

Investigation of electrocatalysts for energy conversion using high throughput experimentation techniques

Dissertation

Zur Erlangung des akademischen Grades eines
Doktors der Naturwissenschaften
(Dr. rer. nat.)

vorgelegt von

Simon Schumacher

geboren am 16.04.1994 in Wuppertal

Universität Duisburg-Essen
Fakultät für Chemie

Juli 2024

Diese Arbeit wurde im Rahmen des DFG-Projekts „***Exploring high-entropy alloys for the hydrogen evolution reaction in alkaline electrocatalysis: from compositional screening to strain effects***” -AN 1570/2-1 an der Fakultät für Chemie der Universität Duisburg-Essen in der Arbeitsgruppe von **Prof. Dr.-Ing. Corina Andronescu** angefertigt.

Tag der Abgabe der Dissertation: 12.07.2024

Prüfungskommission

Vorsitzender: Prof. Dr. Mathias Ropohl, Universität Duisburg-Essen

Gutachterin: Prof. Dr. Corina Andronescu, Universität Duisburg-Essen

Gutachterin: Prof. Dr. Marika Schleberger, Universität Duisburg-Essen

DuEPublico

Duisburg-Essen Publications online

UNIVERSITÄT
DUISBURG
ESSEN

Offen im Denken

ub | universitäts
bibliothek

Diese Dissertation wird via DuEPublico, dem Dokumenten- und Publikationsserver der Universität Duisburg-Essen, zur Verfügung gestellt und liegt auch als Print-Version vor.

DOI: 10.17185/duepublico/82791

URN: urn:nbn:de:hbz:465-20250108-072104-1

Alle Rechte vorbehalten.

Zusammenfassung

Das Streben nach nachhaltigen und umweltfreundlichen Energiequellen hat das Interesse an der Nutzung von Wasserstoff als möglicher Energiespeicher und -träger verstärkt. Diese Dissertation untersucht verschiedene Elektrokatalysatoren für die Wasserstoffproduktion und Energieumwandlungsprozesse, mit dem Fokus auf die Identifizierung effizienter Materialien, die nicht auf teure und seltene Edelmetalle angewiesen sind.

Hoch-Entropie Legierungen (HEAs) und Dünnschichtmaterialien haben vielversprechende Eigenschaften bei der Katalyse kritischer elektrochemischer Reaktionen wie der Wasserstoffentwicklungsreaktion und der Sauerstoffreduktionsreaktion gezeigt. Diese Forschung untersucht das katalytische Potential verschiedener HEA-Zusammensetzungen, einschließlich neuer Kombinationen wie (TiNi)-Cu-Hf-Pd-Zr und zuvor untersuchter Zusammensetzungen wie $\text{Co}_{35}\text{Cr}_{15}\text{Fe}_{20}\text{Mo}_{10}\text{Ni}_{20}$. Hochdurchsatz-Experimentiertechniken wurden eingesetzt, um die Leistung dieser Materialien schnell zu sichten und zu bewerten, was die Identifizierung vielversprechender Katalysatoren erleichtert.

Der Einsatz einer Rastertropfenzelle ergab neuartige HEA-Materialsysteme mit signifikanten katalytischen Aktivitäten. Beispielsweise wurde festgestellt, dass überraschende Kombinationen von Elementen, die zuvor als nicht aktiv in der Katalyse galten, wie Ti, Hf und Zr, einen erheblichen Einfluss auf das katalytische Verhalten haben. Zusätzlich identifizierte das Hochdurchsatz-Screening von über 1000 verschiedenen HEA-Zusammensetzungen innerhalb des CoCrFeMoNi-Raums spezifische Zusammensetzungen mit verbesserter katalytischer Aktivität für die Wasserstoffbildung.

Darüber hinaus wurde die katalytische Aktivität von Dünnschicht-Molybdändisulfid (MoS_2) mittels elektrochemischer Rasterzellmikroskopie untersucht. Diese Technik ermöglichte eine detaillierte räumliche Kartierung der katalytischen Aktivität, wodurch signifikante Leistungsvariationen von MoS_2 sichtbar wurden. Diese Variationen wurden auf Polymerrückstände oder Grenzschicht Phänomene zurückgeführt, die während des Transferprozesses entstanden, und lieferten wertvolle Einblicke in das Verhalten des Materials.

Unabhängig davon wurde der Einfluss von mechanischer Spannung auf Platin (Pt)-Filme untersucht. Die Integration von sogenannten Stress-Chips in den Versuchsaufbau der elektrochemischen Rasterzellmikroskopie ermöglichte die Untersuchung von Pt-Dünnschichten unter angelegter mechanischer Spannung. Diese Dissertation unterstreicht die Bedeutung von Hochdurchsatz-Methoden bei der schnellen Identifizierung und Optimierung von Elektrokatalysatoren. Die umfangreichen Datensätze, die durch diese Methoden generiert wurden, bieten eine wertvolle Ressource für zukünftige Anwendungen des maschinellen Lernens, die darauf abzielen, neue Katalysatorzusammensetzungen vorherzusagen und zu entdecken.

Abstract

The pursuit of sustainable and environmentally friendly energy sources has heightened interest in using hydrogen as a potential energy storage and carrier. This thesis investigates various electrocatalysts for hydrogen production and energy conversion processes, focusing on identifying efficient materials that do not rely on expensive and rare precious metals.

High entropy alloys (HEAs) and thin-film materials have shown promising properties in catalyzing critical electrochemical reactions such as the hydrogen evolution reaction and oxygen reduction reaction. This research explores the catalytic activity of various HEA compositions, including new combinations such as (TiNi)-Cu-Hf-Pd-Zr and previously studied compositions like Co₃₅Cr₁₅Fe₂₀Mo₁₀Ni₂₀. High-throughput experimental techniques were employed to rapidly screen and evaluate the performance of these materials, facilitating the identification of promising catalysts.

The use of a scanning droplet cell revealed novel HEA material systems with significant catalytic activity. For instance, surprising combinations of elements previously considered non-active in catalysis, such as Ti, Hf, and Zr, were found to have a substantial influence on catalytic behavior. Additionally, high-throughput screening of over 1000 different HEA compositions within the CoCrFeMoNi space identified specific compositions with enhanced catalytic activity for the hydrogen evolution reaction.

Furthermore, the catalytic activity of thin-film molybdenum disulfide (MoS₂) was examined using scanning electrochemical cell microscopy (SECCM). This technique allowed for detailed spatial mapping of catalytic activity, revealing significant variations in the performance of MoS₂. These variations were attributed to polymer residues or interfacial phenomena formed during the transfer process, providing valuable insights into the material's behavior.

Separately, the influence of mechanical stress on platinum (Pt) films was investigated. The integration of stress chips into the SECCM setup enabled the study of Pt thin films under applied mechanical stress.

This dissertation underscores the importance of high-throughput methodologies in the rapid identification and optimization of electrocatalysts. The extensive datasets generated through these methods provide a valuable resource for future machine learning applications aimed at predicting and discovering new catalyst compositions.

Eidesstattliche Erklärung

Ich erkläre hiermit, die vorliegende Dissertation mit dem Titel „**Investigation of electrocatalysts for energy conversion using high throughput experimentation techniques**“ selbstständig verfasst und keine anderen als die angegebenen Hilfsmittel und Quellen verwendet zu haben. Wörtliche und inhaltliche Zitate sind stets als solche gekennzeichnet. Bei Kapiteln, die bereits als Zeitschriftenartikel veröffentlicht wurden, sind die Beiträge der Co-Autorinnen und -Autoren zu Beginn verzeichnet.

Ich versichere außerdem, dass ich die vorliegende Dissertation nur in diesem und keinem anderen Promotionsverfahren eingereicht habe und dass diesem Promotionsverfahren keine endgültig gescheiterten Promotionsverfahren vorausgegangen sind.

Duisburg, 12.07.2024

Ort, Datum

Unterschrift

Acknowledgement

This work would not have been possible without the help of many individuals, to whom I extend my heartfelt thanks.

First and foremost, I would like to extend my gratitude to my advisor, Prof. Dr. Corina Andronescu, for giving me the opportunity to pursue my PhD in her research group, and for her unwavering support and guidance. During this time, I have gained invaluable experiences, not only in the scientific field but also in other areas of life, which will benefit me greatly in various situations.

I am also deeply thankful to Prof. Dr. Wolfgang Schuhmann, who welcomed me as a guest in his research group during the early years of my PhD and provided me with immense support. His vast and extensive experience in Analytical Chemistry and scientific research has been a tremendous learning source for me.

I would also like to extend my thanks to Prof. Dr. Marika Schleberger, with whom I completed my Master-Thesis in 2018. This pivotal experience led me to the field of electrocatalysis, which remains central to my professional career. Since then, our paths have never fully parted, and we have continued to collaborate successfully throughout my PhD.

Next, I would like to thank my companion from the very beginning, Michael Braun. We embarked on our PhD journey together and, despite working on very different topics, we have always supported each other, both within and beyond our scientific endeavors.

For their help and collaboration on scientific projects, I would like to thank several members of Ruhr University Bochum, who have become friends beyond our shared work. In particular, I am grateful to my SECCM colleagues Dr. Swapnil Varhade, Dr. Emmanuel Batsa Tetteh, and Dr. Tsvetan Tarnev, as well as Dr. Olga Krysiak and Sabrina Baha, with whom I had the privilege of delving deeply into the world of High Entropy Alloys.

My later PhD period, which I had the pleasure of spending in Duisburg, was made much more enjoyable and easier thanks to my esteemed office partners, Dr. Vimanshu Chanda and Dr. André Olean Oliveira. You have become true friends for life.

I would also like to thank the Andronescu group in Duisburg, who made me feel a sense of belonging even during my stay in Bochum. Foremost among them are Dr.

Ignacio Molto, Faria Huq, Bhawana Kumari, Raíssa Machado, Bright Jaato, Dr. Alejandro Perez-Mendoza, Lithin Banatheth, and Vaibhav Kumbhar.

During my time at RUB and DuE, I had the opportunity to meet and work with many diverse individuals, receiving their help and offering mine in return. I would especially like to thank Adarsh Koul, Dr. Joao Junqueira, Dr. Patrick Wilde, Dr. Tobias Löffler, and Dr. Lukas Madauss.

Letzte Worte möchte ich auf Deutsch an meine Familie, insbesondere meine Eltern und Brüder richten. Seit ich denken kann habt Ihr mich immer unterstützt und gefördert. Ohne Euch wäre ich nicht, wo ich heute bin.

Zwar zum Schluss, aber am aller wichtigsten, möchte ich meiner Frau Sabine danken. Du hast mich in den letzten Jahren immer unterstützt und mir Rückhalt in allen Situationen gegeben. Deine liebevolle Art baut mich auf und deine pragmatische Sicht auf Probleme, die dadurch keine Probleme mehr sind, gibt mir immer Kraft und Motivation weiterzumachen. Jetzt haben wir unseren Sohn Jakob, der unser Leben noch ein kleines bisschen schöner (und lebhafter) macht und dafür bin ich ganz besonders dankbar. Ich freue mich schon auf die nächsten Jahre mit Euch! Ich liebe Euch!

Table of content

Zusammenfassung.....	I
Abstract	III
Eidesstattliche Erklärung.....	IV
Acknowledgement.....	V
1. Introduction.....	1
2. Fundamentals and State of the art	3
2.1 Electrochemical energy conversion	3
2.1.1 Hydrogen evolution reaction as part of Water splitting	3
2.1.2 Oxygen reduction reaction.....	7
2.2 Electrode materials for electrochemical energy conversion.....	10
2.2.1 High entropy Alloys	10
2.2.2 2D-Materials.....	13
2.2.3 Strain engineering for optimizing catalytic activity.....	17
2.3 High throughput techniques as method for analysis of electrocatalysts.....	20
2.3.1 Voltammetric analysis methods.....	20
2.3.2 Scanning droplet cell	25
2.3.3 Scanning electrochemical cell microscopy.....	28
3. Motivation and aim of the work	34
4. Results and discussion.....	36
4.1 High entropy alloy compositions spreads on material libraries.....	36
4.1.1 (TiNi)-Cu-Hf-Pd-Zr	36
4.1.2 Co-Cr-Fe-Mo-Ni	45
4.2 SECCM investigations on thin-film molybdenum disulfide	53
4.2.1 Initial setup measurements.....	53
4.2.2 Noise reduction	57
4.2.3 Revealing the heterogeneity of large-area MoS ₂ layers in the electrocatalytic hydrogen evolution reaction	59
4.3 Design, Construction and Evaluation of SECCM configuration for strain induced optimization of the electrocatalytic activity for HER	68
4.3.1 Idea of the project.....	68
4.3.2 Design and construction of the stress chip holder.....	69
4.3.3 Integration of Gas-/Ar-chamber.....	72
4.3.4 Bending the cantilever on the stress chip	78
4.3.5 Bending the cantilever on the stress chip and measuring with SECCM.....	79

4.3.6	Problem analysis of the SECCM experiments on the stress chip samples	91
5.	Conclusion and outlook	93
6.	Experimental procedures	95
6.1	Materials/Tools Used	95
6.1.1	List of chemicals	95
6.1.2	List of materials	95
6.1.3	List of devices	96
6.1.4	List of software	96
6.2	Sample and probe fabrication and preparation.....	96
6.2.1	Sputtering process.....	96
6.2.2	CVD process.....	97
6.2.3	Transfer of MoS ₂	98
6.3	Sample and probe characterization	100
6.3.1	Scanning electron microscopy.....	100
6.3.2	Preparation of Ag/AgCl QRCE.....	100
6.3.3	Preparation of SECCM probes (capillaries).....	100
6.3.4	Filling of the capillaries.....	101
6.3.5	Checking the OCP of the QRCE	101
6.4	SDC experiments	102
6.4.1	SDC experiments on (TiNi) -Cu-Hf-Pd-Zr	102
6.4.2	SDC experiments on Co-Cr-Fe-Mo-Ni.....	102
6.5	SECCM experiments	103
6.5.1	Initial SECCM setup.....	103
6.5.2	SECCM setup optimization	104
6.5.3	SECCM experiments on MoS ₂	104
6.5.4	SECCM experiments on stress chips.....	105
7.	List of contributions.....	106
7.1	First author publications	106
7.2	Co-author publications.....	106
8.	References.....	108

1. Introduction

The goal of making water an inexhaustible energy source and achieving independence from fossil fuels like coal or oil is widely shared among environmentally conscious people. This objective aims to mitigate or delay climate change from excessive CO₂ emissions.¹⁻³ The effectiveness of hydrogen production and its utilization in energy conversion systems plays a crucial role in the advancement of the hydrogen economy. Currently, the widespread methods employed for commercial hydrogen production, such as catalytic steam reforming, partial oxidation, and coal gasification, contribute substantially to global CO₂ emissions. While there is potential for purely thermal processes utilizing nuclear or solar heat concentration to generate hydrogen, these methods are still in the early stages of development.^{4,5}

Researchers are actively working on the efficient recovery, storage, and conversion of hydrogen, which is considered a clean energy source when used in conjunction with oxygen in fuel cells. A significant challenge in this field is the reduction of reliance on expensive and scarce precious metals, such as platinum, for catalytic purposes in electrochemical hydrogen generation and conversion.^{6,7} Consequently, numerous research groups worldwide are investigating cost-effective and resource-efficient materials that have the potential to serve as catalysts in fuel cells or electrolyzers.⁸⁻¹⁰

To expedite the discovery and development of new materials essential for the successful establishment of a sustainable hydrogen economy, it is necessary to embrace disruptive concepts. These innovative approaches can revolutionize the traditional processes and methodologies, leading to accelerated advancements in material research.¹¹⁻¹⁵

High-throughput experimental methodologies are invaluable for expediting the synthesis and testing of materials to achieve optimized performance. These methods facilitate the rapid generation of high-quality experimental data, making them essential for identifying well-suited catalyst materials used in energy conversion processes. Effective catalyst characterization is crucial in the development of catalytic materials as it aids in identifying active catalytic phases or centers and provides insights into reaction mechanisms.¹⁶⁻¹⁸

The research presented in this thesis focuses on the investigation of electrocatalysts using high throughput techniques. Specifically, material libraries containing a range of high entropy alloy compositions are screened using a scanning droplet cell to evaluate their performance in the hydrogen evolution reaction (HER) and the oxygen reduction reaction (ORR). Additionally, the scanning electrochemical cell microscopy (SECCM) technique is employed to study the catalytic HER activity of thin film molybdenum disulfide, synthesized through a chemical vapor deposition (CVD) process and transferred onto a conductive substrate. Furthermore, the SECCM setup is used to investigate sputtered platinum (Pt) thin films on stress chips, enabling the application of external stress on the catalyst layer during electrochemical measurements.

Scientific findings described in this thesis encompasses uncovering new electrocatalysts using screenings, as well as gaining a better understanding of the active areas of molybdenum disulfide using high-throughput measurements. In addition to that, this thesis also focuses on technical improvements which include enhancing the signal-to-noise ratio and implementing stress chip sample systems within the SECCM setup.

2. Fundamentals and State of the art

This chapter provides an overview of the fundamental electrochemical reactions that were investigated in the experimental part of this PhD research, namely the hydrogen evolution reaction (HER) and the oxygen reduction reaction (ORR), which are crucial reactions for energy conversion processes. Additionally, three types of electrode materials that were analyzed are introduced: high entropy alloys, 2D materials with a focus on MoS₂ as an example, and materials optimized for catalytic properties using strain engineering. Furthermore, the role of two high throughput techniques for electrochemical analysis is discussed: the scanning droplet cell (SDC) and the scanning electrochemical cell microscopy (SECCM). The chapter includes descriptions of the advantages and state-of-the-art examples of these techniques, as well as their general principles.

2.1 Electrochemical energy conversion

2.1.1 Hydrogen evolution reaction as part of Water splitting

Water electrolysis involves using an electric current passed through an anode and cathode immersed in an electrolyte to facilitate the separation of hydrogen and oxygen. Although the fundamental principle remains unchanged, various types of electrolysis devices, such as polymer electrolyte membrane (PEM) electrolyzer,¹⁹ alkaline electrolyzer,²⁰ and solid oxide electrolyzer,²¹ can be employed for hydrogen generation. These devices differ primarily in terms of ion transport mechanisms and the specific type of electrolyte used.^{19–21} Figure 1 illustrates the fundamental principle of an electrolysis cell operating under acidic conditions. The fundamental process remains consistent across all water electrolysis technologies: water is supplied to an electrochemical cell where, under the application of a sufficiently high voltage, hydrogen is generated at the negative electrode (cathode) and oxygen is generated at the positive electrode (anode). The charge difference is balanced by movement of ion molecules, in Figure 1 illustrated through movement of H₃O⁺, representing ions in acidic electrolyte.

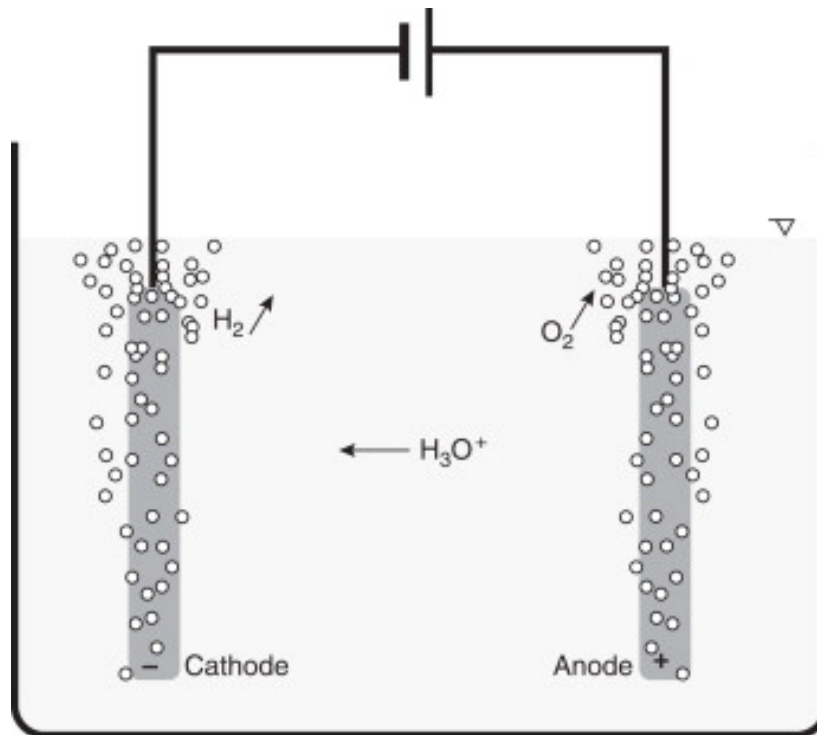


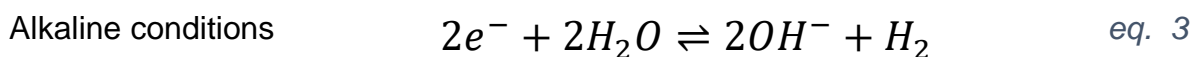
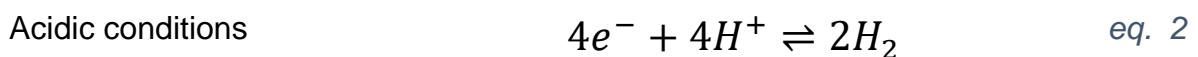
Figure 1: Schematic representation of the general principle of the water splitting reaction in acidic media. Hydrogen molecules are produced at the negatively charged cathode and oxygen molecules at the positively charged anode. Reproduced from ²² with permission from Elsevier.

The following equation is representing the overall reaction happening during the water splitting:

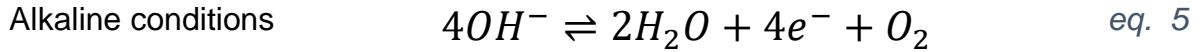
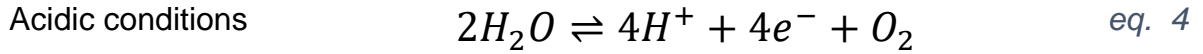


Two water molecules are split to two hydrogen molecules and one oxygen molecule. The overall electrolysis reaction can be divided into two half-cell reactions taking place at the cathode and anode, involving reduction and oxidation processes, respectively. At the cathode, the hydrogen evolution reaction (HER) occurs, resulting in the evolution of hydrogen gas. On the other hand, at the anode, the oxygen evolution reaction (OER) takes place, leading to the evolution of oxygen gas. Water electrolysis can be carried out in both acidic and alkaline media. The following equations describe these reactions.

Cathodic reaction (HER):



Anodic reaction (OER):



The OER is a complex process that involves the transfer of four electrons and four protons, called proton-coupled electron transfer (PCET). It occurs through four distinct electron transfer steps and typically requires higher overpotentials compared to the HER.^{23,24} Although the OER is a fascinating area of research, it is not the focus of discussion in this particular thesis. Therefore, detailed explanations and analysis of the OER are not provided in this chapter.

The HER is a half-cell reaction that takes place during the electrolysis of water. It entails the transfer of two electrons. In alkaline conditions, the reaction commences with the dissociation of water, followed by the adsorption of hydrogen and the transfer of one electron at a suitable surface site. Also known as Volmer step. In acidic environments, the Volmer step involves the direct adsorption and reduction of a proton from the electrolyte without prior water dissociation. The subsequent stage involves the generation and release of H₂, which can be achieved either through the combination of the adsorbed hydrogen atom with another proton from the solution, occurring together with the transfer of one electron (Heyrovski step in alkaline conditions), or by the combination of two adsorbed hydrogen atoms (Tafel step in acidic conditions).²⁵⁻²⁷

To initiate this process, a specific quantity of electric energy is required. This can be determined by formulating the redox potentials associated with each individual reaction. The difference between these two potentials establishes the reversible voltage of the overall reaction, denoted as $E_{H_2O}^0$, which is 1.229 V²⁵ and remains unaffected by the solution's pH value. These calculations pertain to electrolysis conducted at a temperature of 25 °C. To carry out isothermal electrolysis, the thermal energy of 48.652 kJ mol⁻¹ must be overcome by applying a higher voltage, resulting in a voltage of $E_{H_2O}^{0,en} = 1.481$ V²⁵ for isothermal water electrolysis. Since water electrolysis is often conducted at elevated temperatures, it is necessary to account for temperature-dependent thermal energy, which accounts for the heating and evaporation of water. Additionally, during operation, the anodic and cathodic overpotentials η_a and η_c , as well as the ohmic drop iR , are included in the

thermoneutral electrolysis voltage $E_{H_2O}^{0,in}$.²⁵ The ohmic drop iR signifies the voltage decline caused by the ohmic resistance of the electrolyte, while the anodic and cathodic overpotentials η_a and η_c arise from changes in reactant concentration during the electrochemical reaction.²⁸ Consequently, the required operational voltage can be calculated using following equation.²⁵

$$E = E_{H_2O}^{0,in} + \eta_a + \eta_c + iR \quad \text{eq. 6}$$

To ensure energy-efficient operation of the process, it is desirable to minimize the Ohmic drop and overpotentials. This can be achieved by utilizing electrode materials with high activity, characterized by a higher exchange current density or a larger electrode surface area.²⁵ Platinum (Pt) serves as an excellent example of a highly active electrode material. Additionally, electrode coatings with catalysts can be employed to enhance the activity or effective surface area of the electrodes.

In the presence of a catalyst, the HER typically follows two reaction mechanisms, including the before described reaction steps and depicted in Figure 2 for Pt as model catalyst. These mechanisms exhibit varying dominance depending on the catalyst. The first mechanism is the Volmer-Heyrovsky mechanism (Figure 2b), where a hydrogen cation initially adsorbs onto the catalyst surface, followed by another hydrogen cation reacting with the adsorbed ion to form H_2 , which subsequently desorbs from the surface. The second mechanism is the Volmer-Tafel mechanism (Figure 2a), where two hydrogen cations adsorb on the surface in the first step, and then these adsorbed ions react with each other to produce H_2 , which desorbs from the surface.²⁹ In the case of Pt, the Volmer-Tafel mechanism dominates during the HER process due to the high coverage of H^+ ,^{30,31} which serves as the rate-limiting step for catalysis.

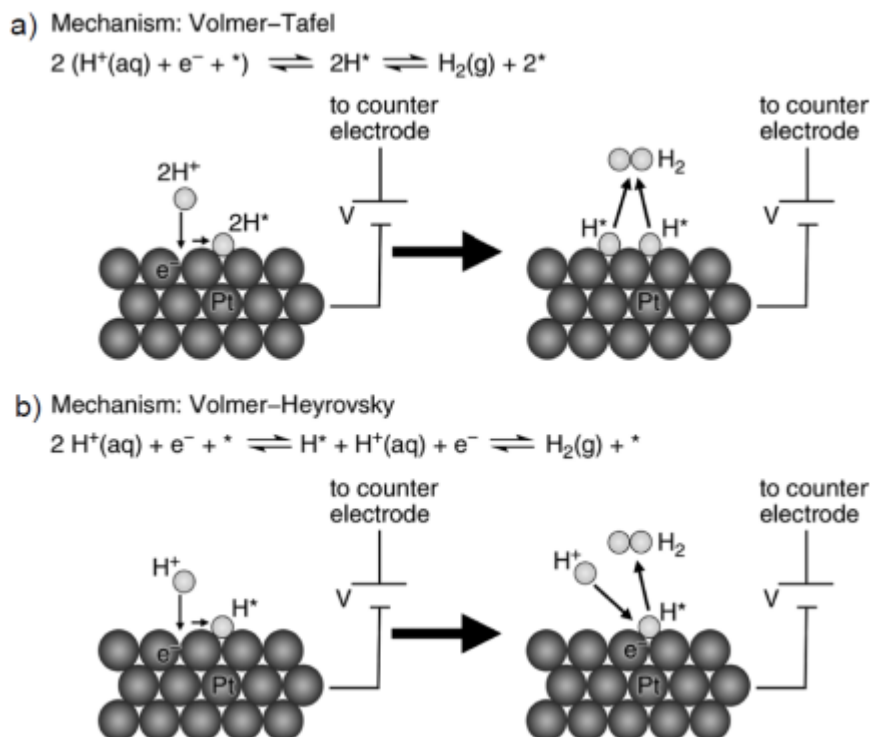


Figure 2: Two mechanisms proposed for the hydrogen evolution reaction (HER) on platinum surfaces: the Volmer-Tafel mechanism (a) and the Volmer-Heyrovsky mechanism (b). In these mechanisms, the asterisk (*) represents an unoccupied active site, while H^* denotes a hydrogen atom bound to the active site. (Adapted with permission from²⁹. Copyright 2012 American Chemical Society)

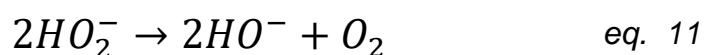
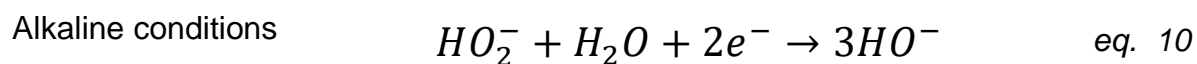
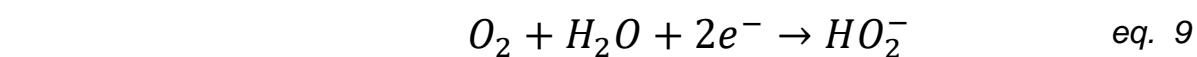
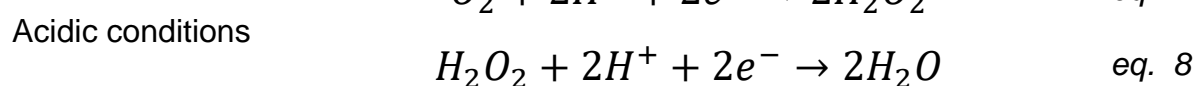
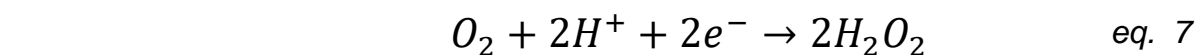
2.1.2 Oxygen reduction reaction

Proton exchange membrane fuel cells (PEMFCs) and rechargeable metal-air batteries (MABs) represent advanced energy devices with the potential for clean power generation.^{32,33} In the discharge process of PEMFCs or MABs, the cathode facilitates the oxygen reduction reaction (ORR), where O_2 molecules undergo reduction through proton-coupled electron transfer. However, the electrochemical dissociation of the O_2 bond, which possesses a remarkably high bond energy of 498 kJmol^{-1} ,³⁴ presents a significant challenge. To overcome this obstacle, the assistance of electrocatalysts becomes crucial, as they enable the activation and cleavage of the O_2 bond, thereby lowering the energy barrier. In the cathode of PEMFCs, the ORR occurs at a significantly slower rate compared to the hydrogen oxidation at the anode in aqueous solutions. This substantial difference in kinetics is attributed to the complex nature of adsorption/desorption processes and reaction pathways, involving various O-containing intermediates.³⁵

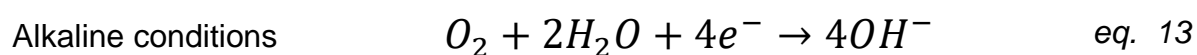
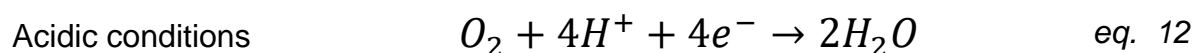
The ORR can proceed through two distinct pathways. The first pathway, commonly known as partial reduction, involves a two-electron process leading to the formation of adsorbed hydrogen peroxide (H_2O_2). In contrast, the second pathway, referred to as

full reduction, follows a more efficient four-electron process that does not involve the generation of H_2O_2 .^{36–38} Given the enhanced efficiency of full reduction and the relatively high reactivity of hydrogen peroxide compared to water, catalysts that favor the full reduction pathway are sought after for ORR applications.³⁹ In the following the reaction steps for both pathways are illustrated.⁴⁰

Two-electron pathway (partial reduction):



Four-electron pathway (full reduction):



In the industrial context, commercially available electrocatalysts utilized for the ORR in PEMFCs primarily consist of precious Pt-based nanomaterials, which contribute to a significant portion of the overall cost of PEMFCs.^{41,42} However, these Pt-based electrocatalysts face several challenges such as high cost due to limited availability, susceptibility to fuel crossover, and poor stability. Consequently, these limitations severely restrict their widespread application in PEMFCs or MABs. Therefore, it is imperative to prioritize the development of cost-effective, highly active, and stable electrocatalysts for the ORR as alternatives to Pt-based electrodes, facilitating the large-scale implementation of PEMFCs or MABs.⁴³

One approach of decreasing the number of noble metals in the catalyst is the alloying of noble metals like Pt with first-row, late transition metals like Fe, Co, Ni, Cu, etc. This approach has been shown to engender enhanced electrochemical performance relative to pure Pt.^{44,45} The improved performance is mainly attributed to changes in

the electronic structure of Pt atoms induced by the presence of foreign metal atoms. These modifications optimize the adsorption strength between Pt and reaction intermediates (OH, OOH) during the ORR.⁴⁶⁻⁴⁸ Such alloying strategies hold promise for developing cost-efficient and highly active ORR electrocatalysts that can serve as substitutes for Pt-based electrodes in large-scale applications of PEMFCs or MABs. Similar approaches for a design and optimization of catalyst materials are made using so called high entropy alloys, which is the topic of the next chapter.

2.2 Electrode materials for electrochemical energy conversion

2.2.1 High entropy Alloys

Polyelemental alloys, such as compositionally complex solid solutions (CCSS) or high entropy alloys (HEAs), have been extensively studied in electrocatalysis due to their superior activity compared to traditional electrocatalysts.^{49–52} CCSS consist of five or more elements, typically in the range of 5–35 at.%, and are stabilized by a high mixing entropy, resulting in a single phase structure.⁵³ The surface composition of CCSS offers multiple atomic arrangements with different binding energies, leading to a higher density of optimal or near-optimal binding energies for specific reactions after suitable structure optimization.⁵⁴ In recent years, a wide range of CCSS systems with diverse combinations of elements have been investigated for various electrochemical reactions, including the HER,^{55–61} ORR,^{62–64} OER,^{65–70} carbon monoxide reduction,^{63,71} methanol oxidation,^{63,72} and ammonia synthesis and decomposition.^{49,73}

Löffler et al.⁶⁴ demonstrated that certain compositions in the Co-Cr-Fe-Mn-Ni system exhibit higher activity for the ORR compared to Pt, whereas this was not observed for quaternary, ternary, or binary combinations of the same elements. Zhang et al.⁵⁵ also reported that arc-melted Co₃₅Cr₁₅Fe₂₀Mo₁₀Ni₂₀ shows comparable electrocatalytic activity for the HER to Pt in alkaline electrolytes.

In addition, it has been reported that HEA compositions containing noble metals can effectively reduce the total utilized amount of noble metals while boosting catalytic activity compared to using noble metals alone.⁷⁴ Glasscott et al. demonstrated a method to synthesize CoFeLaNiPt using a nanodroplet technique, which resulted in a catalyst surpassing the activity of Pt alone, considered as the benchmark catalyst, for the HER.⁷⁴ Following a similar approach, Li et al. explored Pt-based HEAs with various element combinations and discovered that the Al-Cu-Ni-Pt-Mn composition exhibited significantly improved activity for the ORR compared to pure Pt, thereby reducing the reliance on Pt content in the catalyst.⁷⁵

The broad range of applications for catalytic processes highlights the significant potential of utilizing HEAs as catalysts. Brian Cantor, a pioneer in HEA and complex solid solution research, explains that the unique feature of compositionally CCSS is their synergetic effect, which arises from the collective behavior of the highly entropic system. This effect goes beyond a simple combination of the individual properties of

the elements involved.⁷⁶ In addition to the unique features of specific active sites that are synergistically optimized by the combination of four other elements, another advantage of HEAs lies in the presence of neighboring active sites with distinct properties. This arrangement enables follow-up reactions of primary reaction products to take place, utilizing closely localized active sites that possess ideal properties for both reactions. This characteristic is particularly valuable in catalytic reactions where products are formed through multistep or cascade reactions.¹¹ Figure 3 illustrates three different possibilities of a model multistep reaction involving two reductions using two different active sites.

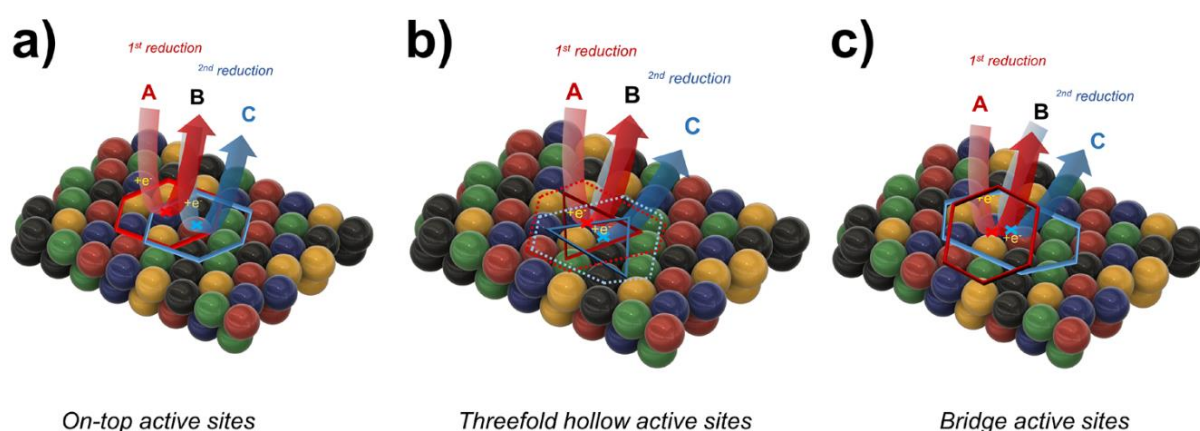


Figure 3: Illustration of a cascade reaction at the surface of a CSS catalyst involving two consecutive reduction reactions with single coordinating intermediates. The active sites of the catalyst have different properties and are represented as atoms (a), three-fold coordinated adsorption (b), and bridge coordinated adsorption (c). The cascade reaction occurs at directly neighboring active sites, facilitating efficient conversion of reactants into products. Adapted with permission¹¹. Copyright 2019 American Chemical Society

While these aforementioned findings highlight the potential of CCSS as electrocatalysts, the exploration of CCSS materials is still limited, considering the vast materials space available. For instance, in the quinary Co-Cr-Fe-Mo-Ni system alone, there are over 4.5 million theoretically possible compositions, with each element varied in 1 at. % increments. Moreover, post-treatments, such as exposing alloys to elevated temperatures, further expand the potential for synthesizing new materials.⁷⁷

In recent investigations, a combination of simulation, machine learning, data-guided combinatorial synthesis, and high-throughput characterization has been employed to identify a CCSS catalyst with outstanding activity. This process, known as the iterative materials discovery loop, entails assessing computational predictions through experimental validation. These studies have unveiled that simplistic descriptors are inadequate for predicting the activity of electrocatalysts on CCSS surfaces. Thus,

substantial advancements in computational methodologies specific to CCSS are necessary to overcome this challenge.¹²

Efficient research methods are needed to explore this vast space and discover novel catalysts. Combinatorial synthesis of thin-film materials libraries (MLs) has emerged as a promising approach for accelerated material discovery. MLs cover a wide composition range with defined composition gradients, facilitating high-throughput characterization methods.^{78,79} Co-sputtering confers the advantage of achieving atomic-level mixing during deposition, facilitating the simultaneous synthesis of high-purity thin films in a singular process. In a single experimental run, continuous composition spreads can be generated, encompassing all possible combinations within ternary systems.⁸⁰

However, as the number of elements increases to quaternary and higher systems, the coverage of compositions within a single ML is considerably reduced. Combinatorial co-deposition of four or more elements results in varied composition gradients contingent upon the relative arrangement of deposition sources. Recently, a strategy was reported that effectively broadens the coverage of quinary systems by sequentially fabricating MLs with permuted arrangements of individual deposition sources.⁷⁷ Nevertheless, achieving comprehensive coverage of the entire composition space in multinary systems necessitates a substantial experimental undertaking, making it currently unfeasible to encompass the entire space. Considering the substantial experimental effort required to encompass significant portions of multinary composition spaces and the vast number of potential material systems, it becomes evident that a disruptive approach to materials discovery and screening is indispensable.^{12,77}

2.2.2 2D-Materials

Since 2004, extensive research has been conducted on the class of two-dimensional (2D) materials, which have garnered increasing attention due to their remarkably thin nature and outstanding mechanical,⁸¹ electrical,⁸² and optical⁸³ properties. Among these materials, graphene, an atomically thin layer of carbon, has emerged as the most well-known representative. Although theoretical investigations of 2D graphite have been ongoing for many years, it was primarily regarded as an academic material.⁸⁴ Landau and Peierls' theoretical work questioned the thermodynamic stability of 2D materials, stating that thermal fluctuations could lead to atomic distortions on the scale of interatomic distances.^{85,86} This perspective was further supported by subsequent research conducted by Mermin and Wagner.⁸⁷

Experimental data at the time reinforced these theoretical notions, as a considerable decrease in the melting temperature with diminishing layer thickness was repeatedly observed. This phenomenon facilitated the formation of material islands and suggested that pure 2D materials lacked thermodynamic stability. However, the discovery of graphene in 2004⁸⁸ and subsequent findings on other 2D materials⁸⁹ effectively refuted these prevailing views. The existence of 2D materials can be rationalized by their confinement in a metastable state, maintained by robust interatomic covalent bonds that resist thermal fluctuations and the formation of defects.^{85,87} Another perspective, put forth by Meyer et al., indicates that while graphene exhibits microscopically flat crystalline regions, its macroscopic surface appears undulated, thereby challenging its purely 2D character.⁹⁰ According to this viewpoint, the gain in elastic energy, accompanied by the suppression of thermal vibrations, reduces the overall free energy, enabling graphene to achieve thermodynamic stability.⁹¹

In addition to graphene, the group of two-dimensional transition metal dichalcogenides (2D TMDCs) has garnered significant interest, with MoS₂ being the most renowned member of this family. Molybdenum disulfide (MoS₂), a transition metal dichalcogenide, exhibits a layered crystal structure in which molybdenum atoms are covalently bonded to a plane of sulfur atoms. This arrangement gives rise to a monolayer consisting of three atomic layers, as illustrated in Figure 4.⁹² Each individual monolayer has an approximate thickness of 0.6-0.7 nm.⁹²

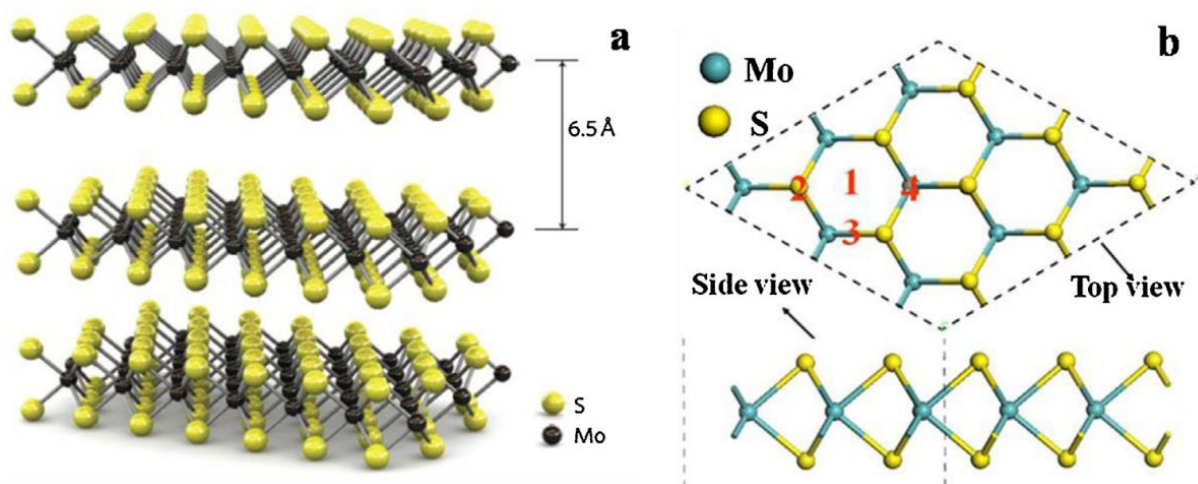


Figure 4 Structure of 2H-MoS₂ layers. Adapted from ⁹²with permission from Elsevier.

In crystalline MoS₂, two distinct crystal structure symmetries are observed. In the monolayer form, there are two types: 2H-MoS₂, which exhibits trigonal prismatic symmetry and displays semiconducting properties, and 1T-MoS₂, which possesses octahedral crystal symmetry and exhibits metallic properties.⁹³ Similar to graphite, bulk MoS₂ is utilized as a solid lubricant in vacuum systems due to its weak van der Waals bonds between the layers, high melting temperature, and low reactivity.⁹⁴ Moreover, MoS₂ is a semiconductor with an indirect band gap of 1.29 eV in its bulk form. Interestingly, this value undergoes a change as the number of layers decreases, resulting in a direct band gap of 1.9 eV in single-layer MoS₂.⁸³ These semiconducting properties make MoS₂ suitable for various applications, such as (opto-)electronics.^{95,96} Additionally, the layer thickness of MoS₂ can be determined by analyzing the frequencies of inelastically scattered photons in Raman spectroscopy.⁹⁷ Furthermore, MoS₂ serves as a catalyst for the hydrogen evolution reaction, which is discussed in more detail in the following.

2.2.2.1 MoS₂ as catalyst for HER

As previously mentioned, MoS₂ has gained significant interest in recent years due to its favorable catalytic properties for the hydrogen evolution reaction (HER). Efficient HER catalysis relies on a catalyst's ability to bind atomic hydrogen with a binding energy close to zero, similar to platinum (Pt). In the case of MoS₂ nanoparticles, the moderate overpotential ranges between 0.1 V and 0.2 V.⁹⁸ A study conducted by Jaramillo et al. in 2007 revealed that the catalytically active sites on MoS₂ are primarily located at the material's edges.⁹⁹

Furthermore, when comparing the current density with the edge length of MoS₂, it was observed that there is a better correlation with a linear increase, rather than the surface coverage of MoS₂.⁹⁹ This suggests that the activity is more directly influenced by the presence of edges rather than the overall surface area. In a separate study conducted by Yu et al. in 2014, the influence of the number of layers of MoS₂ on catalytic activity was investigated. It was discovered that the catalytic activity for the HER on MoS₂ catalysts decreases by a factor of approximately 4.47 for each additional layer of MoS₂.¹⁰⁰ These findings suggest that a MoS₂ catalyst with a higher number of edges and fewer layers can achieve better activity. For MoS₂ catalysts in HER, it is believed that the rate-limiting step is the reaction of the Volmer-Heyrovsky mechanism, primarily due to the relatively low coverage of H⁺ on the catalyst surface.³⁰ Additionally, as mentioned earlier, thin materials such as two-dimensional MoS₂ are advantageous for HER due to their strong electrical connection to the substrate material.

Previous studies have often attributed the catalytic activity for the HER in thin layered MoS₂ solely to the edge plane, considering the basal plane as inert.¹⁰¹ However, recent high-resolution electrochemical imaging studies have challenged this notion. These studies have shown that while the edge plane exhibits high activity for HER, directly observed at step edge features in few- to multi-layer MoS₂, the basal plane also exhibits significant catalytic activity. Takahashi et al.¹⁰² conducted high-resolution scans on MoS₂ flakes covering few micrometer sized areas that were transferred onto highly oriented pyrolytic graphite (HOPG) after synthesis using chemical vapor deposition (CVD). Figure 5 a) and b) illustrate maps of the currents and overpotentials for the HER respectively. The results demonstrate that the basal plane of MoS₂ contributes significantly to the overall activity, despite having lower activity compared to the edge plane. Figure 5 c) and d) depict the different activity regions observed within the scan and provide exemplary LSV experiments, respectively. Furthermore, it has been discovered that the activity of the BP can vary between different surfaces or crystals. However, it consistently demonstrates relatively lower activity compared to the edge plane, with an exchange current density (j_0) of approximately 10^{-4} Acm⁻² for edge plane.^{102,103} The exchange current density (j_0) for the BP is approximately $3 \cdot 10^{-6}$ Acm⁻², which is comparable to polycrystalline Au or Ni.¹⁰⁴

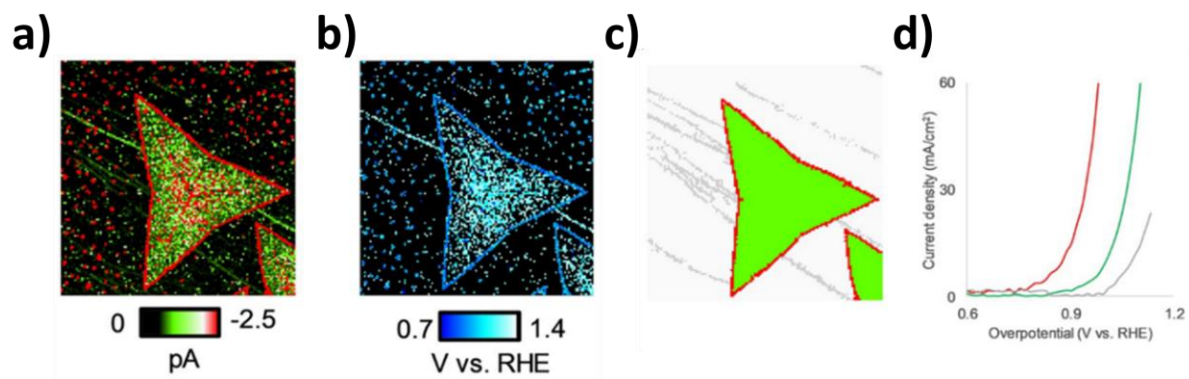


Figure 5 SECCM scan of MoS₂ flake a) current response, b) overpotential, c) 3 color mapping, d) exemplary LSVs. Adapted from ¹⁰²with permission of Wiley.

2.2.3 Strain engineering for optimizing catalytic activity

The inherent effectiveness of each catalytic site essentially adheres to the Sabatier principle, which is closely associated with the electrocatalyst's capacity to modulate the binding energies with reactants, intermediates, and products. For instance, when the adsorption of hydrogen on the active sites of an electrocatalyst maintains a moderate level of free energy (ΔG_H), the catalyst exhibits the highest level of catalytic activity in facilitating the HER. Conversely, excessively strong or weak ΔG_H on the active sites of an electrocatalyst hindering the HER process. Therefore, achieving the optimal HER performance necessitates finding the appropriate equilibrium in the strength of ΔG_H . This described principle has been supported by numerous studies^{105–109} highlighting the crucial role of ΔG_H in determining catalytic efficiency.

The interaction between electrons of a species and a metal active site during adsorption leads to the formation of new bonding and anti-bonding orbitals.^{110–112} Figure 6 depicts the binding energy relationships for a transition metal, serving as an example. The anti-bonding orbital is energetically close to the Fermi level and is partially occupied.¹¹³ A higher energy anti-bonding orbital compared to the Fermi level indicates that more antibonding orbitals remain unoccupied, resulting in a more stable adsorption of the species. This stability is associated with a higher energy of the d-band center of the metal active site. Hence, the d-band center of a metal site serves as a crucial parameter in determining the adsorption capability of a metal active site.^{114,115}

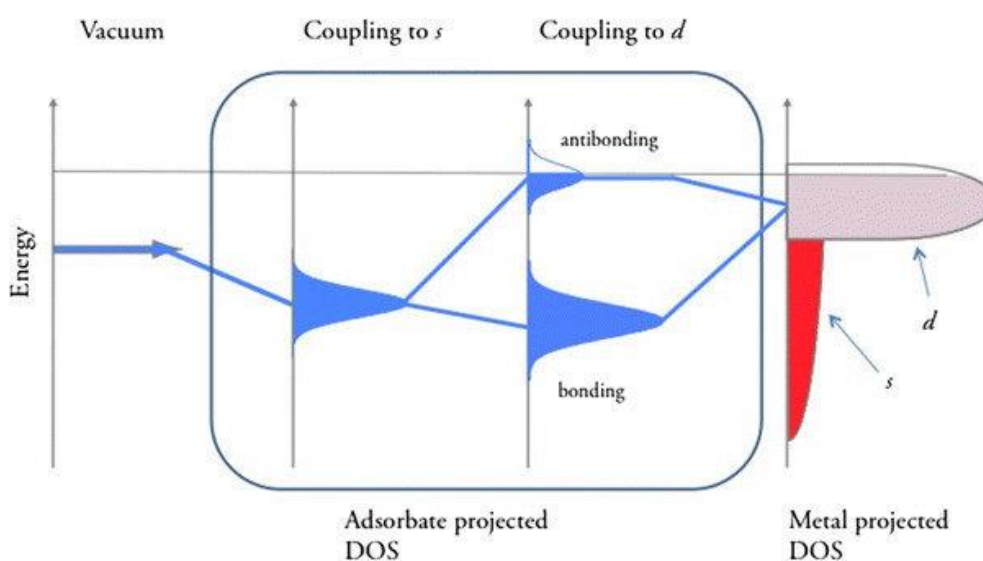


Figure 6: Schematic illustration of the d-band model depicting the interaction between an adsorbate adatom level and the s- and d-states of a transition metal surface. Adapted from ¹¹⁴with permission from Springer Nature

The position of the d-band can be effectively modified by adjusting the lattice strain of the metal crystal, providing a potential path for optimizing catalytic activity.¹¹⁶ Lattice strain refers to the variation in atom-atom distance on the surface or within a local region of a particle, which can deviate from the standard atom-atom distance found in the bulk material. This strain effect can either result in an increased (compressive strain) or decreased (tensile strain) atom-atom distance compared to the bulk material. The intensity of strain depends on the standard atom-atom distance in the lattice of the bulk material, as well as the atom-atom distance on the particle or local area surface. Thus, depending on the element of the atom, it is possible to observe either a compressive or tensile strain effect.¹¹⁷

The catalytic reactivity of a metal surface is influenced by strain, which causes changes in the electronic structure.^{118,119} According to d-band theory,^{110,114,117–119} applying tensile strain to late transition metals results in shifting the d-band center closer to the Fermi level and narrowing the bandwidth. This shift leads to a reduction in electron occupation in the antibonding states of the metal-adsorbate interaction, ultimately leading to stronger adsorbate binding on the metal surface.

Strain alteration is a significant factor in enhancing catalytic activity in various electrochemical reactions. One notable example of strain-induced activity enhancement is the utilization of core-shell structured materials.^{120–122} In a core-shell catalyst, there is a difference in lattice parameters between the metal in the core and the metal in the shell, leading to strain between the two lattice structures. The magnitude of this strain can be adjusted using various methods. By this controlling the strain state is of utmost importance in the design of core-shell catalysts. Specifically, the strain in the shell layer can be regulated by selecting an alloy with a tunable lattice parameter as the core. By carefully choosing the composition of the core material, the lattice mismatch between the core and shell can be adjusted, thereby influencing the strain state in the shell layer.¹¹⁷ Xie et al. employed octahedral structures of PtCo and conducted annealing processes to deposit thin layers of Pt on top of the octahedra. This approach resulted in a significant enhancement of the ORR activity.¹²³ Liu et al. utilized Pd/Pt core-shell materials and employed hydrogen intercalation to induce a change in the lattice spacing of the Pd core, leading to lattice expansion of the Pt shell. This approach effectively promoted the alcohol oxidation reaction (AOR).¹²⁴ He et al. employed a similar approach by utilizing Pd/Pt core-shell structures and phosphorizing

the Pd component. This allowed them to tune the lattice strain, either towards compression or tensile side, by manipulating the lattice tensions, resulting in increased HER activity.¹²⁵

Another approach for altering lattice strain involves changing the atom-atom distance within the support material of a layered structure. This can be achieved by mechanically bending the substrate, resulting in a modification of the strain in the layer deposited on top of the support. Yan et al.¹²⁶ conducted a study where an elastic polymer electrode was coated with various metals (Pt, Cu, and Ni). The electrocatalytic activity for the HER was tested using a three-electrode setup, with the polymer electrode serving as the working electrode. The researchers observed that applying different external strains (compressive and tensile) to the polymer electrode resulted in a change in activity. This change could be explained by the shift in the d-band position and variations in adsorption energies. Deng et al.¹²⁷ employed a similar approach and obtained similar findings with regards to Au and Pt. They utilized a piezo-modulated polymer electrode as the support for the catalyst materials.

2.3 High throughput techniques as method for analysis of electrocatalysts

The comparison between "conventional" and "high throughput" techniques plays a crucial role in this thesis. The conventional techniques, such as RDE and RRDE measurements, are highly reliable and produce qualitatively accurate results with well-defined properties and a high reproducibility rate.¹²⁸ However, when the objective is to screen a large number of catalyst sites or different catalyst compositions, these methods prove to be inefficient and time-consuming. In such cases, high throughput techniques offer an alternative approach that enables a significantly higher number of experiments to be conducted within a reasonable timeframe.¹²⁹ These techniques enhance efficiency and deliver faster results, making them valuable tools for catalyst analysis in high-volume screening scenarios.^{78,130,131}

Voltammetric methods play a vital role in both conventional and high throughput techniques for investigating electron transfer kinetics, transport properties of electrochemical reactions, and characterizing the activity and other properties of electrocatalysts. These methods are essential for describing key features of the high throughput methods employed in this thesis. Specifically, cyclic voltammetry and linear sweep voltammetry will be briefly described in the following.¹³²

2.3.1 Voltammetric analysis methods

The measurement process involves applying a voltage between a working electrode and a reference electrode, which are connected through an aqueous electrolyte. A current is then measured between the working electrode and a counter electrode (in a 3-electrode setup) or a quasi-reference counter electrode (in a 2-electrode setup). By fixing the potential at the reference electrode and varying the potential at the working electrode, different currents corresponding to the working electrode potential can be measured.^{132,133}

Linear sweep voltammetry (LSV) is a technique that involves applying a fixed potential range, similar to potential step measurements. The potential is changed at a specific scan rate, which is determined by the rate at which the potential changes over time. By adjusting the time taken to sweep the potential range, the scan rate is modified. The recorded linear sweep voltammogram exhibits certain characteristics that are influenced by various factors, such as the rate of the electron transfer reaction, chemical reactivity of the electroactive species, and the voltage scan rate.^{132,133}

The voltammogram obtained in linear sweep voltammetry (LSV) is influenced by the scan rate used. While the overall shape of the curve remains the same, the total current increases with higher scan rates. This can be explained by considering the size of the diffusion layer and the time taken to record the scan. The Gouy-Chapman-Stern model¹³⁴ offers an approach to describe the behaviour of ions at the electrode surface. It proposes the presence of a compact layer close to the electrode surface, known as the Stern layer, which contains counter-ions that balance the surface charges on the electrode. Beyond the Stern layer, there is the diffusion layer where counter-ions diffuse due to thermal motion. These layers can be represented by two capacitors in series which is represented in Figure 7. The size of these layers depends on the electrode surface potential and the diffusion processes of ions.^{133–135} When the scan rate is decreased, the linear sweep voltammogram takes longer to record, resulting in a larger diffusion layer above the electrode surface. In contrast, a fast scan rate leads to a smaller diffusion layer.^{132,133,135} As a consequence, the flux of ions towards the electrode surface is significantly lower at slow scan rates compared to faster rates. Since the current is proportional to the flux towards the electrode, the magnitude of the capacitive current is lower at slow scan rates and higher at high rates. It is important to note that the voltage scan rate, and hence the time taken to record the voltammogram, strongly affects the observed behaviour in LSV. Although there is no time axis displayed on the graph, the scan rate influences the results. However, it is worth noting that while the capacitive current magnitude may vary, the positions of peaks on the voltammogram remain consistent. The occurrence of peaks at the same voltage is a characteristic of electrode reactions with rapid electron transfer kinetics, often referred to as reversible electron transfer reactions.^{132,133}

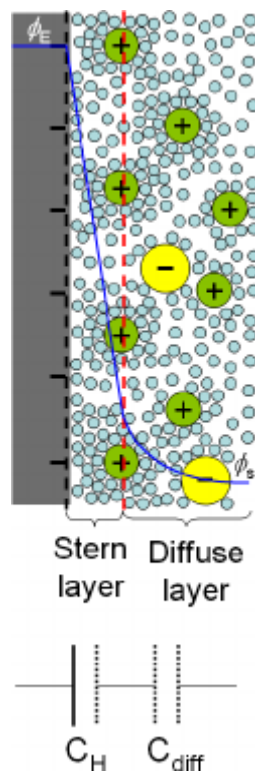


Figure 7 : Schematic representation of the Gouy-Chapman-Stern model with a diffuse layer developed into the electrolyte due to the thermal motions of electrolyte ions. Adapted from ¹³⁶ with permission from ASME.

Cyclic voltammetry (CV) shares similarities with LSV. In CV, the voltage is swept between two values at a fixed rate. The forward sweep generates a response similar to that observed in LSV. Upon reversing the scan direction, the potential sweep is simply reversed, and the current now flows from the solution species back to the electrode, opposite to the forward sweep. Following the IUPAC convention, currents occurring from oxidation processes have positive values and reduction processes show negative currents.¹³²

Especially for the observation of oxidation and reduction processes of molecular species the use of CVs is of interest. The Nernst equation (eq. 14) connects the potential of an electrochemical cell E to the standard potential of a species (E^0) and the activities of the oxidized (Ox) and reduced (Red) forms of the analyte at equilibrium. In this equation, F represents Faraday's constant, R is the universal gas constant, n denotes the number of electrons involved, and T stands for the temperature.¹³²

$$E = E^0 + \frac{RT}{nF} \ln \frac{(Ox)}{(Red)} \quad \text{Eq. 14}$$

In application of the Nernst equation the formal potential, including adjusted conditions of the system, is often used instead of the standard potential and the activities are usually replaced by the concentration in case they are sufficient low.¹³³ The Nernst equation is a useful tool for predicting how changes in species concentration or electrode potential will affect a system. In a CV experiment, as the electrode potential is varied, the concentration of species near the electrode changes over time, consistent with predictions made by the Nernst equation.¹³²

By analyzing and interpreting the shape of a CV curve the reaction at the electrode surface can be examined and understood. For a coherent interpretation of this curve identification of freely diffusing or adsorbed species involved in the electron transfer processes are important. For electrochemically reversible reaction involving freely diffusing species of the analyte the peak current i_p within the CV can be described with the Randles-Sevcik equation (eq. 15). Aside to the aforementioned and defined constants also in eq. 14, A is representing the electrode surface area, C^o is the bulk concentration of the analyte, D^o is the diffusion coefficient of the oxidized analyte and ν describes the scan rate used in the CV experiment.^{132,133}

$$i_p = 0.446nFAC^o \sqrt{\frac{nF\nu D^o}{RT}} \quad \text{Eq. 15}$$

As the Randles-Sevcik equation is showing, for freely diffusing species the peak current in a CV experiment is proportional to the square root of the scan rate. In case of the electrochemical reaction with species that are adsorbed at the electrode surface, the peak current can be described by eq. 16, with Γ representing the surface coverage of the adsorbed species and the peak current being directly proportional to the scan rate.^{132,133}

$$i_p = \frac{n^2 F^2}{4RT} \nu A \Gamma \quad \text{Eq. 16}$$

Using those these formulars the CV experiments are valuable tools for the analysis and interpretation of electrochemical reactions. The position, height and shift of the oxidation and reduction peaks within a CV provide information about the diffusion

behaviour and type of the species which is probed with the CV aswell as the surface coverage in case of adsorbed species.^{132,133}

2.3.2 Scanning droplet cell

Linear sweep voltammetry and cyclic voltammetry are valuable methods for analyzing and comparing various catalyst materials to observe their current potential behavior. These techniques provide a reliable assessment of the respective properties but are limited to analyzing one catalyst at a time. In a screening process, each catalyst needs to be deposited on the electrode surface and measured individually, which can be time-consuming for a measurement series involving multiple materials. To enable the screening of a larger number of catalysts, an automated setup would be ideal.^{129,131}

One example of such a setup is the scanning droplet cell, which is illustrated schematically in Figure 8. It consists of a conically shaped Teflon cell (6) connected to a head (5) with connections for the counter electrode (4), reference electrode (2), and a tube inlet and outlet (3) connected to a pump for controlling electrolyte flow. The tip opening of the cell can be positioned using automated step motors above a conductive sample surface, serving as the working electrode. Once the cell successfully approaches the surface, the force between the Teflon cell and the sample can be adjusted to ensure firm contact and sealing. The electrode surface area is defined by the diameter of the tip opening. After each measurement, the electrolyte is replaced with fresh electrolyte, and the cell automatically moves to another position on the wafer. This allows for the automatic acquisition of electrochemical data at different spatially resolved locations on the sample surface, utilizing a wide range of electrochemical techniques. By examining the trend in the generated activity data curves, the influence of the sample's composition on the film activity can be determined. In addition, it is feasible to incorporate a light source (1) within the scanning droplet cell (SDC) head to induce photo currents through photocatalytic reactions.^{137,138}

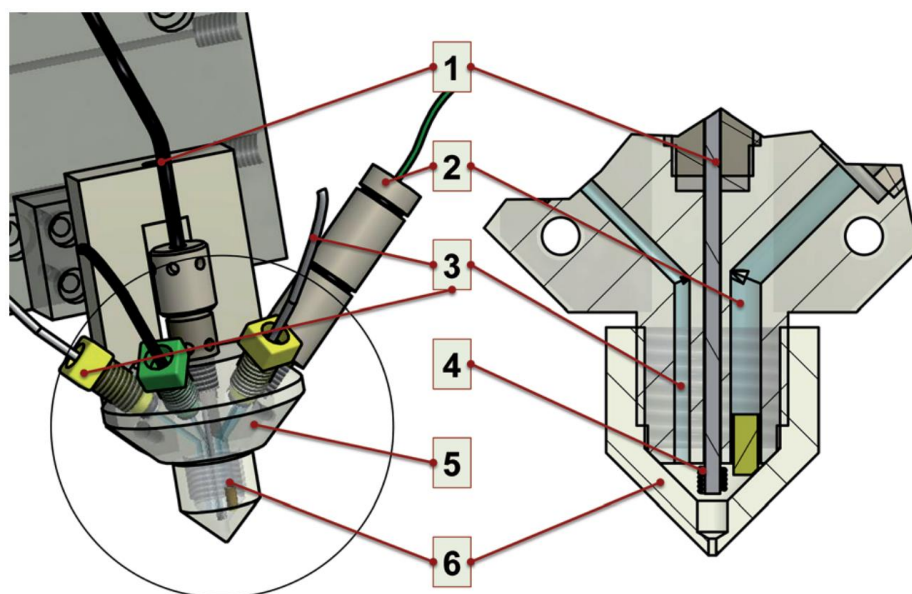


Figure 8: Schematic illustration of the Optical Scanning Droplet Cell (OSDC) setup, showing the components: (1) Optical fiber, (2) integrated double-junction Ag/AgCl/3M KCl reference electrode, (3) electrolyte in- and outlets, (4) Pt-wire counter electrode, (5) PMMA body, and (6) PTFE capillary tip. Adapted from ¹³⁷with permission from Wiley.

SDC is widely utilized by various research groups for the screening of materials targeting different electrochemical reactions.^{77,130,137–141} One common approach involves analyzing material libraries consisting of spatially distributed compositions on a single sample. These material libraries can be fabricated using various methods, including inkjet printing,¹⁴² electrodeposition,¹⁴³ physical vapor deposition (e.g. co-sputtering),^{12,78,80} or drop casting.¹⁴⁴ The use of material libraries allows for the rapid screening of a large number of different material compositions, enabling efficient exploration of catalytic properties and reaction performance.

In recent years, SDC technology has been employed for analyzing materials suitable for photocatalytic reactions. Gregoire et al. conducted a study using SDC to analyze thin-film catalyst libraries (Fe-Co-Ni-Ti)O_x, which were fabricated using inkjet printing. The study involved a total of 5456 unique sample compositions. Various techniques, including cyclic voltammetry and chronoamperometry, were performed under light exposures to evaluate the catalytic activity for OER.¹⁴⁵ Similar methods were used by Schäfer et al.¹³⁸ as well as Meyer et al.¹⁴⁶ who both analyzed thin film material libraries sputtered in a co-sputtering process. Schäfer et al. focused on the electrocatalytic ORR using (Ti/Nb)O_x covered with a Pt layer. On the other hand, Meyer et al. investigated the photoelectrochemical current on (FeW)O_x with the SDC.

In addition to employing high-throughput electrochemical methods, some research groups have started to utilize coupled analysis techniques in combination with SDC measurements. This approach aims to expand the range of information obtained from the high-throughput data. The research group led by Karl Mayrhofer employed a SDC with an additional electrolyte output to transform the cell into a scanning electrochemical flow cell. This innovative technique allowed the detection of products from electrochemical measurements, expanding the information obtained beyond traditional electrochemical data. To achieve this, they coupled the SDC with an inductively coupled plasma mass spectrometer (ICP-MS), which analyzed the electrolyte after the electrochemical measurements. By using this approach, they successfully detected and analyzed various products, such as copper dissolution during corrosion experiments,¹⁴⁷ hydrogen evolution during water electrolysis, and different products during CO₂ reduction.^{139,140} Jenewein et al. employed a similar approach, utilizing a scanning flow cell coupled with an ICP-MS. Their study focused on the analysis of Fe-Ni and (Fe-Ni-Co)O_x material libraries, specifically investigating the activity for the OER, as well as the dissolution of the catalyst and its stability during the reaction.¹³⁰

2.3.3 Scanning electrochemical cell microscopy

Conventional electrochemical analysis methods like RDE and RRDE have a limitation as macroscopic characterization technique. They can only provide information about the bulk properties of the materials. However, a catalyst film on an electrode consists of numerous active sites of varying types, and RDE and RRDE measurements can only provide an average activity value.¹⁴⁸ Furthermore, the properties of the catalyst film, including layer thickness, surface area, and porosity, can significantly impact the observed activity.¹⁴⁹

In order to obtain a thorough understanding of electrochemical systems, it is essential to utilize techniques capable of probing nanoscale aspects of electrocatalysts. The exploration of complex spatiotemporal dynamics at electrochemical interfaces plays a critical role in addressing both fundamental and practical inquiries, particularly in catalyst material research. A promising scanning probe technique, known as scanning electrochemical cell microscopy, has emerged as an effective method for directly and swiftly investigating nanoscale regions on a target surface with exceptional precision.^{15,150–152}

SECCM (Scanning Electrochemical Cell Microscopy) is a scanning probe technique similar to SDC that utilizes a mobile droplet to perform electrochemical characterizations of surfaces. However, there are key differences between SECCM and SDC. One distinction is the size, as the SECCM probe can be miniaturized to dimensions below 50 nm.^{102,150} Another difference is that the hanging drop in SECCM is not confined after the approach, unlike in SDC. SECCM was first introduced and extensively developed by the research group led by Patrick Unwin.¹⁵³ In SECCM, a mobile meniscus is brought into contact with the sample surface using an electrochemical feedback loop. This meniscus forms an electrochemical cell, enabling localized electrochemical measurements. The scanning strategy in SECCM involves performing arrays of measurements through a hopping scanning regime. The hopping scanning regime in SECCM allows for the application of various electrochemical methods. After each measurement, the meniscus is completely detached from the surface and then repositioned to an adjacent area without overlapping with previously contacted areas. This approach ensures high-quality, statistically relevant, and independent electrochemical measurements. Additionally, the contacted area or meniscus footprint can often be visualized and analyzed after a scan, for example,

using scanning electron microscopy. One significant advantage of the hopping mode in SECCM is that it allows for the effective investigation of sites of interest on rough surfaces while minimizing the risk of tip crash. This makes SECCM a highly robust and versatile technique for electrochemical analysis.^{150,154–157}

SECCM can utilize either a single barrel or dual barrel pipette as a probe. The electrode preparation process is similar for both configurations, involving the fabrication of capillaries with different tip opening sizes using a laser puller. The main difference lies in the type of feedback employed to detect the approach to the surface and the required instrumentation for feedback reading. In the case of a dual barrel configuration, a bias potential (U_1) is applied between the two barrels to generate a direct ion current (I_1) across the meniscus (Figure 9a). This I_1 is monitored to determine the positioning of the droplet. When the droplet contacts the surface, there is a change in the I_1 due to the altered size and shape of the meniscus. Fine control over positioning and the pipette-sample distance is typically achieved by operating in the AC mode. In this mode, the dual barrel probe is vertically modulated at a specific frequency using a sinusoidal signal generated from a lock-in amplifier. The resulting oscillations cause the meniscus to vibrate, converting the initially described I_1 into an alternating current. The lock-in amplifier extracts the magnitude and phase of this alternating current to accurately position the meniscus over the sample. This approach is particularly useful for samples with lower conductivity. The potential U_1 is used to regulate the driving force for electrochemical reactions, while the working electrode current (I_2) is measured as the electrochemical signal.^{153,158–162}

For the single barrel probe (Figure 9b), a small bias is applied between the quasi-reference counter electrode (QRCE) and the working electrode surface. Upon contact with the surface, a change in I is used as feedback to halt further translation. Although single barrels do not provide complete control over the meniscus geometry, the instrumentation is relatively straightforward, and the feedback loop can be detected more rapidly. This allows for the implementation of faster scanning protocols.^{102,103}

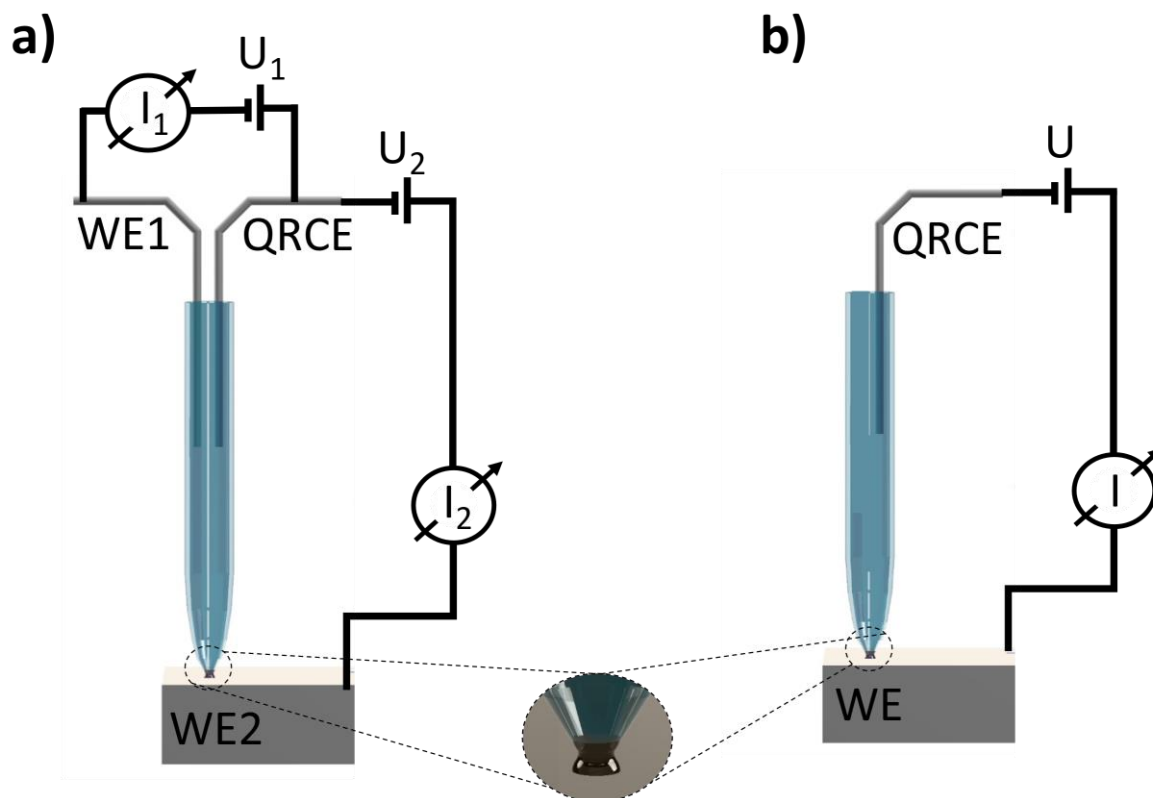


Figure 9: SECCM in a) double barrel configuration and b) in single barrel configuration.

SECCM, as a highly effective characterization technique with exceptional lateral resolution, has been extensively employed for imaging electrochemical processes on heterogeneous surfaces. The primary emphasis of numerous SECCM investigations has been to visualize and understand the electrochemical behavior occurring at these complex surfaces.^{163–167} The independent nature of SECCM hopping mode measurements allows for the generation of statistically significant datasets, with the capability to perform up to thousands of measurements in a short period of time.^{102,164,166,168} These large electrochemical datasets can be visualized as maps or movies, providing information on the local electrochemical activity across the sample surface.¹⁰⁴ Furthermore, these datasets can be correlated with structural information obtained from characterizations performed at the same locations such as AFM,^{169,170} Raman spectroscopy,¹⁷¹ XPS,¹⁷⁰ EBSD^{150,172} or SEM^{165,173,174}. This ability to establish structure-activity correlations is valuable in various disciplines, including electrocatalysis,^{102,175–181} crystallization,^{182,183} corrosion,¹⁸⁴ and batteries^{185–188}. By linking the electrochemical behavior to the underlying structure, insights into the functional properties and performance of materials can be gained.

The utilization of the SECCM is primarily concentrated in the realm of nanomaterials, specifically aimed at exploring the inherent properties of these materials. Its application is centered on the investigation of nanomaterials, enabling a comprehensive examination of their fundamental characteristics. SECCM facilitates the in-depth analysis of nanomaterials, unraveling their unique traits and behaviors at the nanoscale. This advanced technique provides researchers with valuable insights into the intricate details and distinctive aspects of nanomaterials, fostering progress in this field of research. The SECCM can be employed to investigate nanomaterials through the utilization of local ensemble measurements. In this method, the pipette probe is utilized to encapsulate and examine individual nanoparticles or small groups of particles that are situated on an electrochemically inert working electrode surface. Initial SECCM experiments utilizing ensemble measurements and encapsulating multiple nanoparticles employed relatively large probe sizes (30 μm). These studies focused on analyzing the activity of Pt nanoparticles on single-walled nanotubes for the ORR.¹⁸⁹ This investigation enabled the analysis of the pristine state of the particles. Subsequent studies applied similar methodologies to Ni(OH)₂-decorated carbon nanotubes for ORR activity, allowing for differentiation between the alpha and beta phases of Ni(OH)₂.¹⁹⁰ Tarnev et al. conducted an example analysis of smaller nanoparticles, specifically (ZIF-67) particles, to investigate their activity towards the OER.¹⁷³ This study demonstrated that the OER current correlated with the number of nanoparticles within the encapsulated SECCM meniscus spot, while the turnover frequency slightly decreased. Quast et al. also employed a similar approach to analyze multiple Co₃O₄ nanocubes for the OER within the SECCM meniscus, and intrinsic activity comparisons were made using single-particle-on-nanoelectrode measurements.¹⁷⁴

Electrochemical imaging is another configuration of the SECCM, where spatially resolved measurements are conducted in a sequential manner at predetermined points across the surface of the sample. This approach enables the creation of a map depicting the distribution of electrochemical activity on the sample surface. This approach allows for the investigation of nanoparticles, nanosheets, and other nanostructures. Initial investigations focusing on electrochemical mapping of nanoparticles using the hopping mode were carried out by Takahashi et al.¹⁹¹ They conducted a study mapping the redox activity of LiFePO₄, a crucial parameter in

lithium-ion batteries.¹⁹¹ Subsequent studies on the same particles revealed variations in the redox activity of individual particles, which were attributed to differences in their crystal structures.¹⁹² In this particular study, the SECCM configuration was utilized within a glovebox to maintain an inert atmosphere when working with Li-based materials. In the field of electrocatalysis, Au nanoparticles have been frequently employed as a subject of investigation in SECCM studies. Bentley et al. utilized high-speed and high-resolution hopping mode techniques with probe sizes of 30 nm to analyze both polycrystalline and well-defined {111}-oriented Au nanoplates.^{193,194} While the average electrochemical response was similar for all particles, individual electrochemical experiments within a single particle exhibited variations, suggesting the presence of sub-particle structural crystallographic heterogeneity.

Within the realm of nanosheets, significant research interest lies in the class of 2D materials discussed in earlier chapters. Graphene nanosheets, in particular, were among the first 2D nanomaterials to be investigated using electrochemical imaging with SECCM.¹⁹⁵ Studies focused on the reactions of various redox mediators, revealing differences between $\text{FcTMA}^{+/2+}$ and $[\text{Ru}(\text{NH}_3)_6]^{3+/2+}$ for different layer thicknesses. SECCM has been applied in the analysis of graphene, particularly in examining the effects of N/P co-doped holey graphene nanosheets.¹⁹⁶ The research showed that the presence of holes in the graphene lattice generated active sites for the HER. Moreover, the introduction of doping led to an enhancement in the catalytic activity, which was attributed to the modification of edge structures following the doping process.¹⁹⁶

As previously mentioned, SECCM has been utilized by several research groups to investigate MoS_2 , providing insights into the identification of active sites for the HER and their impact on the overall catalytic activity.^{102,104} SECCM has also been applied to study other TDMCs, including WSe_2 . In these studies,¹⁹⁷ the local photoelectrochemical activity of WSe_2 was investigated using a light source that was directed through a transparent substrate. The findings revealed that the electron transfer rate was influenced by the thickness of the nanosheets. It was attributed to the limited ability of thin nanosheets to support independent space charge layers, leading to variations in the electron transfer kinetics.

The SECCM exhibits a wide spectrum of capabilities, ranging from the generation of statistically evident datasets to the exploration of intrinsic properties in materials. It

serves as a versatile and robust measurement system, enabling comprehensive investigations across different research areas.

3. Motivation and aim of the work

In the research to find efficient, sustainable and environmentally friendly energy sources and storage possibilities, the quest to find an optimal catalyst for different kind of electrochemical reactions is present. Nevertheless, the systematic screening of potential materials is hindered by the low throughput of manual or conventional measurement methods. To overcome this limitation, automated synthesis and screening techniques employing combinatorial methodologies have been developed. These approaches enable accelerated investigations into the effects of composition and structure on materials performance. By combining high-throughput preparation methods with high-throughput screening, a large number of different materials can be efficiently explored, facilitating the search for materials that meet the desired specifications.

As discussed in Chapter 2, HEAs have demonstrated efficient catalytic activity for various electrocatalytic reactions, including the HER and ORR. However, the challenge lies in identifying catalysts with optimized activity, given the vast number of potential element combinations and compositions. To address this challenge, high throughput measurement techniques are essential for conducting experiments within a reasonable timeframe to discover efficient catalysts. The initial step in high throughput screening of HEAs involves strategically selecting a starting point. This work presents two different approaches for identifying catalysts based on HEAs.

In the first approach, a catalyst comprising (TiNi)-Cu-Hf-Pd-Zr was employed for the HER and ORR, both being significant electrochemical reactions in energy conversion. This element combination consists of established electrocatalytic elements and less commonly used elements, with the intention of leveraging synergistic effects to enhance activity.

In the second approach, a previously reported HEA composition, Co₃₅Cr₁₅Fe₂₀Mo₁₀Ni₂₀, was chosen as a starting point. This composition had been identified by Zhang et al.⁵⁵ as an efficient catalyst for the HER. Over 1000 different HEA compositions were synthesized using co-sputtering to create three material libraries. These compositions were then analyzed using SDC measurements to identify HEA compositions within the CoCrFeMoNi space exhibiting higher activities and to determine composition trends associated with enhanced activity.

As outlined in chapter 2, conventional techniques such as RDE or RRDE measurements provide information about the bulk properties of materials and offer averaged activity of the catalyst film on an electrode. However, these techniques are limited in their ability to identify and analyze the intrinsic activity of individual active sites. Understanding the underlying processes responsible for catalyst activity requires the characterization and analysis of intrinsic activity, which goes beyond the scope of macroscopic characterization techniques.

SECCM measurements were performed to analyze the spatially resolved activity of thin film MoS₂ flakes. These flakes were synthesized via chemical vapor deposition (CVD) on a non-conductive substrate and subsequently transferred to a glassy carbon support. The aim was to investigate the catalytic activity of these larger-sized MoS₂ flakes compared to previous studies in the literature. The SECCM setup used in the research group was optimized and rebuilt to improve sensitivity and signal-to-noise ratio.

Lastly, the influence of stress in catalyst films on catalytic activity was studied. A stress chip, capable of measuring stress in films on cantilevers, was utilized as a support for Pt films. Pt was chosen as a model catalyst to assess the functionality of the setup. The electrochemical analysis was performed using SECCM. This part of the project involved integrating the stress chip into the SECCM setup and designing a holder system to induce bending of the cantilevers on the stress chip during SECCM measurements. The subsequent analysis aimed to measure and evaluate the impact of stress in the thin film on the stress chip on catalytic activity.

4. Results and discussion

4.1 High entropy alloy compositions spreads on material libraries

Two distinct combinations of high entropy alloys (HEAs), namely (TiNi)-Cu-Hf-Pd-Zr and Co-Cr-Fe-Mo-Ni, were subjected to analysis using the SDC technique. The resulting data was carefully examined and interpreted, leading to the publication of two research papers in peer-reviewed journals at the time of writing this thesis. The findings and contributions from these studies are presented in two separate subchapters, with the division of individual contributions outlined at the beginning of each respective subchapter.

4.1.1 (TiNi)-Cu-Hf-Pd-Zr

The following subchapter covers the studies of Krysiak and Schumacher et al.¹⁹⁸ Parts of the text or paraphrases were taken from ¹⁹⁸. Also, it covers the studies that were addressed within the scope of the DFG project “Exploring high-entropy alloys for the hydrogen evolution reaction in alkaline electrocatalysis: from compositional screening to strain effects - AN 1570/2-1” from the research groups of Prof. Dr. Corina Andronescu and Prof. Dr. Alfred Ludwig. The contribution in this study is divided as follows. SDC measurements were performed, and electrochemical data was analyzed and interpreted by Olga Krysiak (O.K.) and Simon Schumacher (S.S), O.K. being responsible for ORR measurements and S.S. for HER measurements. Fabrication and characterization of the MLs were performed by Alan Savan. Writing of the original manuscript draft was done by O.K. and S.S. Conceptualization, providing resources, supervision and project administration are attributed to Wolfgang Schuhmann, Alfred Ludwig and Corina Andronescu. Further data interpretation, discussion as well as review and editing of the manuscript were done by all coauthors.

Considering the vast number of possible combinations of elements and their relative concentrations in HEAs, it is crucial to employ high-throughput screening methods to analyze the effects of composition, structure, and catalysis. These methods are essential for identifying potential catalysts with desirable electrocatalytic properties. By utilizing thin-film MLs containing continuous composition spreads of HEAs, where each constituent element ranges from about 10 at.% to 35 at.%, along with rapid electrochemical screening techniques such as the scanning droplet cell, a better understanding of the interactions and unexpected properties exhibited by quinary

element mixtures can be achieved. Additionally, this approach facilitates the efficient identification of suitable electrocatalysts for various reactions.^{138,139}

It is also valuable to include elements in unconventional combinations that have not been explored before due to the poor performance of individual elements. However, such combinations might contribute to synergistic effects in CCSS and consequently enhance electrocatalytic activity. Selecting an elemental composition as a starting point for high-throughput screening, without prior knowledge of how the interactions in a CCSS will influence the measured properties, particularly catalytic activities, remains a challenge. One approach is to start from known active metals or binary mixtures and assume that the combination of their properties will be relevant for the activity of HEAs based on five or six elements. Although this approach seems knowledge-driven, it falls short due to the complex and unknown interactions among different parameters. The alternative approach involves starting with a combination of metals, such as those with high activity for certain reactions, and another class of metals typically used as support materials in heterogeneous catalysis. In this study, latter approach is adopted.¹⁹⁸

In this study the composition-dependent activities of the hexanary system (TiNi)-Cu-Hf-Pd-Zr for the ORR and HER in alkaline media were investigated. These reactions were selected as model reactions due to their significance in the field of energy conversion. The choice of elements was based on the intention to expand the range of elemental compositions tested for catalytic activity by combining commonly used catalytic metals (Ni, Cu, Pd) with elements that are not typically considered promising electrocatalysts (Hf, Zr, Ti).

Two thin-film MLs (ML1 and ML2), generated using combinatorial co-sputtering from five confocal targets, exhibited nearly identical composition spreads. The sputtering process is described in more detail in chapter 6. The distinctions between ML1 and ML2 were limited to approximately 1 atomic percent (at.%) of specific elements. To analyze the electrochemical properties of various elemental compositions, a SDC was employed in 0.1 M KOH electrolyte. A detailed description of this analytical device and the measurement procedure can be found in chapter 6. This high-throughput electrochemical technique allowed the assessment of activity at 342 discrete measurement areas (MAs) within the ML, generating a data map that correlates electrochemical response with controlled composition trends. By maintaining

consistent measurement conditions and ensuring high data accuracy and reliability through automated non-manual operation, valid comparisons of activity between different MAs were made.

Considering the potential surface oxidation of compositions containing Ti, Hf, and Zr, the start potential of the LSV was adjusted to prevent oxide formation. The focus was on reduction reactions where any surface-oxidized species would be re-reduced before reaching the potential range of the investigated reactions. Figure 10 displays electrocatalytic activity maps, which plot measured current values at specific potentials in relation to the location on the ML. A potential of 570 mV vs RHE was chosen for the ORR, while a potential of -700 mV vs. RHE was selected for the HER. This visualization allowed observation of activity changes throughout the studied composition space, revealing both general trends and the location of high-activity regions. For ORR, activity increased from the upper end of ML1 to the lower end, with three highly active regions situated on the center-left side of the ML. Conversely, for HER, the general trend indicated increased activity along the diagonal from the upper right side to the lower right side, with the high-activity area located on the upper left side of ML2. The lower panel of Figure 10 exhibits the measured LSVs for ORR and HER at selected MAs from regions with different activities (marked with squares in Figure 10).

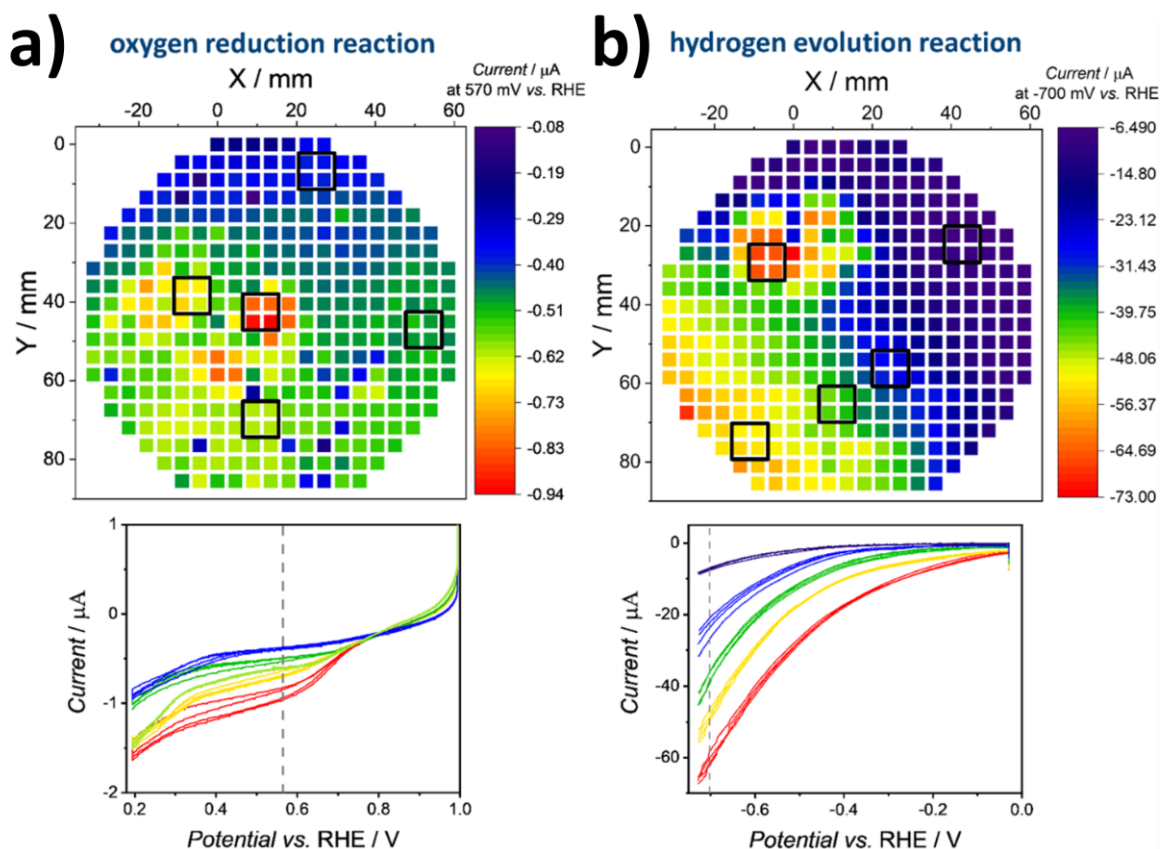


Figure 10: Comparison of activity maps obtained for the ORR (a) and the HER (b). Individual LSVs of the selected MAs characterized by different electrochemical activities (indicated by squares) are presented on the bottom part of the figure. For the ORR the current at 570 mV vs. RHE and for the HER the current at -700 mV vs. RHE (dashed lines) were selected as the measure of activity¹⁹⁸

To eliminate the possibility of systematic errors introduced by the automated measurement setup, we conducted a second measurement of the material library (ML) after physically rotating it by 90° (Figure 11). By comparing the results obtained before and after the rotation, we were able to verify that the observed changes in activity were indeed associated with the variations in the composition of the ML. This further supports the conclusion that the observed differences in activity are directly influenced by the specific compositions of the material library rather than any experimental artifacts.

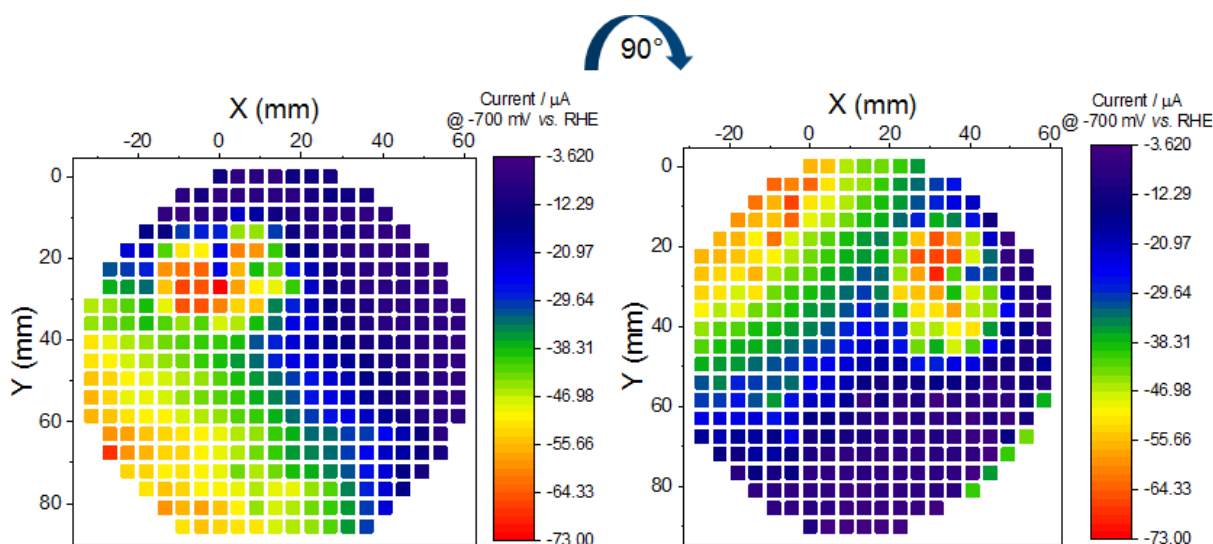


Figure 11: Electrochemical activity maps obtained by plotting the current at -700 mV vs. RHE measured on ML2 initially, and then subsequently after physical rotation of the sample by 90°. ¹⁹⁸

The highest activity for ORR was observed in a small cluster located at the center of ML1, corresponding to the composition Ti₁₄Ni₁₇Cu₁₆Zr₂₁Pd₁₇Hf₁₅. Furthermore, the activity appeared to be enhanced with higher amounts of Ti and Ni, and slightly improved with increased Cu content. It is worth noting that the recorded LSV curves for ORR exhibited a multi-wave shape characteristic of high-HEAs, as described theoretically¹⁹⁹ and confirmed experimentally.²⁰⁰ The random arrangement of elements in a CCSS leads to a continuous and distinct adsorption energy distribution pattern. When considering only on-top adsorption of reaction intermediates, the number of adsorption peaks corresponds to the number of elements, with each peak representing active sites containing a specific element at the center. However, when active sites formed by two or three atoms are considered, the number of adsorption peaks increases along with the number of possible centers. Each of these multiple adsorption peaks generates a current curve, whose activity depends on the peak's position relative to the optimal binding energy. The intensity of the current curves is determined by the molar ratio of elements, with activity influenced by the difference in peak position from the optimal binding energy. In some cases, electrochemical response waves corresponding to each adsorption peak may not be visible in the LSV due to low activity and high overpotentials. Consequently, plotting activity maps at different potentials can provide additional insights into catalytic activity.

As shown in the top panel of Figure 12 a) and b), plotting the activity map of ML1 at 820 mV reveals an opposite trend compared to 570 mV. At higher potentials, activity increases with higher amounts of Ni and Ti, whereas at lower potentials, activity

increases with decreased amounts of Ni and Ti and increased Pd content. Additionally, the small high-activity region near the center of the ML is no longer visible at 570 mV vs RHE. These results can be explained by the multi-wave shape of the LSV plots. The potential of 820 mV vs RHE falls within or close to the catalytic region of the first wave, while the potential of 570 mV vs. RHE corresponds to the second wave. This indicates that adsorption sites containing Cu, Ni, and Ti are responsible for the first wave, while the second wave corresponds predominantly to adsorption sites containing Pd, Hf, and Zr.

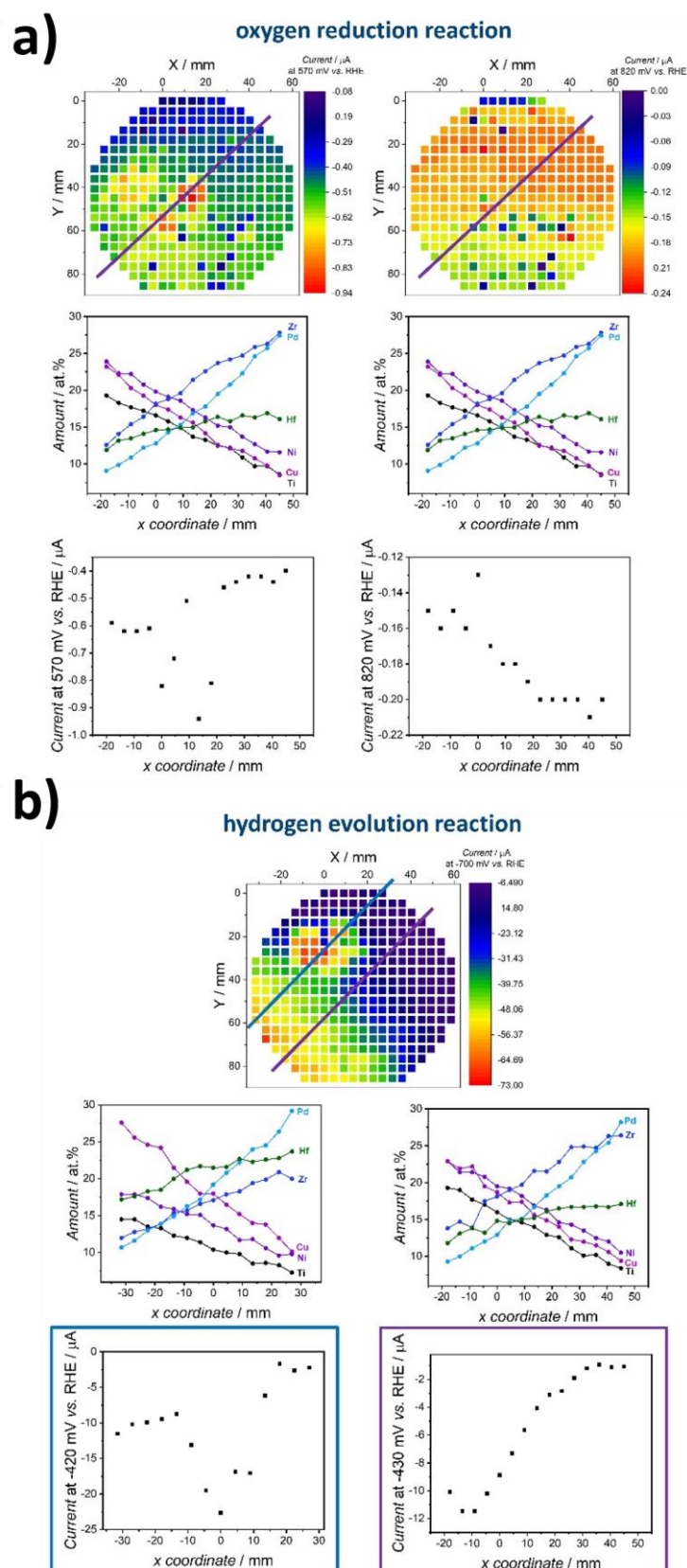


Figure 12: a) and b) showing further data interpretation for ORR and HER, respectively. Correlation of the amount of each element (middle row) at each of the measurement areas marked with the lines on MLs (top row) and the measured current at 570 mV and 820 vs. RHE for ORR and at -700 mV for HER (bottom row). Lines indicated in the activity maps (top row) determined the MAs used for this analysis, represented by their x coordinate.¹⁹⁸

Regardless of the potential at which the activity map is measured (Figure 13), the overall trend for the HER remains consistent. The activity increases from the upper right side of the ML (starting from the high Pd content) to the lower left side (higher Ti, Ni, and Cu content), and a high-activity area is observed at relatively high levels of Hf and Pd (around 20 at.% to 25 at.%). Interestingly, this upward trend in activity along the diagonal of the ML is contrary to the Pd content, which is known to be an efficient HER catalyst.²⁰¹ This finding suggests that the synergistic interactions among all the elements present in the HEAs are more significant for electrocatalytic activity than the individual element content. In the analyzed ML, the active sites containing mainly Cu, Ti, and Ni exhibit the highest activity. Alongside the diagonal activity trend, a narrow cluster with higher activity is situated at the center, slightly shifting toward the region with higher Hf content. This observation supports the notion of possible synergistic interactions contributing to the catalyst's activity since Hf is not typically recognized as a highly active HER catalyst. The composition Ti₁₁Ni₁₃Cu₁₈Zr₁₇Pd₁₉Hf₂₂ demonstrates the highest activity for HER.

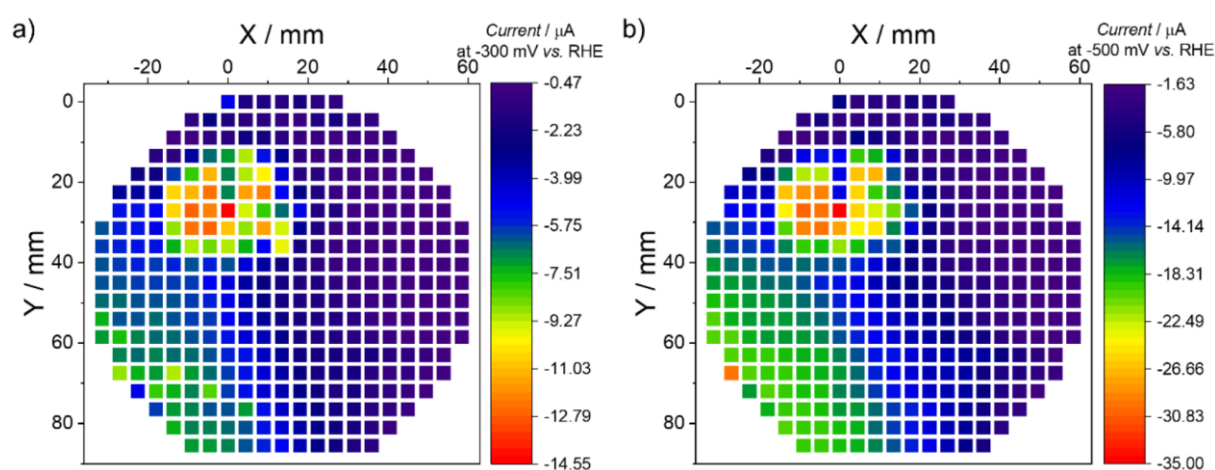


Figure 13: HER activity maps of ML2 at a) -300 mV vs RHE and b) -500 mV vs RHE.¹⁹⁸

In conclusion, several key findings emerge from this subchapter. By combining elements commonly used in catalysis (Cu, Ni, Pd) with elements typically employed as support materials (Ti, Hf, Zr), previously unknown and unexpected compositions that exhibit remarkable activity for the HER and ORR could be discovered. Interestingly, the presence of supposedly non-active elements is essential for achieving these high activity levels. It is noteworthy that different compositions, characterized by varying relative amounts of the elements, enhance different electrocatalytic reactions. In the case of the ORR, the variation in Ti and Ni content plays a crucial role in determining

the activity, while for the HER, decreasing Pd content and a specific cluster within the material library exhibit higher activity. Due to the immense complexity arising from the countless possible compositions and unknown physico-chemical interactions, screening large numbers of material libraries is the only viable approach to unravel this complexity. The resulting extensive and expanding datasets will serve as a valuable foundation for machine learning techniques, enabling improved predictions and the identification of optimal starting compositions in future studies.

4.1.2 Co–Cr–Fe–Mo–Ni

The following subchapter covers the studies of Schumacher and Baha et al.²⁰² Parts of the text or paraphrases were taken from ²⁰². Also it covers the studies that were addressed within the scope of the DFG project “Exploring high-entropy alloys for the hydrogen evolution reaction in alkaline electrocatalysis: from compositional screening to strain effects - AN 1570/2-1” from the research groups of Prof. Dr. Corina Andronescu and Prof. Dr. Alfred Ludwig. The contribution in this study is divided as follows. SDC measurements were performed, and electrochemical data was analyzed by Simon Schumacher (S.S). Fabrication and characterization of the MLs were performed by Sabrina Baha (S.B.) and Alan Savan. Writing of the original manuscript draft was done by S.S. and S.B. Conceptualization, providing resources, supervision and project administration are attributed to Alfred Ludwig and Corina Andronescu. Further data interpretation, Review and editing of the manuscript were done by all coauthors.

The Co-Cr-Fe-Mo-Ni CCSS (Combinatorial Co-Sputtering System) was investigated as a potential source of new electrocatalysts for the HER in an alkaline environment. The exploration began by focusing on a nearly equiatomic composition, which served as the center point of the first material library (ML1). From this starting point, the composition range expanded linearly in five different directions on the ML. Additionally, ML2 and ML3 introduced new center points, further extending the composition space. ML3 specifically included the composition previously reported by Zhang et al.⁵⁵ By utilizing high-throughput X-ray diffraction (XRD) and energy dispersive X-ray spectroscopy (EDX) characterization techniques, over 1000 different CCSS compositions were analyzed. Furthermore, high-throughput screening of electrocatalytic activity for HER using voltammetry in a SDC was employed. As a result, numerous Co-Cr-Fe-Mo-Ni CCSS compositions were identified that exhibited significantly higher electrocatalytic activity compared to those reported in the literature.⁵⁵

The chemical compositions of 342 measurement areas (MAs) on each ML are depicted in Figure 14, providing a comprehensive overview of the three libraries. The MAs are arranged in a well-defined manner, with the first MA starting from the lower-left corner and progressing from left to right. The final MA, MA342, is located at the top-right

corner of the ML. The center points of each ML, namely ML1-MA168, ML2-MA168, and ML3-MA167, possess chemical compositions of $\text{Co}_{20}\text{Cr}_{24}\text{Fe}_{14}\text{Mo}_{21}\text{Ni}_{21}$, $\text{Co}_{43}\text{Cr}_{12}\text{Fe}_{31}\text{Mo}_5\text{Ni}_9$, and $\text{Co}_{36}\text{Cr}_{16}\text{Fe}_{20}\text{Mo}_8\text{Ni}_{20}$, respectively.

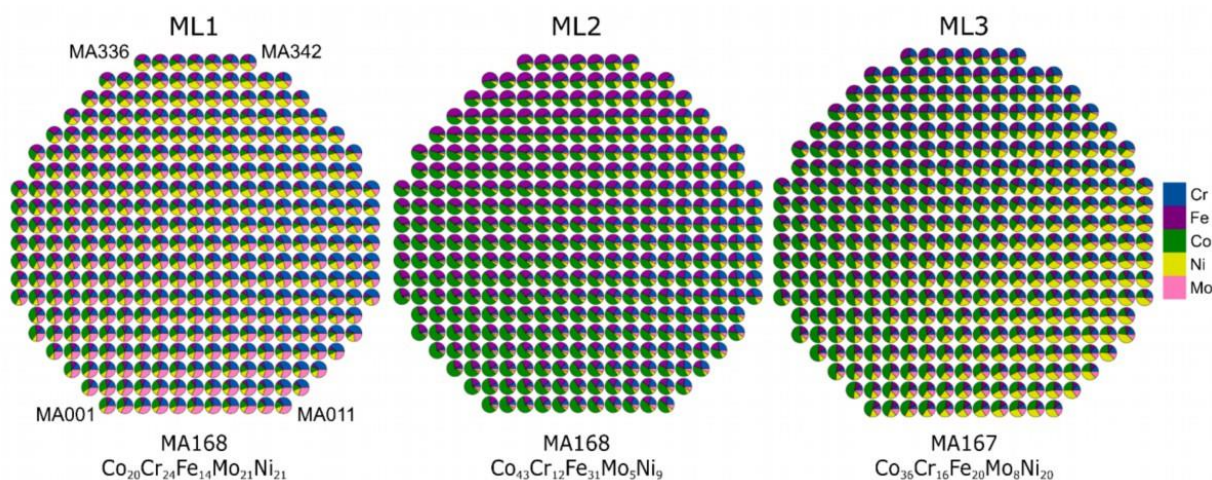


Figure 14: Composition ranges of the MLs, measured by EDX in at%. The composition of each of the 342 MAs in the synthesized MLs is visualized as a color-coded pie chart. The measured composition in the respective center of the ML: ML1-MA168 $\text{Co}_{20}\text{Cr}_{24}\text{Fe}_{14}\text{Mo}_{21}\text{Ni}_{21}$, ML2-MA168 $\text{Co}_{43}\text{Cr}_{12}\text{Fe}_{31}\text{Mo}_5\text{Ni}_9$ and ML3-MA167 $\text{Co}_{36}\text{Cr}_{16}\text{Fe}_{20}\text{Mo}_8\text{Ni}_{20}$. The numbering of the MA starts at MA001 and runs from left to right, so that the last MA is MA342 in the upper right corner²⁰²

Despite synthesizing and characterizing over 1000 compositions, it is important to note that the explored composition space remains limited compared to the vast number of possibilities offered by the quinary system. To visualize this, Figure 15 provides a schematic representation of the 5D space for ML1 (pink), ML2 (yellow), and ML3 (blue) in both 2D and 3D projections. The projections depict two different configurations of the deposition sources and offer a better understanding of the 5D element space. Figure 15 b) and c) highlight that ML1 and ML2 do not overlap in their compositions. Furthermore, in all the figures, ML3-MA167 is marked with a green point, representing a CCSS composition that closely resembles a composition previously reported in the literature as an active HER electrocatalyst.⁵⁵

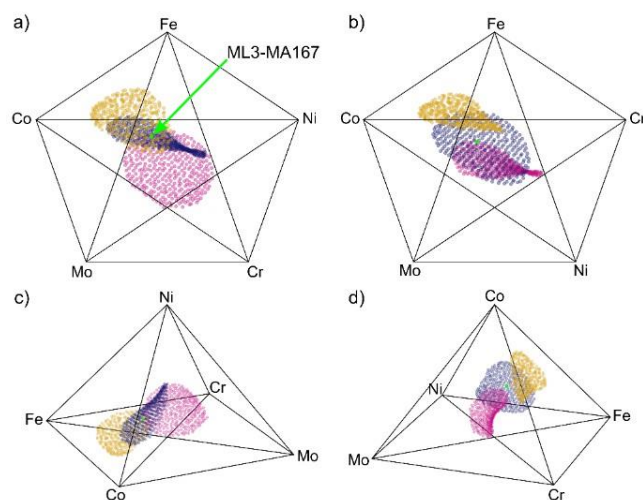


Figure 15: Representation of the 5D space as (a) and (b) 2D projections and (c) and (d) 3D projections of ML1 (pink), ML2 (yellow) and ML3 (blue). The green point in a) represents the composition $\text{Co}_{36}\text{Cr}_{16}\text{Fe}_{20}\text{Mo}_8\text{Ni}_{20}$ (ML3-MA167), which was reported⁵⁵ as a HER catalyst. Two different configurations of the deposition sources were chosen to visualize the 5D elemental space.²⁰²

Figure 16 showcases the electrocatalytic HER activity as activity maps derived from the electrochemical measurements, along with selected electrocatalytic and compositional trends for each ML. The respective MAs from the three MLs are plotted based on the measured current at a potential of -250 mV vs RHE, with a specific color range utilized for visualization. The extensive evaluation of MAs allows for the identification of activity trends as a function of composition without any interpolation or data manipulation. The white areas in Figure 16 a) indicate MAs where no faradaic current could be recorded or extracted due to technical issues, such as gas bubble formation leading to cell disconnection and noisy current recordings. Upon comparing the activity maps at -250 mV vs RHE, it becomes evident that MAs with higher electrocatalytic HER activity are present on ML2 and ML3, surpassing those on ML1. Each activity map features a black arrow pointing from the MA with the lowest recorded current at -250 mV vs RHE to the MA with the highest current, illustrating the trend in electrocatalytic HER activities (Figure 16 a). While the trend is pronounced for ML2 and ML3, it is less apparent for ML1. Consequently, for ML1, measurements of current at a higher overpotential (-400 mV vs RHE) were conducted. The results of electrocatalytic HER activity (Figure 16 b) and the corresponding elemental compositions (Figure 16 c) are plotted for individual MAs along the arrow shown in Figure 16 b).

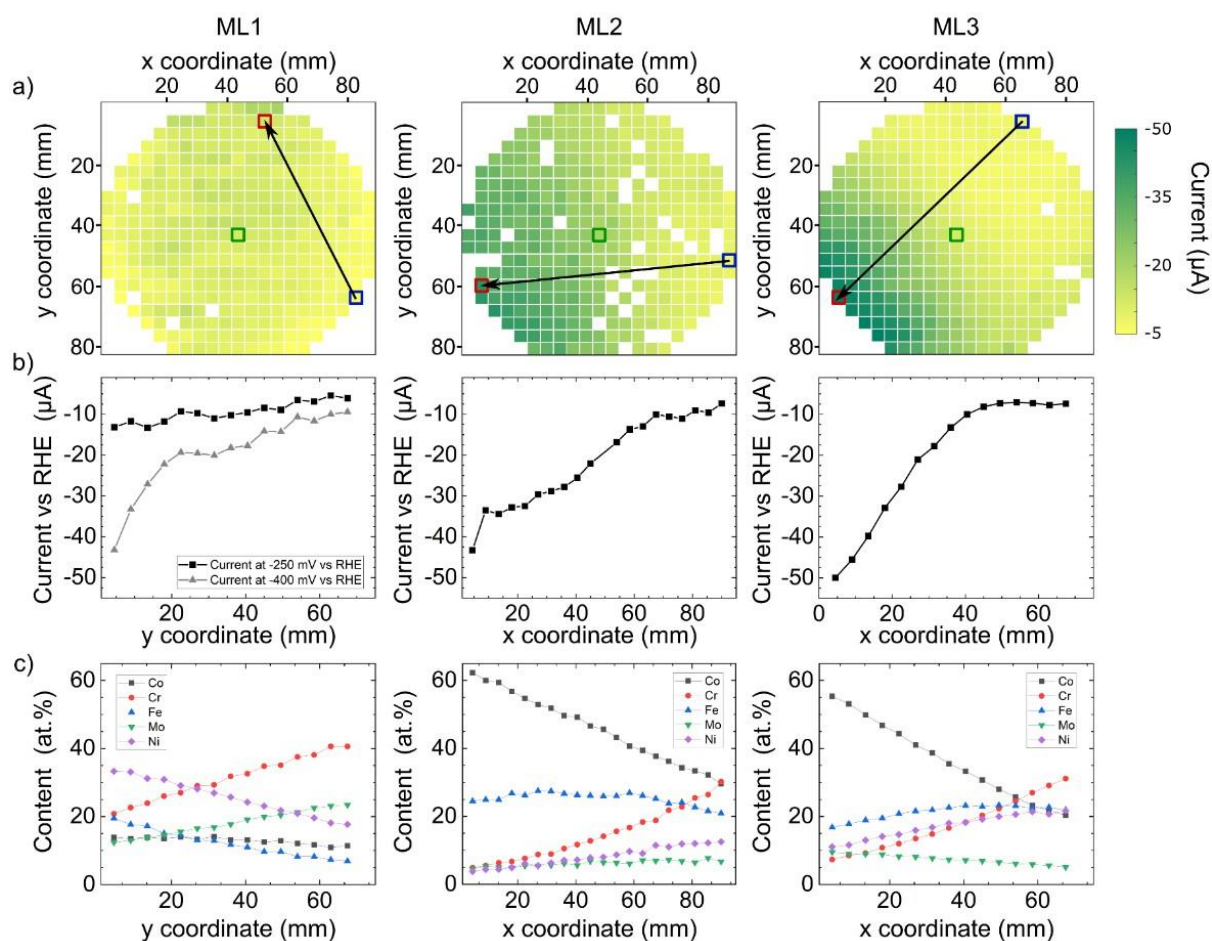


Figure 16: Comparison of ML1, ML2 and ML3: (a) color-coded activity map, visualizing the current in mA at 250 mV vs. RHE for all MAs in dependence of x- and y-coordinates; the black arrow represents a direct path from the lowest current (blue square) to the highest current (red square); center of the ML (green square); (b) current (mA) and (c) content of each element (at.%) in the MAs located on the black arrow with respect to the x- or y-coordinate.²⁰²

The comparison of the three MLs reveals that high contents of Cr (>20 at.%) have an inhibiting effect on the electrocatalytic HER activity. This finding explains the overall decreased activity observed in the Cr-rich ML1 in comparison to ML2 and ML3. Additionally, on ML2 and ML3, it is evident that the CCSS compositions with the highest Cr content exhibit decreased electrocatalytic HER activity. While Cr has been demonstrated to have a positive impact on stability,²⁰³ it does not contribute to enhanced HER activity in this context. Similar results have been reported for multimetal-based systems by McKay et al.²⁰⁴

However, despite the relatively high Cr content in ML1, it is observed that the HER activity can be enhanced by increasing the Fe and Ni content while decreasing the Cr and Mo content, while maintaining a constant Co content. In the case of ML2 and ML3, the MAs primarily consist of higher amounts of Co and Fe compared to other elements. Nevertheless, an increase in the relative Co content, accompanied by a decrease in

the amounts of Cr and Ni while maintaining a relatively constant amount of Fe and Mo, leads to an increase in HER activity. The Co-rich area of ML2 and ML3 exhibits the highest HER activity, with ML3-MA057 displaying the highest recorded current (50 mA at -250 mV vs. RHE). This value is approximately ten times higher than the areas with the lowest activities in this screening. These results indicate that a substantially high Co content (>40 at%) has a boosting effect on the HER activity.

The XRD patterns and LSV curves depicted in Figure 17 a) correspond to the selected MAs marked in Figure 16 a) using the same color code. The MAs with the highest HER activity (red) on the three MLs correspond to ML1-MA332, ML2-MA076, and ML3-MA057. The center MAs of each ML are indicated in green (ML1-MA168, ML2-MA168, ML3-MA167), while the compositions with the lowest activity (blue) correspond to ML1-MA075, ML2-MA136, and ML3-MA335.

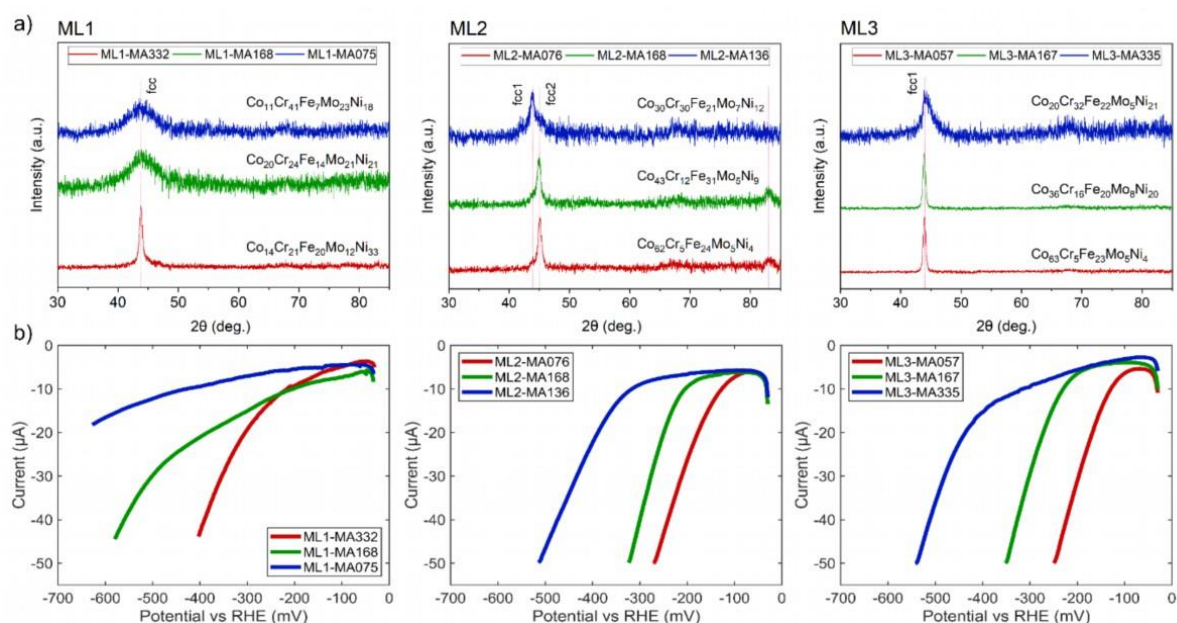


Figure 17: (a) XRD pattern of the MAs showing the highest (red) and the lowest current (blue) at -250 mV vs. RHE and the center MA (green) from each ML and (b) the corresponding recorded LSVs.²⁰²

The XRD patterns reveal diffraction intensity maxima, which can be attributed to one or two textured fcc solid solution phases (fcc1, fcc2) as shown in Figure 17 a). For ML1, the fcc intensity peaks appear at $2\theta = 45.00^\circ$ and $2\theta = 83.22^\circ$, for ML2, fcc1 is at $2\theta = 43.84^\circ$, and for ML3, fcc1 appears at $2\theta = 43.79^\circ$. The results suggest that both crystallinity and composition have a complex influence on the catalytic activity. Generally, lower crystallinity (broad diffraction peaks with low intensity) is associated with poorer electrochemical activity, while higher crystallinity (sharp diffraction peaks with high intensity) indicates better activity in the respective ML. However, the

composition has a more significant effect, as observed in ML3. ML3-MA167 (Co₃₆Cr₁₆Fe₂₀Mo₈Ni₂₀) exhibits higher crystallinity compared to the MAs in the low-activity region of ML3, but it does not possess the highest activity within the investigated composition range. The highest activity is observed for Co₅₆Cr₈Fe₁₉Mo₇Ni₁₀ at -250 mV vs RHE (ML3-MA057), which exhibits comparable crystallinity in the XRD measurements. This suggests that the composition plays a more significant role in determining activity than crystallinity, although there may be complex interactions between these properties.

Including ML3-MA057, a total of 349 compositions were discovered on ML2 and ML3 that exhibit similar or higher catalytic activity than the composition reported by Zhang et al. (ML3-MA167). These results are illustrated in Fig. 5, where the corresponding compositions for the MAs with higher activity are highlighted in yellow on the two MLs. A dashed black line in Fig. 5 represents the currents recorded at 250 mV vs. RHE for comparison. Overall, the discovery of more than 300 active compositions demonstrates the advantage of high-throughput techniques over conventional methods that examine one composition at a time.

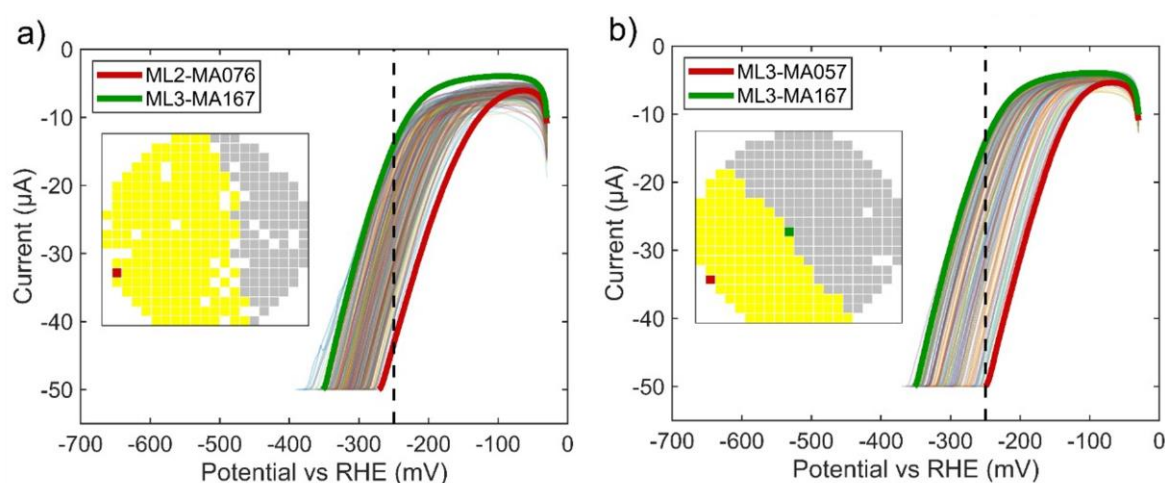


Figure 18: LSVs of 349 MAs from (a) ML2 and (b) ML3. The LSVs are compared to the corresponding CCSS composition found by Zhang et al.⁵⁵ (ML3-MA167, green). MAs with similar or better electrocatalytic activity are marked yellow in the activity maps which were plotted at -250 mV vs. RHE (insert). The most active MAs of ML2 (ML2-MA076) and ML3 (ML3-MA057) are marked in red.²⁰²

The Tafel slopes for all MAs were calculated and plotted on the MLs to provide spatial resolution (Figure 19) using a color code. The coefficient of determination (R^2) was also calculated for all MAs to assess the quality of the linear fit. Tafel slopes in the range of 50 to 130 mV dec⁻¹ were obtained for the MAs located on ML2 and ML3. These values are within the expected range of 40 mV dec⁻¹ to 120 mV dec⁻¹ for the

Heyrovsky and Volmer steps, respectively, which are considered rate-determining steps. By analyzing the catalyst composition, trends can be identified regarding the dominant limiting steps. Specifically, the Tafel slope values differ between the area with higher Cr content and lower HER activity, and the area with low Cr content and higher activity on ML2 and ML3. Compositions exhibiting lower activity and higher Tafel slope values indicate that the rate-determining step is the transfer of the first proton and electron, corresponding to the Volmer step. In contrast, compositions with relatively lower HER electrocatalytic activities exhibit hindered second proton and electron transfer in the Heyrovsky step. On ML1, where the MAs with the lowest catalytic activities were observed, Tafel slopes above 150 mV dec^{-1} were calculated. Such values, which deviate from the typical Volmer and Heyrovsky steps in HER, have been reported in the literature for catalyst materials with poor conductivity, as demonstrated by Chung et al.²⁰⁵ However, it is important to consider these values carefully as they do not provide relevant intrinsic values.

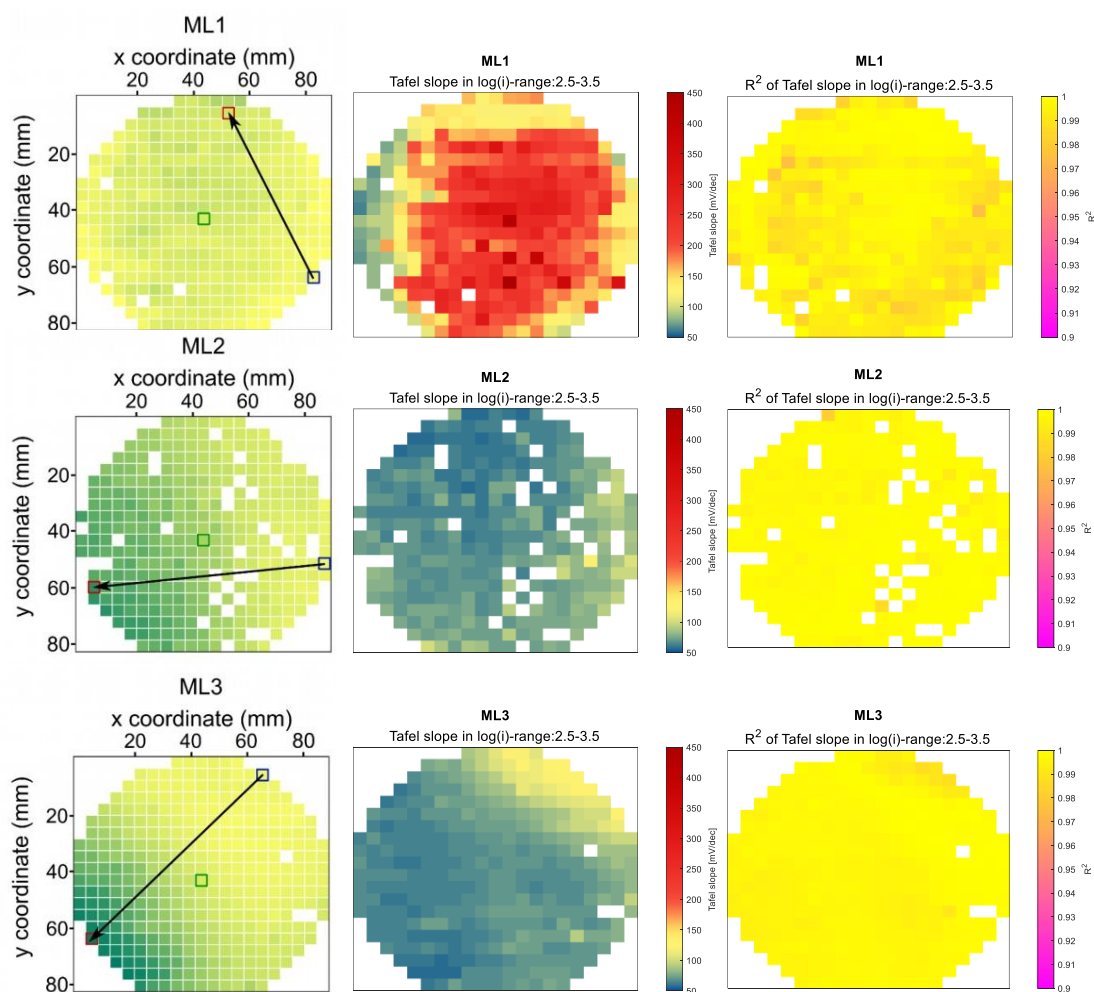


Figure 19: Comparison of the colormaps of the current at -250 mV vs RHE , the Tafel slope in $\log(i)$ -range 2.5 – 3.5 and the R^2 -values of the linear fitting of the corresponding Tafel slopes.²⁰²

To highlight the different Tafel slopes of the MAs, they were further presented for the MAs discussed in Fig. 4. Fig. S2† shows that the MAs with the lowest electrocatalytic HER activity on ML1 exhibit extremely high Tafel slope values, indicating high resistance of the sample. The corresponding LSVs presented in Fig. 4 for ML1 show an almost linear increase at lower overpotential, suggesting high resistance of the MAs. On ML2 and ML3, the Tafel slope values range from 65 to 80, indicating the highest electrocatalytic activity. This may suggest a combination of the two possible limiting steps (Volmer and Heyrovsky steps) and a potential variation in coverage of the multiple active sites, which are expected to be present in a HEA material, contributing to these results.

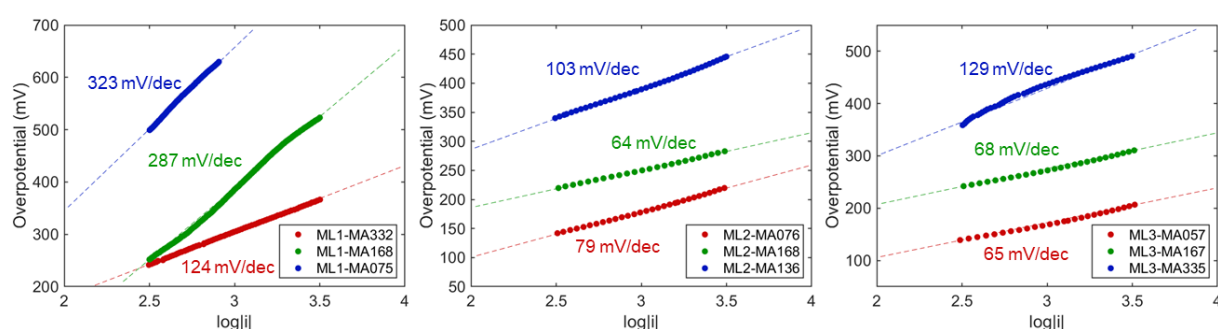


Figure 20: Tafel-plots from the LSVs with the highest (red) and the lowest current (blue) at -250 mV vs RHE and the center MA (green) from each ML.²⁰²

In this study, more than 1000 compositions of the Co–Cr–Fe–Mo–Ni system were evaluated using high-throughput screening of thin film material libraries (MLs). Among these compositions, 349 were found to exhibit similar or better HER activity compared to a recently reported catalyst composition for the system. Through the evaluation of three different MLs, trends in HER activity were identified and correlated with crystallinity and chemical composition. It was observed that high contents of Fe and Co in the CCSS contribute to enhanced HER activity, while an increasing amount of Cr has the opposite effect. Moreover, it was found that Co–Cr–Fe–Mo–Ni CCSS compositions with higher HER activity tend to exhibit higher crystallinity. However, the composition of the CCSS was found to have a stronger influence on the HER electrocatalytic activity compared to crystallinity. Overall, there is a complex interaction between compositions and phases that affects the activity of HER in this system.

4.2 SECCM investigations on thin-film molybdenum disulfide

As previously reported in chapter 2, initial findings on MoS₂ were conducted by other research groups using SECCM. These studies consistently utilized exfoliation techniques or chemical vapor deposition (CVD) to create thin films, resulting in small flakes ranging from nm to a few μm in size. However, the current focus of this PhD study is on the investigation of larger MoS₂ thin film flakes grown through CVD and subsequently transferred onto a conductive substrate. The materials were fabricated by the group of Prof. Dr. Marika Schleberger and were characterized as received. Furthermore, this chapter also presents technical enhancements made to the SECCM setup used in previous studies, leading to results that have been published in a peer-reviewed journal.

4.2.1 Initial setup measurements

In first initial experiments the setup was in a state described by T. Tarnev in his PhD thesis¹⁵⁸ and in several research articles.^{159,173} This setup was utilized in those studies to analyze the catalytic activity of ensembles of particles within the spot size of a single SECCM measurement. To achieve this, a probe size of approximately 1 μm was deemed sufficient, resulting in lower demands for the required signal-to-noise ratio compared to using smaller tip sizes for higher-resolution experimental data.

For this study, MoS₂ thin layer flakes were synthesized via a Chemical Vapor Deposition (CVD) process. These flakes were subsequently transferred from the synthesis substrate (Si/SiO₂) to a conductive glassy carbon (GC) substrate, allowing for the creation of a suitable working electrode for electrochemical measurements. The synthesis and transfer process are described in more detail in chapter 6. Following the transfer, SECCM scans were performed on the MoS₂ sample using double barrel capillaries. Detailed information regarding the SECCM experiments with double barrel capillaries can be found in chapter 6. After the SECCM scan, the scanned area was carefully examined using scanning electron microscopy (SEM) to observe and analyze the residual electrolyte footprints left by the SECCM tip approaches. Figure 21 presents the results obtained from the conducted SECCM scan. In Figure 21 a), the SEM image showcases the scanned area, revealing the triangular-shaped MoS₂ flake along with the residuals of the SECCM scan's electrolyte. The SECCM scan pattern is characterized by a division into lines and points, as indicated in Figure 21 a). It is

evident from the image that the residuals of the scan gradually increase starting from line 4, denoted by a green frame. Beyond this point, the capillary experienced an accidental collision with the substrate, leading to larger residuals in subsequent spots. For comparative analysis, the third line is selected, as it represents measurements before the capillary crash, encompassing spots on both the glassy carbon substrate and the transferred MoS₂. Following the landing of the SECCM tip, CV measurements were conducted in the potential range between 0 V and -1.0 V vs RHE. The corresponding polarization curves are depicted in Figure 21 b) for Spots 1-6 in line 3 (highlighted with a yellow frame in Figure 21 a) and in Figure 21 c) for Spots 7-11 in line 3 (highlighted with a red frame in Figure 21 a). As observed in the SEM image, Spots 9-11 are situated on a single MoS₂ flake, while all other spots lie on the glassy carbon substrate. This spatial distinction is also evident in the CVs of these spots. Specifically, the current responses for the landing spots on glassy carbon reach a maximum of approximately -150 pA at -1.0 V vs RHE. Conversely, the spots on the MoS₂ exhibit higher activity for the HER, with current responses ranging from -200 pA to -250 pA at the same potentials.

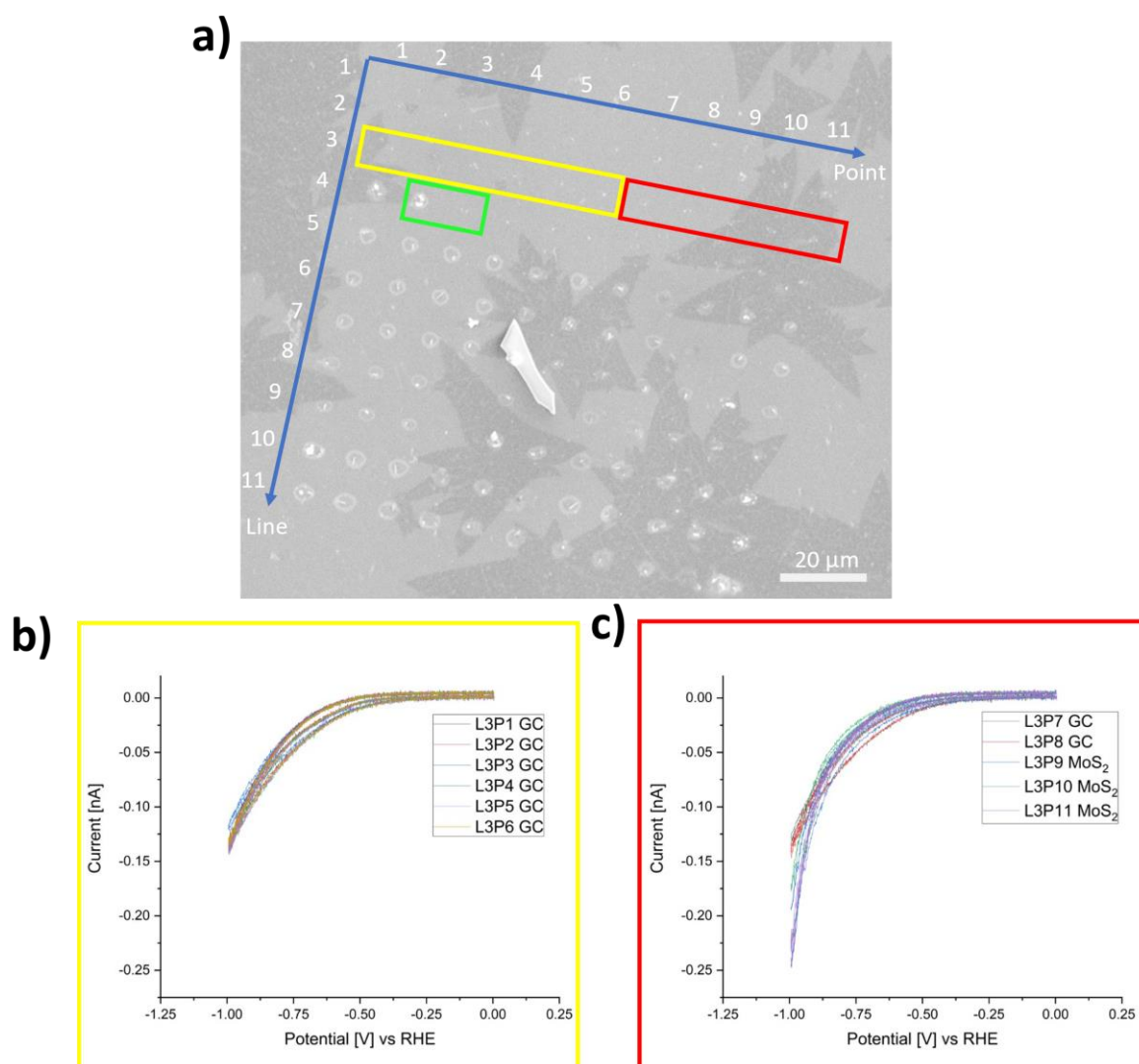


Figure 21: SECCM scan on MoS₂ transferred on GC, a) SEM image of scan, b) and c) polarization curves of measurements.

While the discrimination of activity between the transferred MoS₂ flake and the underlying glassy carbon substrate marks an initial achievement, it does not constitute novel advancements in the realm of SECCM on MoS₂. To gain more profound insights into the electrochemical properties, further higher-resolution mappings are imperative, surpassing the simple differentiation between being on the MoS₂ or not. The resolution in a SECCM scan is determined by two key factors: the hopping distance between different SECCM spots and the size of the probe utilized.

In the utilized setup, the conventional capillary tip size typically falls within the range of approximately 500 nm to 1000 nm in diameter. However, to effectively visualize and dissolve active sites on the MoS₂ flakes, the possibility of using smaller SECCM capillary tip sizes becomes crucial. To achieve this, transitioning from double-barrel to

single-barrel capillaries was the initial step in enhancing the setup's resolution. As the reduction of tip size is more feasible with single-barrel capillaries, and the approach follows a more straightforward principle, this switch was deemed essential. Further details of the experimental modifications are elucidated in Chapter 6. Initial attempts of SECCM measurements were carried out using single-barrel capillaries with tip sizes less than 100 nm.

The primary challenge in this SECCM configuration was the inadequate signal-to-noise ratio for currents occurring after approaching with a tip smaller than 100 nm. Figure 22 a) depicts the current signal before the SECCM meniscus contacts the working electrode, displaying a peak-to-peak noise of approximately 17 pA. However, upon the approach towards the surface, the process is interrupted as the capillary tip crashes into the surface, enlarging the tip opening and enabling a larger approach current to emerge. A failed scan with a capillary crashed into the surface is illustrated in Figure 22 b). In this case, electrolyte from the capillary leaks onto the surface, overlapping with other spot sites, rendering the mapping of electrocatalytic activity unfeasible.

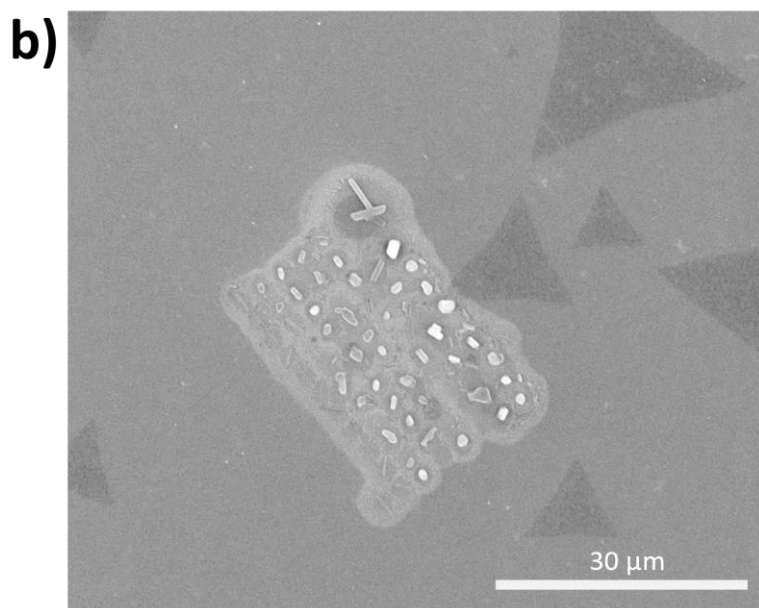
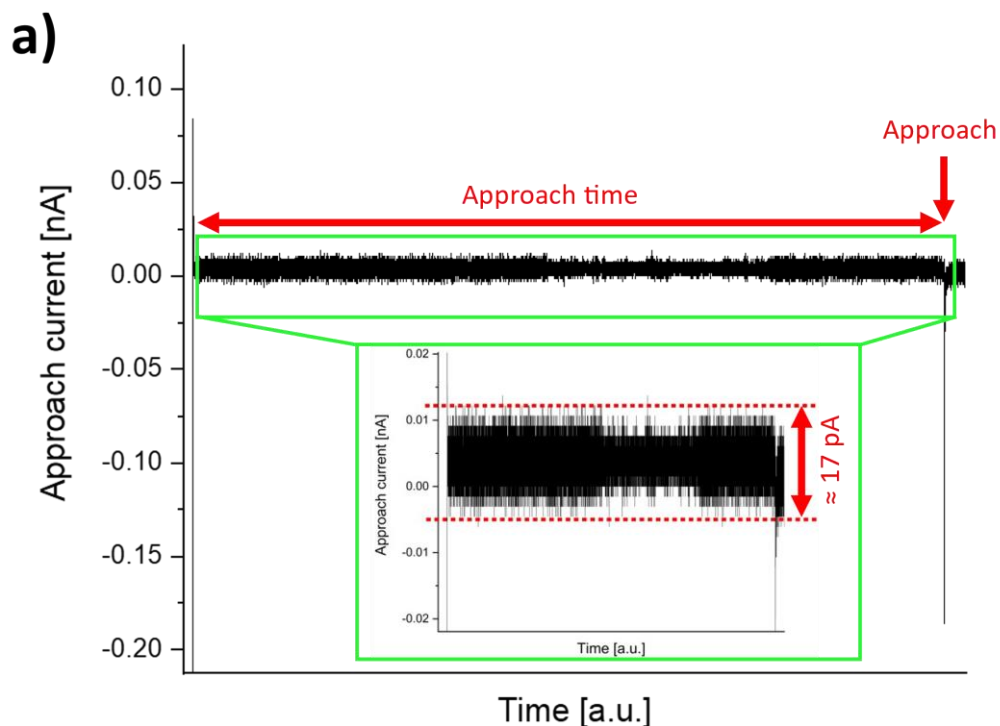


Figure 22: a) Current signal during the approach of a SECCM capillary tip, b) electrolyte and glass residuals of a failed SECCM scan.

4.2.2 Noise reduction

The SECCM is aiming to detect current responses from extremely small electrode areas to resolve high resolution activity maps. This means the detection of very small currents with an optimized signal-to-noise ratio is desirable for a meaningful result. Optimization is done in this case by reducing the noise in the current signal as much as possible. Electrical noise in general, as defined by Motchenbacher (1993), is “*any unwanted disturbance that obscures or interferes with a desired signal.*”²⁰⁶ In this work

the desired signal is an electrical current resulting after an electrochemical reaction which in the case of the SECCM can vary in between nA- to fA-range depending on the probe size.

Electrical noise refers to random fluctuations in currents and voltages that occur in electronic systems. These fluctuations arise from various sources, including the thermal motion of electrons and the quantized nature of electric charge. As a result, noise is an inherent characteristic of electronic circuits and can be observed in any electrical system.²⁰⁷

For optimizing the signal-to-noise ratio of a current amplifier, which is used to convert the current signal from an electrochemical reaction to a voltage signal, the parameter of interest is the transimpedance. This device amplifies the magnitude of the input current by a fixed multiple and passes it to the succeeding circuit or device, thus performing current amplification. To achieve a high sensitivity of the amplifier, the bandwidth and rise time are crucial factors. The bandwidth should be small enough to avoid capturing high or low-frequency noise sources, while the rise time should be appropriate to capture the speed of the electrochemical reactions, allowing them to be displayed accurately by the device.

Initially, the ELC-03XS from NPI,²⁰⁸ a typical patch clamp amplifier, was used to record the current between the QRCE and the WE. However, due to its high complexity, this setup configuration resulted in unacceptable noise rates (Figure 22). To overcome this issue, a simpler setup was implemented, replacing the ELC-03XS with a variable gain low noise transimpedance current amplifier with high bandwidth from FEMTO, known as the DLPCA-200.²⁰⁹ This amplifier has a transimpedance gain ranging from 10^3 to 10^{11} V/A, with input noise as low as $4.3 \text{ fA}/\sqrt{\text{Hz}}$ and a bandwidth up to 500 kHz. The rise time has a minimum value of 700 ns. With the implementation of the DLPCA-200 amplifier, the need for a separate preamplifier was eliminated, reducing the number of electrical nodes. The QRCE is now directly connected to the input of the amplifier using a short shielded pickup cable, minimizing the possibility of capturing additional noise from the environment before being led into the current amplifier.

Through the implementation of the new setup configuration with a capillary size smaller than 100 nm, a substantial reduction in the signal to noise ratio was successfully achieved. The presented Figure 22 illustrates an exemplary LSV measurement utilizing

this improved setup, while maintaining a similar sample configuration as in Figure 21. The temporal evolution of the current signal during the approach, waiting time, LSV measurement, and retraction stages is displayed. Remarkably, the noise level has been significantly decreased to approximately 1.1 pA. Comparatively, in Figure 21, the majority of current features, such as the approach current and the LSV signal, would have been indistinguishable from the noise observed in the previous setup configuration.

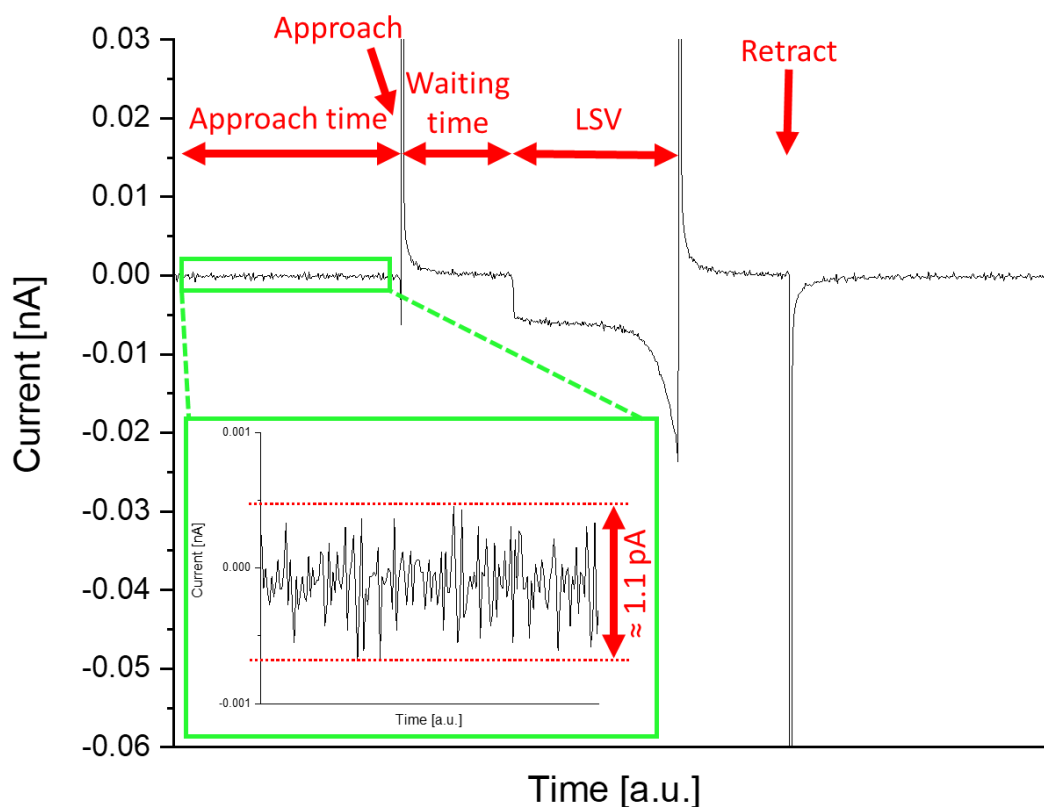


Figure 23: Exemplary current response of a SECCM experiment including approach, waiting time, LSV experiment and retraction after the system optimization. The experiment was performed using a capillary size of approximately 100 nm, Ag/AgCl wire as QRCE and 0.1 M HClO₄ as electrolyte. The scan rate of the LSV was 2 V/s. The approach and retraction were performed as described in chapter 6.5.3.

The enhanced setup configuration now allows for the realization of more ambitious high-resolution scans, enabling a deeper investigation of electrochemical properties with increased precision and accuracy.

4.2.3 Revealing the heterogeneity of large-area MoS₂ layers in the electrocatalytic hydrogen evolution reaction

The following subchapter covers the studies of Schumacher et al.²¹⁰ Parts of the text or paraphrases were taken from ²¹⁰. The contribution in this study is divided as follows. SECCM measurements were performed, and electrochemical data was analyzed and

interpreted by Simon Schumacher (S.S). Fabrication and transfer of the MoS₂ sheets were performed by Lukas Madauß. SEM measurements after the SECCM scan were performed by S.S. Writing of the original manuscript draft was done by S.S. and Corina Andronescu (C.A.). Further data interpretation was done by S.S. and Yossarian Liebsch. Conceptualization, providing resources, supervision and project administration are attributed to Marika Schleberger and C.A. Review and editing of the manuscript were done by all coauthors.

In this study, the surface of large areas of single-sheet MoS₂ that were grown by chemical vapor deposition (CVD) was evaluated. These MoS₂ sheets were transferred onto a glassy carbon (GC) electrode using a polymer-assisted method.²¹¹ A total of 4941 different spots within a 30 µm x 40 µm area were probed, with approximately 4400 spots located on the MoS₂ sheet. During the investigation, we observed variations in the electrocatalytic activity for the HER across the surface of the MoS₂ sheet. The increased lateral heterogeneity in HER activity was observed.

A GC electrode was used to establish the electrical connection (in the so-called bottom-contacted mode) and was further used as a working electrode (WE) in SECCM experiments. The mode of contacting the MoS₂ layers was shown to impact the measured electrocatalytic activity of MoS₂ by SECCM, since different pathways for the electrons transport are established.^{104,212} In top contact, the lateral electron transport along the layer occurs, while in bottom contact, the electron transfer occurs from the substrate to the upper MoS₂ sheet, where the reaction takes place. For example, in the case of bulk MoS₂, measuring with a top contact proved to be beneficial as compared to measuring with a bottom contact, as it prevented the recording LSVs with artefacts.¹⁰⁴ On the other hand, for single to few-layer MoS₂, the bottom contact was successfully used to perform SECCM.²¹² For the large single-sheet MoS₂ used in this study, the recorded LSVs during the SECCM measurement show no artefacts (Figure S1), indicating that electrical conductivity between the MoS₂ sheet and the GC current collector is not limited.

A GC electrode was utilized to establish the electrical connection (in the so-called bottom-contacted mode) and was further used as a working electrode (WE) in SECCM experiments. The mode of contacting the MoS₂ layers was shown to impact the measured electrocatalytic activity of MoS₂ by SECCM, since different pathways for

electron transport are established.^{104,212} In the top contact mode, the lateral electron transport along the layer occurs, while in the bottom contact mode, the electron transfer occurs from the substrate to the upper MoS₂ sheet, where the reaction takes place.^{104,212} For example, in the case of bulk MoS₂, measuring with a top contact proved to be beneficial as compared to measuring with a bottom contact, as it prevented the recording of LSVs with artifacts.^{104,212} On the other hand, for single to few-layer MoS₂, the bottom contact was successfully used to perform SECCM.²¹² SECCM measurements were performed with a capillary size of 55 nm in a hopping mode with a hopping step of 500 nm (Figure 24).

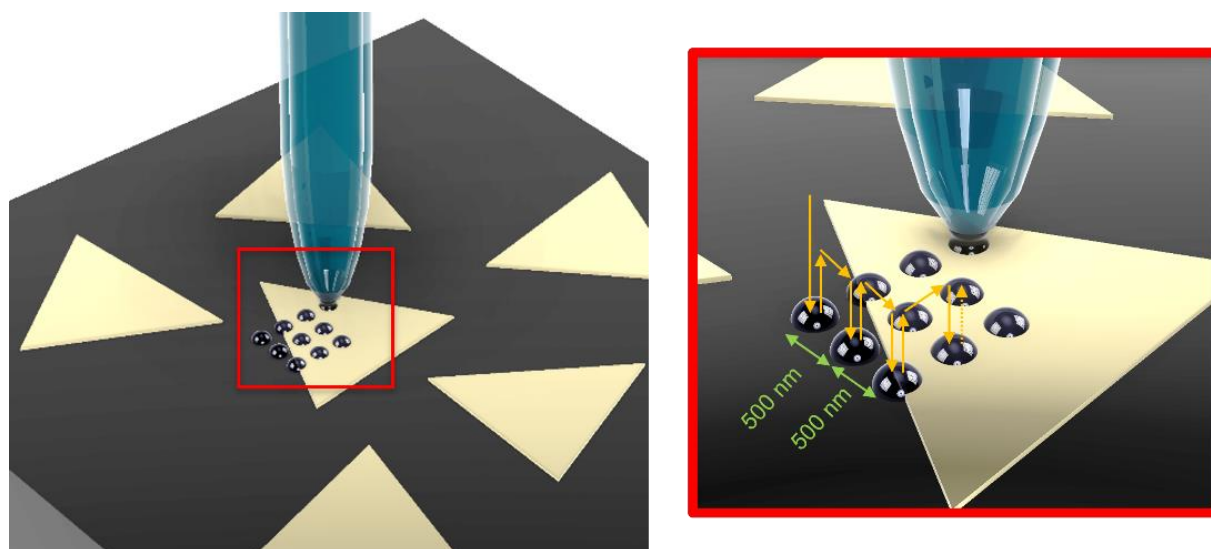


Figure 24: Schematic illustration of the SECCM hopping mode with a hopping distance of 500 nm.

For the large single-sheet MoS₂ used in this study, the recorded LSVs during the SECCM measurement show no artifacts (Figure 25), indicating that electrical conductivity between the MoS₂ sheet and the GC current collector is not limited.

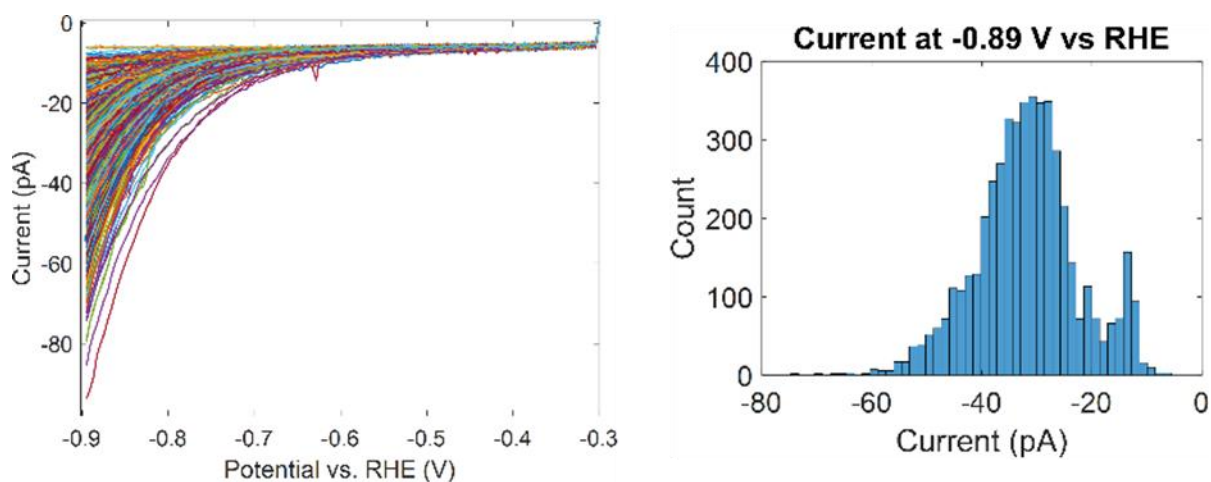


Figure 25: Linear sweep voltammograms recorded in the SECCM experiment presented in Figure 2 in 0.1 M HClO₄ using a scan rate of 2V/s and a SECCM nano-pipette having an opening of ~ 55 nm (left). The currents recorded at a potential of -0.89 V vs RHE are plotted in a histogram (right)

Based on the recorded LSVs, current maps are derived by plotting the currents recorded at defined potentials. At lower overpotential (-0.6 V vs RHE, Figure 26 b), slightly higher currents are recorded on the GC compared with the MoS₂ sheet. However, at overpotentials lower than -0.6 V vs RHE, a sudden increase in the currents recorded on the MoS₂ sheet compared to the GC is observed (Figure 26 b).

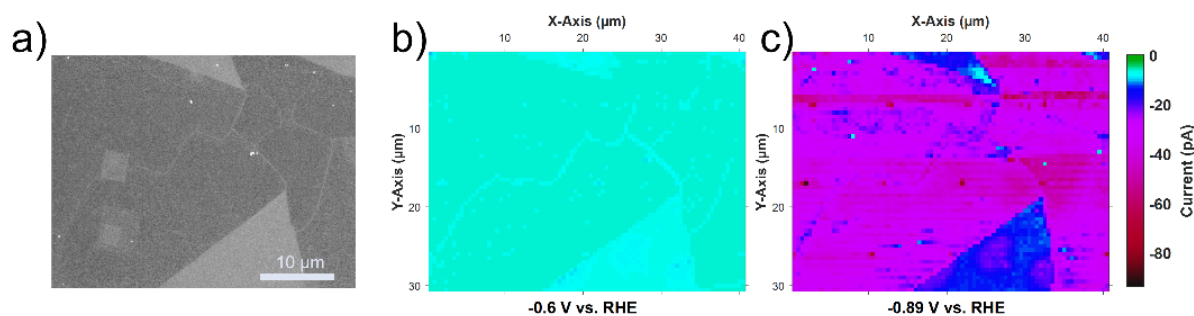


Figure 26: a) SEM image of the MoS₂ sheet transferred on the GC on which the SECCM scan; Corresponding currents maps of the area marked in a) derived by plotting the currents extracted from the recorded LSVs as a function of the measured position at b) -0.6 V and c) -0.89 V vs RHE respectively.

Overall, over the MoS₂ sheet, a high variation of currents at -0.89 V vs RHE is seen, ranging from -20 to -60 pA (Figure 25, histogram), corresponding to current densities ranging from -0.45 to -1.36 A/cm² (Figure 27), in agreement with the results of Bentley et al.¹⁰⁴

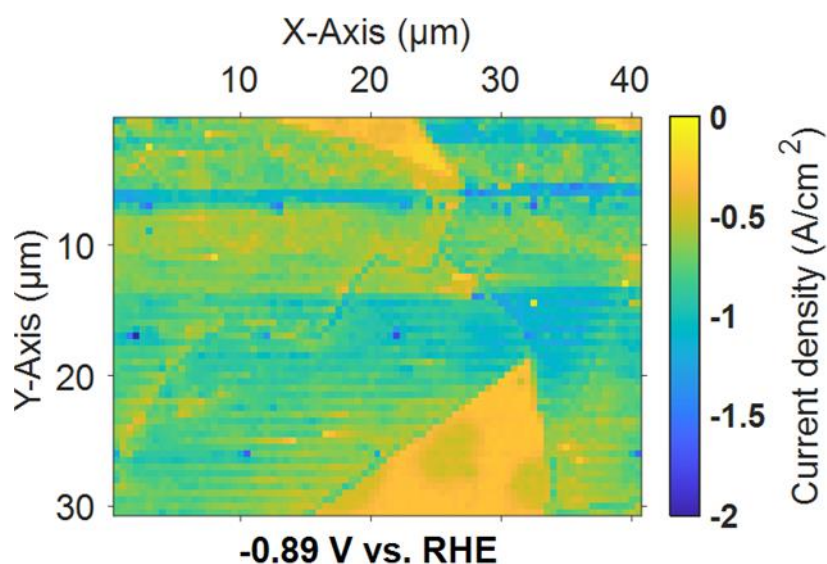


Figure 27: Current densities derived map at -0.89 V vs. RHE assuming the size of the electrochemical cell having the diameter of the nanopipette (55 nm).

Exemplary LSVs from different locations are illustrated in Figure 28 c). To confirm the technical robustness of our experiment, we compared the currents recorded on the GC at the beginning of the scan with those at the end of the scan (white and black areas marked in Figure 28 b). The histogram (Figure 28 d) shows that on GC, currents ranging between -7 and -24 pA are recorded, with an average of -15 ± 3 pA. Thus, we can confirm that no technical error occurred during the SECCM scan performed over 4941 landing sites, and the high current variation is caused by the MoS₂ structure only. Over the scan, lateral streaking can be observed over the scan direction, indicating changes in the droplet size. Such changes can be caused by differences in the surface's hydrophobicity/hydrophilicity due to residual polymers/water layers remaining on the MoS₂ after its transfer.

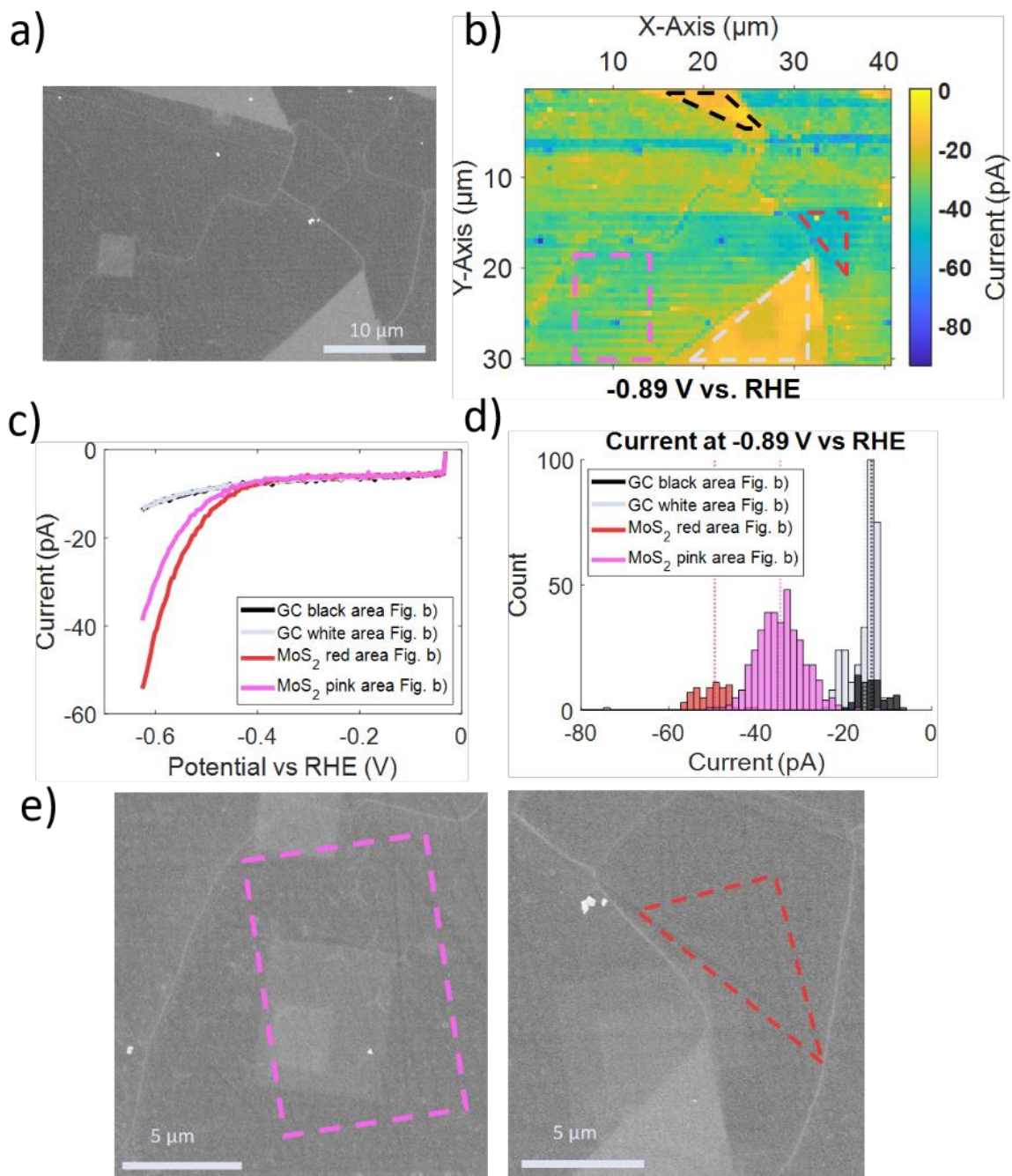


Figure 28: a) SEM image of the MoS₂ sheet transferred on the GC on which the SECCM scan, containing 61 x 81 measured points, was performed. The SECCM scan spreads over an area of 40 μm x 30 μm with a hopping distance of 500 nm and a nanopipette tip size of ~ 55 nm. b) Corresponding currents maps of the area marked in Figure a) derived by plotting the currents extracted from the recorded LSVs as a function of the measured position at -0.89 V vs RHE. c) Exemplary LSVs from different regions of the scan (GC top: X = 19.5 μm, Y = 1 μm; GC bottom: X = 29.5 μm, Y = 24 μm; MoS₂ high activity: X = 34 μm, Y = 15.5 μm; MoS₂ lower activity: X = 9.5 μm, Y = 23.5 μm). d) Histograms showing the number of measured points for which different currents are recorded at -0.89 V vs RHE in the areas marked with pink and red. The currents marked with white and black bars are currents recorded on the GC electrode. e) SEM images of the areas marked with pink in which the presence of multiple MoS₂ layers (highlighted in Figure 3a) can be observed and SEM image of the area marked with red where no multi-layer MoS₂ can be identified.

For instance, in the region marked with pink in Figure 2b), the recorded currents at -0.89 V vs RHE range between -20 to -40 pA, while in the red marked area higher

currents between -40 to -60 pA are recorded. While the MoS₂ sheet shows relatively homogeneous catalytic activity locally in an area of a few 1-2 μm², significant differences are observed over extended ranges, as seen in Figure 28.

SEM analysis of the transferred MoS₂ layers revealed the presence of additional triangular-shaped MoS₂ layers with ~1 μm length on the MoS₂ single layers (Figure 28 e) and Figure 29 a).

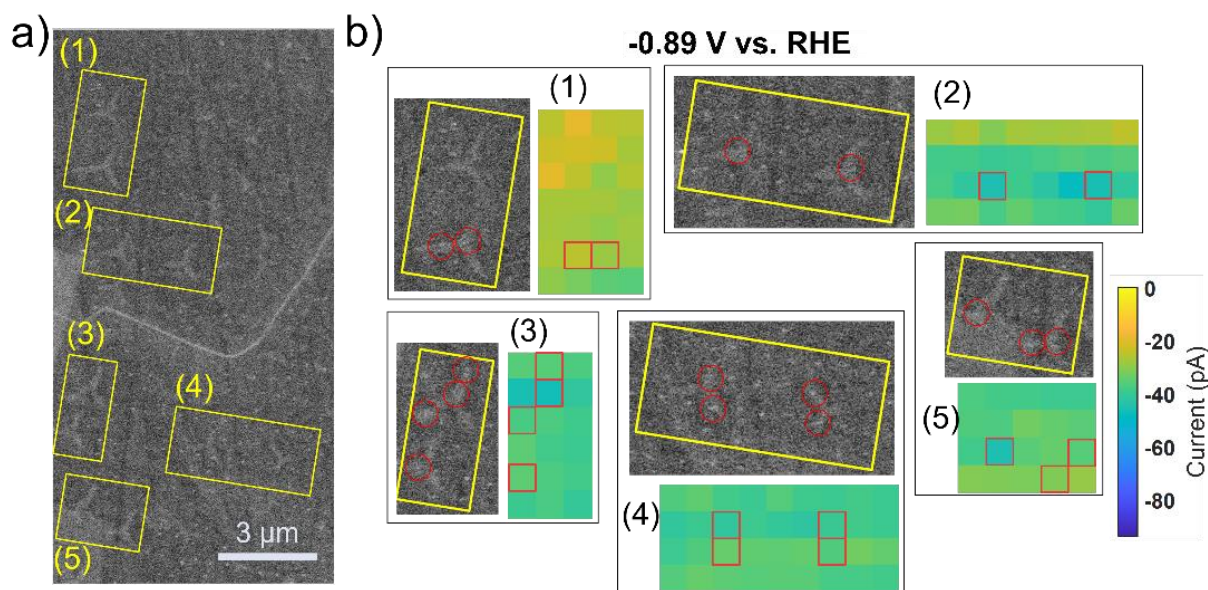


Figure 29: a) SEM image of the MoS₂ sheet transferred on the GC after performing the SECCM experiment on which one can observe the areas in contact with the electrolyte droplet as well as the additional MoS₂ layers present on the large-area MoS₂, which are marked for a better identification; b) the SEM areas and the corresponding activity maps derived by plotting the currents recorded at -0.89 V vs RHE as a function of the measured pixel for the marked regions in which single or multilayered MoS₂ are evaluated in the SECCM experiment.

During the SECCM scan, several landings occurred on top of the multilayer MoS₂ regions, leading to LSVs recorded on a single or multiple MoS₂ layers. The footprint of the SECCM landing spot on the multilayered MoS₂ is marked by a red circle in the SEM image, and the corresponding current with a red square in the resulting SECCM color map in Figure 29 b). Comparing the recorded currents at the same potential, we do not observe significant differences between the single-layer or the multilayer MoS₂ activities. This indicates that the recorded catalytic activity on the transferred large-area MoS₂ is strongly influenced by the electron transfer between the GC electrode and the first MoS₂ sheet. This finding is consistent with results reported by Takahashi

et al. on small-sized MoS₂, where no difference was noticeable in the HER electrocatalytic activity or the Tafel slope for single, two, or three layers of MoS₂.¹⁰²

Based on the analysis of the areas containing single or multilayered MoS₂, we can conclude that the observed heterogeneity in catalytic activity in Figure 28 is not due to the presence of MoS₂ multilayers. Polymer residues may still be present on top of the sample, equally affecting single and multilayers. Another possible factor is the existence of a water layer/gas bubbles between the transferred MoS₂ and the GC surface, as previously reported. These intercalated water layers are commonly found in 2D samples exposed to ambient conditions and can affect the electronic properties.

Tafel analysis can provide information regarding the reaction mechanism and was extensively used to identify the rate-limiting step in electrocatalytic-driven processes. The Tafel slopes were automatically derived in the log(i)-range 2.5 to 3.5 and plotted similar to the activity maps (Figure 30 a). To ensure a good quality of the data fitting used to derive the Tafel plots, the value of the coefficient of determination (R^2) was checked and points with R^2 values outside the range of 0.9 to 1 were removed (white points in Figures 30 a, 30 b).

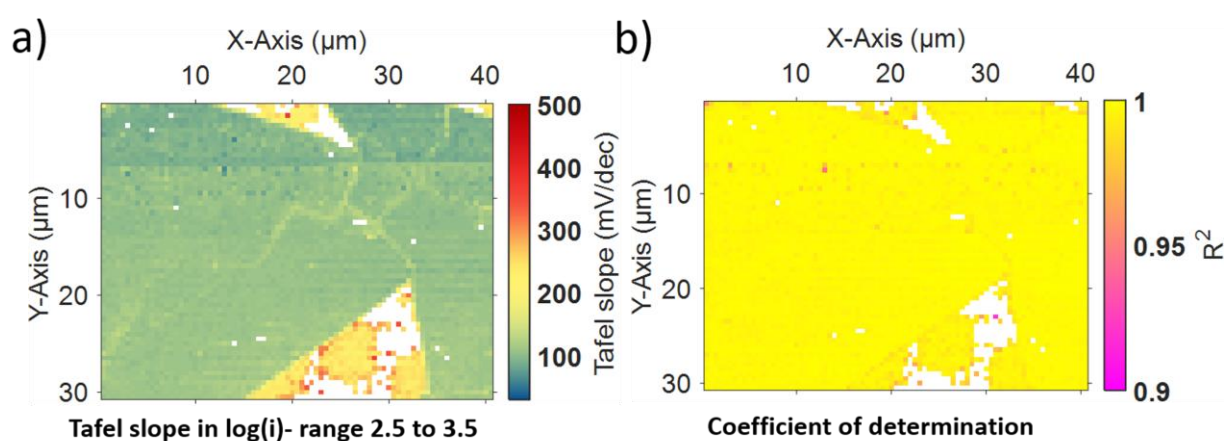


Figure 30: Tafel plot analysis of the SECCM scan presented in Figures 25 and 28 a) Tafel slopes and b) their corresponding coefficient of determination (R^2) as a function of the position in the SECCM scan.

The distribution of calculated Tafel slopes over the SECCM scan is depicted in Figure 31, showing Tafel slopes with values ranging between 80 to 120 mV/dec for the majority of measured points. These values suggest that the Volmer step or the Heyrovsky step at high coverage rates are the rate-determining steps. However, a limited number of points, mainly located on the GC surface, exhibited higher Tafel slopes than theoretically expected. Overall, the recorded Tafel plots support the HER

activity of the basal planes, which is consistent with previous reports showing that the basal planes of pristine MoS₂ are not highly electrocatalytically active but similar to those of Au and Cu.¹⁰⁴

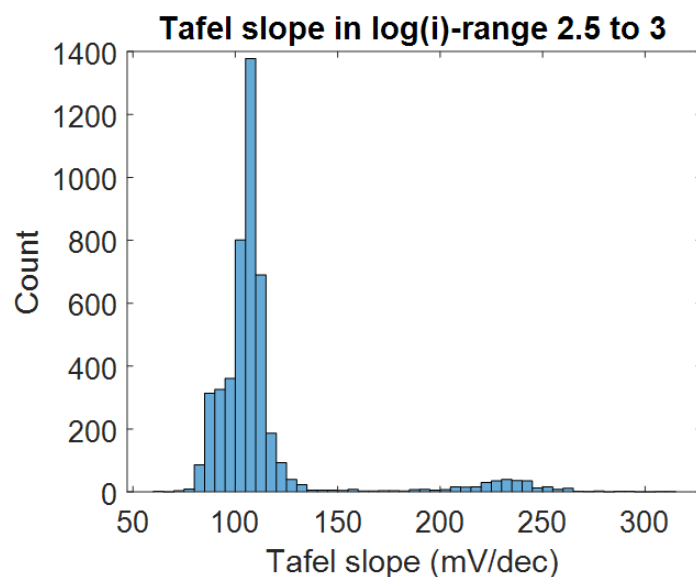


Figure 31: Histogram representing the Tafel slopes calculated in the $\log(i) = 2.5 - 3$ range based on the LSVs recorded (Figure 25) in the SECCM scan analyzed in Figure 28

In conclusion, the SECCM analysis of large single layers of MoS₂ grown by CVD and transferred to a GC electrode revealed high lateral heterogeneity, which becomes significant over longer ranges. The lack of difference in activity between single and multilayer MoS₂ suggests that the observed lateral heterogeneity is likely due to the presence of polymer residues or the existence of a water layer/gas bubbles between the MoS₂ sheet and the GC formed during the transfer process. The recorded Tafel slopes and current densities indicate a moderate HER activity of the large-area MoS₂ transferred onto the GC, similar to that of exfoliated MoS₂ layers reported in the literature.

4.3 Design, Construction and Evaluation of SECCM configuration for strain induced optimization of the electrocatalytic activity for HER

The following chapter covers the studies that were addressed within the scope of the DFG project “Exploring high-entropy alloys for the hydrogen evolution reaction in alkaline electrocatalysis: from compositional screening to strain effects - AN 1570/2-1” from the research groups of Prof. Dr. Corina Andronescu and Prof. Dr. Alfred Ludwig. The contribution in this study is divided as follows. SECCM measurements were performed, and electrochemical data was analyzed by Simon Schumacher (S.S). Design and construction of the stress chip holder as well as implementation in the SECCM setup was done by S.S. Armin Lindner from the fine mechanics workshop of the RUB provided support for the visualization and construction of the stress chip holder. Fabrication, coating and characterization of the stress chip samples were performed by Sabrina Baha (S.B.). Conceptualization, providing resources, supervision and project administration are attributed to Alfred Ludwig and Corina Andronescu.

4.3.1 Idea of the project

For better understanding, the following subchapter presents the idea of the project “Exploring high-entropy alloys for the hydrogen evolution reaction in alkaline electrocatalysis: from compositional screening to strain effects - AN 1570/2-1”. This was drafted by Prof. Dr. Corina Andronescu and Prof. Dr. Alfred Ludwig. The following subchapter 4.3.1 represents a rephrasing of parts of the project proposal.

The project involves investigating the influence of stress on the catalytic activity of a metallic catalyst layer for the HER. For this purpose, a stress chip²¹³ fabricated from silicon was used as the supporting substrate for a sputtered thin film of a metallic catalyst, Pt in this case, serving as the model catalyst for the HER. Initially designed for measuring intrinsic stress in sputtered thin films, the stress chips were modified to function as tools for applying external stress to the thin films on the chip. These stress chips, integrated into the SECCM setup along with a cantilever bending system, allowed the analysis of the catalytic activity for the HER under various induced external stress states on the stress chip using the SECCM technique.

Thin films will be fabricated and deposited onto stress chips to induce changes in their stress levels during electrochemical measurements. The stress manipulation will be

achieved by applying a load at the free end of the cantilever, resulting in deflection and strain on the surface. The catalytic behavior will be characterized at the fixed end of the cantilever, where the strain on the surface is most pronounced. By employing the design of the stress chip and bending the cantilever, surface strains of up to approximately 1% can be attained. The surface strain ε_s is determined by the distance x from the fixed end of the cantilever, taking into account its length L and thickness t , which is calculated using the following formula:²¹⁴

$$\varepsilon_s(x) = \frac{3u_z t}{2L^3} (x - L) \quad \text{eq. 17}$$

The vertical deflection u_z is imposed at the free end of the cantilever. By applying a deflection u_z of approximately 150 μm in the vertical direction, a surface strain of about 0.5% can be achieved. When considering a thin film deposited on a rigid cantilever and assuming the thin film approximation, the surface strain gradient along the cantilever is entirely transmitted to the thin film.^{215,216}

4.3.2 Design and construction of the stress chip holder

During the design and construction of the stress chip sample holder, a significant challenge was encountered in achieving complete independence between the bending of the cantilever on the stress chip and the movements of the SECCM. To overcome this challenge, an additional 3-axis moving system was integrated and installed on top of the SECCM positioner. This new moving system enabled the independent bending of the cantilever, providing the necessary level of control required for SECCM experiments. As part of the design process, an initial draft of a potential holder was created.

As shown in Figure 32 a), which is representing a first draft of the design, three micrometer screws were used to move a bending tip in 3 dimensions (X,Y and Z). For the Z dimension a piezoelectric micrometer screw (Figure 32 b)) was used to move the tip with high accuracy to bend the cantilever after a rough approach with the micrometer screw. To enlarge the possible bending distance using piezo electric equipment, a piezo element with a range of 100 μm was used to bend the cantilever after contact with the bending tip in this range with an accuracy of 0.2 nm.²¹⁷ In addition, the designed holder is fixing and at the same time electrically contacting the top of the stress chip. Therefore, the stress chip is placed in a small pit that the top of the chip is

in the same height as the holder plate. For fixing and contacting the chip a copper plate is used to press the chip down gently.

After bending the cantilever, the SECCM capillary is approached with an individual 3-axis movement system close to the surface of the stress chip (Figure 32 c) and d)) and SECCM experiments can be performed independently of the bending position. In order to bend the cantilever on the stress chip in both directions (up and down for having compressive or tensile stress in the film respectively) a draft of the holder with free space and a hole under the stress chip was designed (Figure 32 e) and f)).

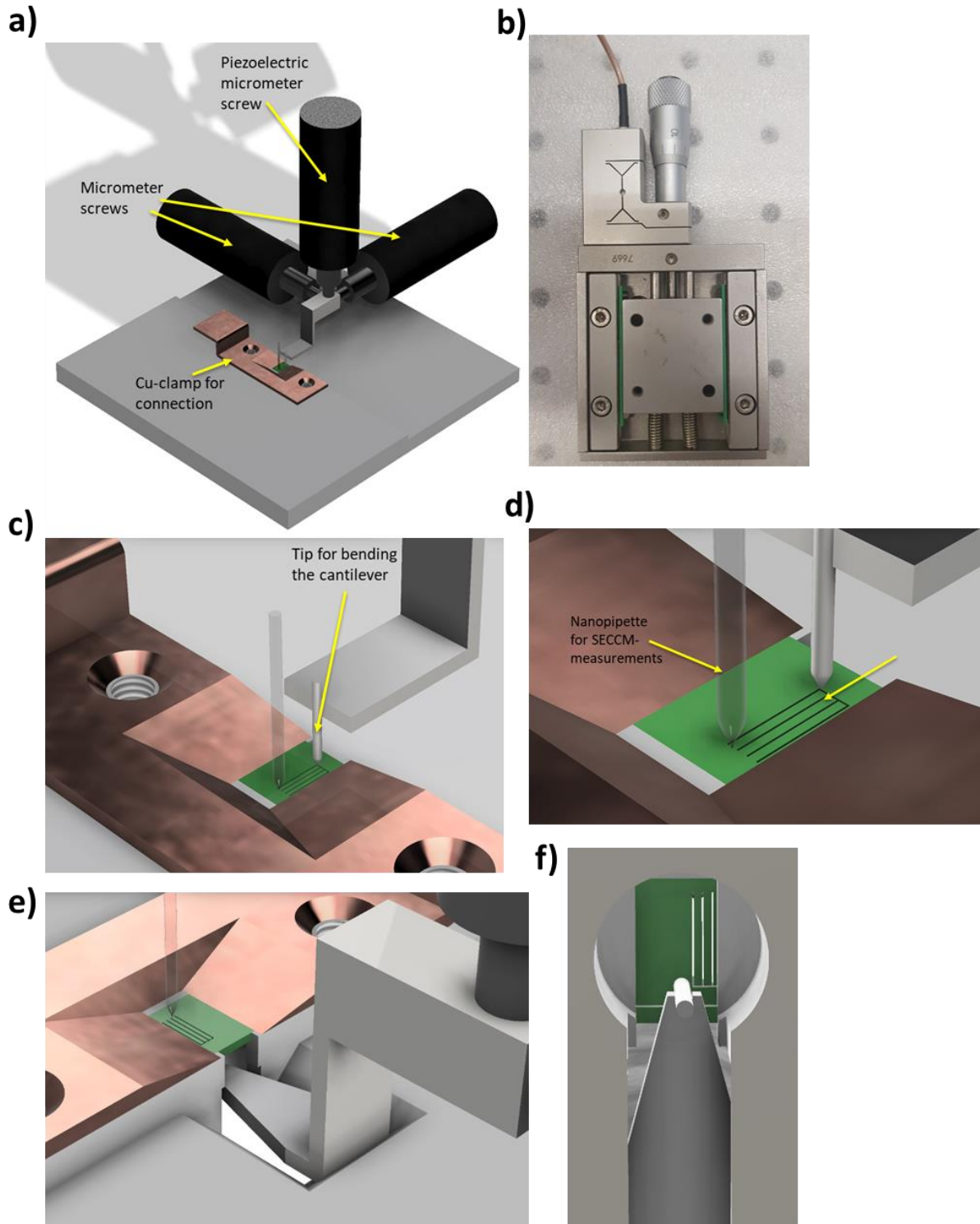


Figure 32: First draft of the stress chip holder: a) Overview of the holder, b) piezoelectric screw, c)-d) zoom-in towards the stress chip and contacting area, e)-f) possible realization of a lifting up technique for the cantilevers.

The cantilever holder/bending system was designed and built in the fine mechanics workshop at the RUB. Armin Lindner from the fine mechanics workshop provided support for the visualization and construction of this holder. The result is shown in Figure 33.

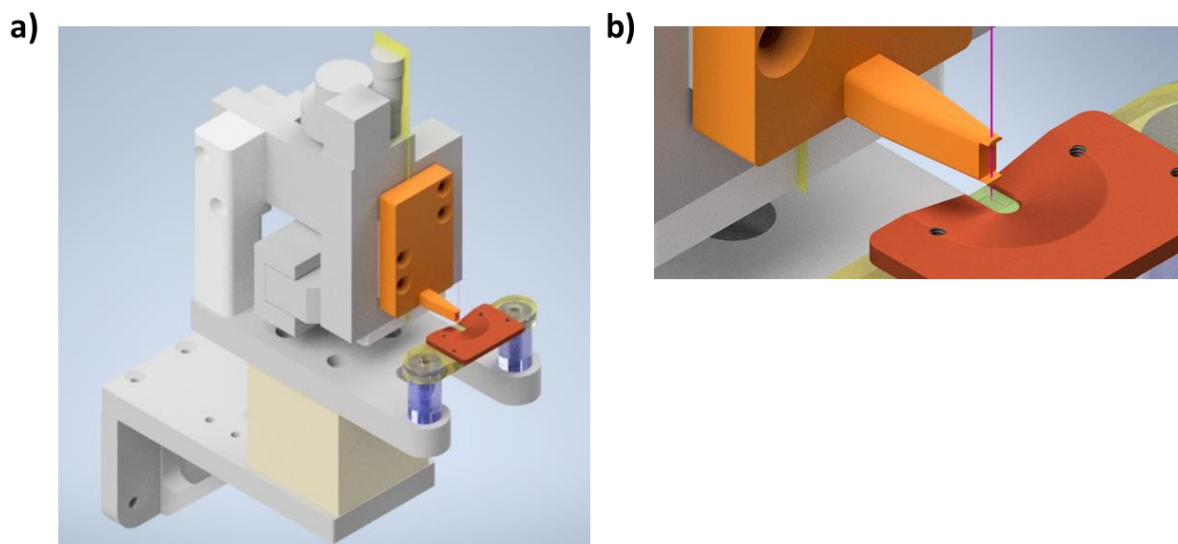


Figure 33: Constructed stress chip holder (Illustration made by Armin Lindner, fine mechanics workshop RUB): a) Overview of the holder, b) zoom into the contacting area.

4.3.3 Integration of Gas-/Ar-chamber

Figure 34 illustrates a gas-tight chamber prototype that was developed and integrated into the SECCM setup to examine the impact of altering the atmosphere surrounding the electrolyte drop on current responses in the CV. The prototype consists of a sample box that encloses the base plate and copper plate, effectively creating a sealed environment around the stress chip. Positioned on the top surface of the sample box is a hole through which the SECCM capillary tip enters above the stress chip. This hole serves a dual purpose, allowing for easy observation of the capillary tip with a camera during the approach towards the surface. It is designed to be of appropriate size, providing clear visibility while preventing air leakage back into the chamber. To ensure airtightness, the edges of the box are covered with Teflon. Additionally, a continuous flow of argon (Ar) is introduced into the chamber through a tube connected to an inlet at the bottom of the Ar chamber. This purging flow of Ar prevents air leakage inside the chamber. Furthermore, to maintain humidity and prevent the drying out of the hanging drop at the capillary tip, the Ar flux is directed through a bubble counter filled with water.

Since Pt was used as a model system sputtered on the stress chip, the electrocatalytic reactions occurring on Pt has to be analyzed from the recorded CVs. The aim of the project is to find catalysts for the hydrogen evolution reaction occurring at potentials between -0.1 V and 0 V vs RHE representing the activity area of most Pt-based

catalysts for HER⁷ which is why the focus on analyzing the CV is in the potential area close to 0 V vs RHE. In this area on the one hand the HER and hydrogen adsorption and desorption is happening. On the other side, Pt is also an efficient catalyst for the ORR which is occurring in potentials starting with 0.8 V vs RHE increasing in reductive potentials.²¹⁸ This means that for experiments performed in air (oxygen containing) the HER, hydrogen adsorption, desorption and ORR are overlapping in same potential ranges. To obtain CV and LSV measurements on Pt which show comparability within one scan and with experiments provided by literature the experiments are run in Ar atmosphere instead of air.

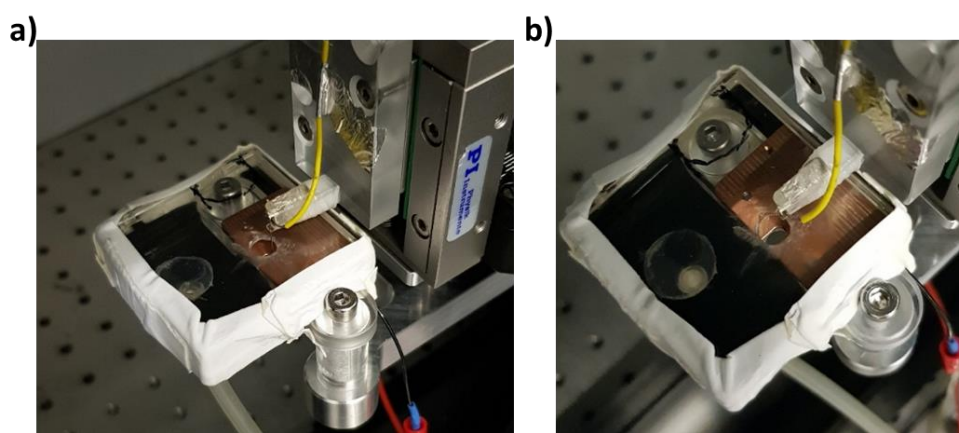


Figure 34: Prototype of the Ar chamber – A sample box surrounds the base plate and copper plate, enclosing the space around the stress chip. The hole on the top surface allows entry for the SECCM capillary tip and facilitates observation with a camera during tip approach. To prevent air leakage, a continuous flow of argon (Ar) is purged into the chamber through a tube connected to the bottom inlet of the Ar chamber. A bubble counter filled with water is used to humidify the dry Ar stream and prevent drying of the capillary tip. Teflon is sealing the box from the sides.

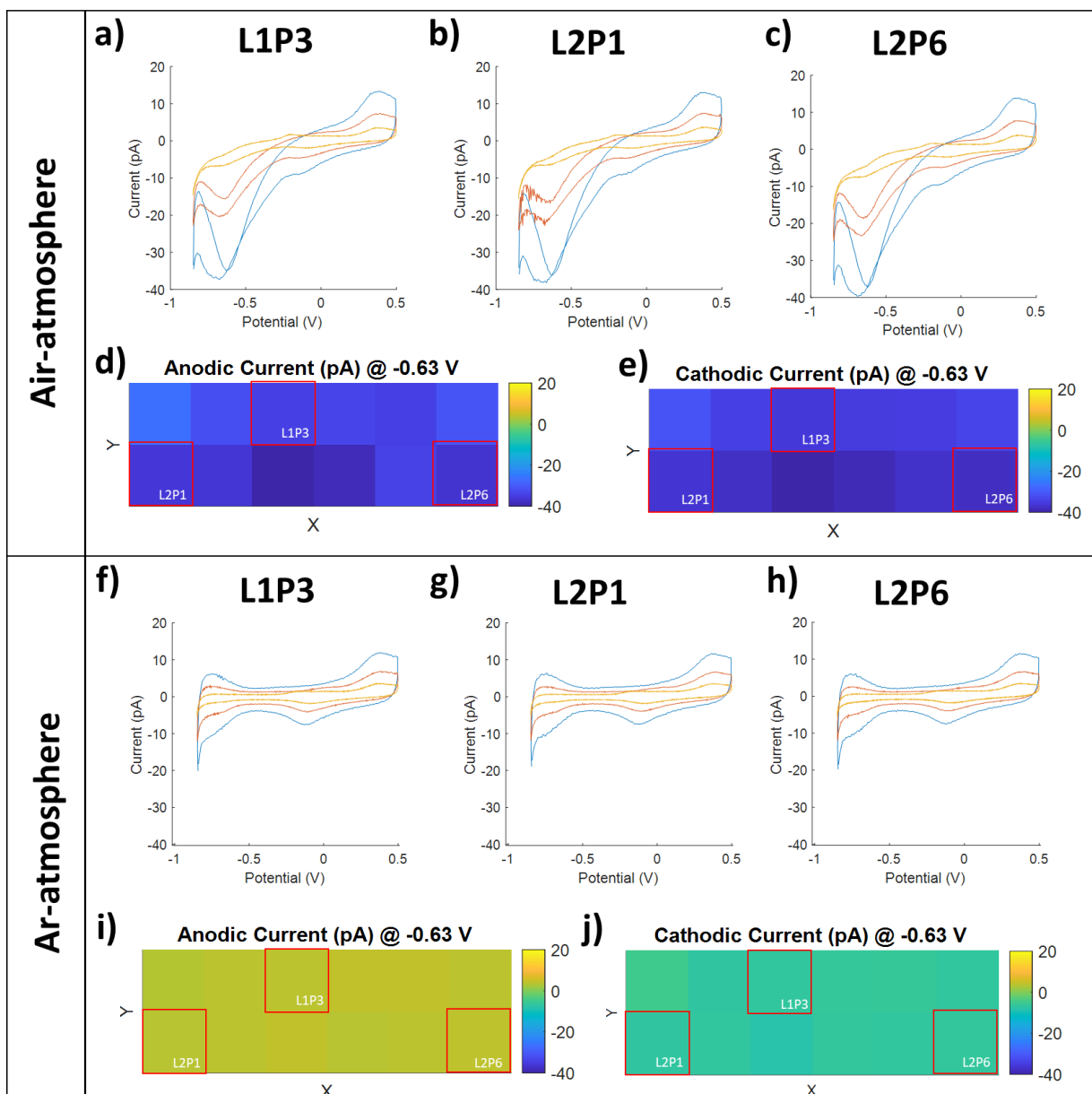


Figure 35: SECCM scans on stress chip sputtered with Pt (SID: 0005069) with and without oxygen suppression; current responses with scan rates of 200, 500 and 1000 mV/s in yellow, red and blue respectively for 3 exemplary landing spots (L1P3, L2P1 and L2P6) in air (a), (b), (c)) and in Ar (f), (g), (h)); corresponding heatmaps of current responses at -0.63 V vs Pt in 0.1 M HClO₄ in SECCM scan in air (d) and e)) and Ar (i) and j)) for anodic and cathodic CV scan direction respectively.

Figure 35 depicts the outcomes of SECCM experiments conducted on stress chips featuring a sputtered layer of Pt, aiming to assess the influence of different atmospheric conditions surrounding the SECCM capillary tip. The SECCM experiments were conducted using a single barrel capillary configuration and employed a hopping mode for scanning. The SECCM experiments utilized a single barrel capillary constructed from quartz glass. The capillary was fabricated using a laser puller, resulting in a size of approximately 600 nm. To evaluate the functionality of the gas chamber, a Pt wire was utilized as a quasi-reference counter electrode (QRCE). It is important to note that

the Pt wire does not serve as a traditional stable reference electrode since redox reactions at the QRCE can cause changes in the reference potential.²¹⁹ However, considering the relatively short time intervals during which each spot is measured, the Pt wire provides a sufficiently stable response, allowing for a comparison between different atmospheric conditions and ensuring overall experiment reproducibility. The potential provided is referenced against Pt in 0.1 M HClO₄, which corresponds to a pH of 1. Two sets of scans, comprising 2 x 6 spots, were performed both with and without argon (Ar) purging. Each spot underwent three cyclic voltammetry (CV) experiments, employing different scan rates (200, 500, and 1000 mV/s), and encompassing five cycles each. The final cycle of three exemplary spots from the SECCM scan carried out under an air atmosphere is presented in Figure 35 a), b), and c). On the other hand, Figure 35 f), g), and h) showcase the results obtained from experiments with Ar purging.

Overall, the CVs obtained at various scan (Figure 35) rates exhibit an increasing trend in current values as the scan rate increases. This observation can be attributed to diffusion processes occurring at the surface of the working electrode as described in chapter 2.3.1.¹³² Although the current peaks associated with redox reactions occur at the same potentials, their magnitudes differ at various scan rates. Both of these phenomena are clearly evident in the recorded CVs. For the analysis of different activity regions on samples with heterogeneous activity distribution considering hydrogen adsorption and desorption processes and the hydrogen evolution reaction it is advisable to examine the CVs obtained at the highest scan rates. This choice is based on the fact that, considering the small surface area of the electrode (tip size of the capillary), higher current values facilitate signal identification. In addition, an easier comparison of activity is also feasible due to the potential dependence of the reactions because with higher currents the detection of small potential differences caused by different activity becomes easier to detect.

The CV profiles obtained under the same atmospheric conditions for both air and Ar exhibit remarkable similarity within a single scan for all three locations, demonstrating the reproducibility of the SECCM experiments. However, a noticeable disparity in current responses is observed when transitioning from an air atmosphere to an Ar atmosphere between -0.2 V and 0.85 V vs Pt in 0.1 M HClO₄. In the potential range mentioned, the CVs recorded in air reveal an increased negative current for both the cathodic and anodic branches, in contrast to the CVs obtained in an Ar atmosphere.

Additionally, when suppressing oxygen during the experiments, a discernible increase in negative current at the anodic side (sweep from positive to negative potentials) and positive current at the cathodic side is detected, particularly for more negative potentials. These observations can be effectively depicted using activity maps, which visualize current values for specific potentials using a predefined color code. Figure 35 d) and e) present the anodic and cathodic currents, respectively, during the last cycle of the CV at a potential of -0.63 V vs Pt in 0.1 M HClO₄ for experiments conducted in an air atmosphere. Conversely, Figure 35 i) and j) illustrate the equivalent results for experiments performed under an Ar-purged environment.

The CVs obtained in Ar atmosphere exhibit characteristics consistent with those reported for Pt.^{220,221} While there are no distinct peaks associated with specific adsorption or desorption processes on particular crystal phases, as observed in conventional electrodes,^{222,223} the overall shape of the CVs aligns with reported experiments on Pt nanoelectrodes with comparable electrode area sizes.^{220,221} Within the CVs, the processes of hydrogen adsorption and desorption become apparent at potentials ranging from -0.85 to -0.5 V vs Pt in 0.1 M HClO₄, while Pt oxidation and reduction reactions occur between -0.3 V and 0.5 V vs Pt in the same electrolyte solution. A visible double-layer region can be observed in the potentials spanning from -0.3 to -0.5 V vs. Pt.

The different values of current responses potentials close to -0.63 V vs Pt in 0.1 M HClO₄ are indicating the hydrogen adsorption and desorption before the hydrogen evolution reaction.^{220–222} Since Pt is an efficient catalyst for the oxygen reduction reaction,²²³ the potential area in which this reaction is happening is overlapping with the hydrogen adsorption and desorption, which is causing the increased negative currents in Figure 35 e), f), g).

The visual representation of these observations can be seen in the color maps. In the absence of oxygen suppression, the color map displays a consistent dark blue shade, indicating negative current values. On the other hand, in the Ar-purged experiments, the color map exhibits less negative currents for the cathodic side, represented by shades of green, and positive currents for the anodic side, depicted by shades of yellow. The utilization of color maps provides a significant advantage when comparing current values at the same potentials, as it enables an immediate visual response for analysis. By employing color mapping, variations in current magnitudes and directions can be easily observed and compared, facilitating the interpretation of experimental

results. This visual representation enhances the efficiency and effectiveness of data analysis, allowing for quick insights and identifying patterns or discrepancies in current responses.^{224,225}

Since suppressing the oxygen reduction reaction and providing comparable CVs results with those found in the literature was proven, an Ar chamber was constructed in a robust and easily accessible manner, facilitating the convenient exchange of different stress chips. Furthermore, the use of a consistently constructed chamber for each experiment provides a high level of reliability and stability. The chamber's construction ensures that it consistently delivers the same argon flux and moisture conditions for every experiment. This reliability and stability contribute to the overall consistency of experimental conditions, allowing for more accurate and reproducible results across different experimental runs. The Ar chamber was fabricated at the fine mechanics workshop (RUB, Armin Lindner) and is illustrated in Figure 36. The chamber consists of a base plate with indentations designed to securely hold the stress chip in place to prevent any movement once it is positioned. Additionally, a gas inlet was incorporated to allow for connection to an argon supply tube. As the stress chip holder has the capability to bend the cantilevers of the stress chip either up or down, another base was created, featuring a hole beneath the stress chip indentation to enable bending of the cantilevers from beneath the sample.

For the chamber enclosure, a top made of acrylic glass was utilized, providing visibility inside the chamber. To prevent any leakage between the base plate and the top, a rubber sealing frame is employed. This rubber frame serves as a barrier, ensuring a tight and secure seal between the base plate and the top of the chamber, effectively preventing any unwanted air or gas leakage. A circular opening with a diameter of 0.5 cm was incorporated to accommodate the SECCM capillary tip. This opening serves the dual purpose of allowing proper camera observation of the tip for precise positioning while also preventing significant air leakage into the chamber. Additionally, a reservoir for filter papers soaked in water was included next to the gas inlet to ensure a moist gas atmosphere within the chamber. The entire construction was designed to fit onto the columns of the stress chip holder, effectively replacing the initially constructed base plate.

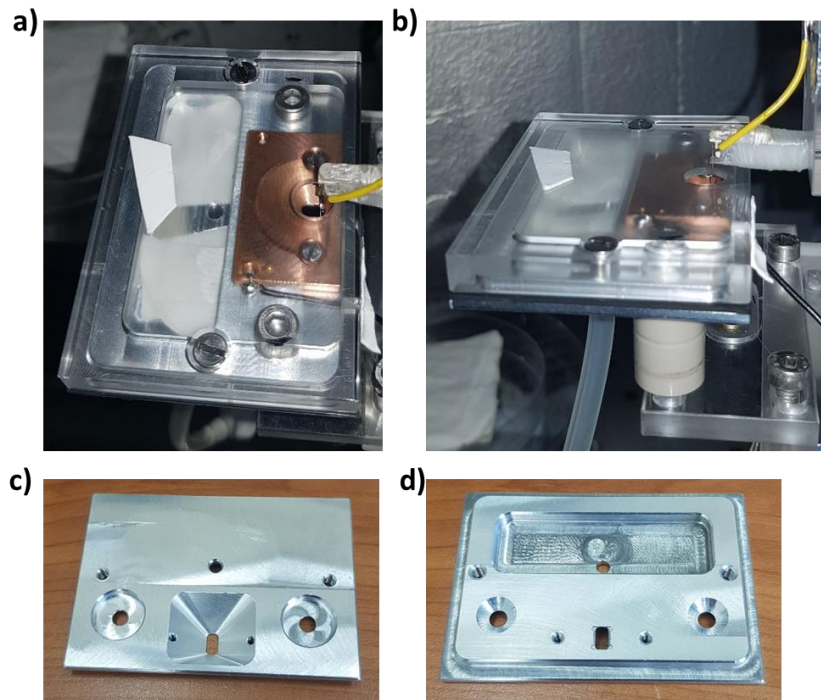


Figure 36: Ar chamber fabricated in the fine mechanics workshop (Armin Lindner) with different bases: a) top view and b) side view of the sample holding assembly with Ar chamber, c) upside down view of and d) top view of the base.

4.3.4 Bending the cantilever on the stress chip

Since the aim of this experimental configuration is to strain a metal film on a cantilever, the bending needs to be achieved with utmost precision. As previously described, a thin metal pin is utilized to bend the cantilever on the stress chip. The metal pin is affixed to an acrylic glass holder, which is connected to a piezoelectric micrometer screw (Figure 32 b). Through this rigid connection, which results in a negligible bending of the pin holder, the bending pin can be moved up and down in direct correlation to the displacement of the micrometer screw. Thus, the bending movement is accurately determined by the distance covered by the micrometer screw.

For precise bending, it is necessary to establish a reference position that sets the initial bending distance of the cantilever to zero. This reference position is determined by the contact between the metallic pin and the surface of the metal film. To fix this position, the electrical contact between the pin and the surface is utilized. The pin is electrically connected to a copper wire through soldering (Figure 36 b)). By using a digital multimeter, the position of the electrical contact between the pin and the stress chip surface is identified and secured. From this fixed position onwards, the bending distance is measured and recorded accurately.

Prior to conducting measurements on the stress chip, an initial breaking test was conducted to determine the bending area of the cantilever. As previously described, the bending tip was brought into contact with the cantilever. Subsequently, the micrometer screw was used to gradually bend the tip and, consequently, the cantilever downwards. At intervals of 10 μm , photos were taken to document the bending process. Figure 37 displays all the captured photos until the point of breaking. It is noteworthy that the cantilever broke after reaching a bending distance of 140 μm .

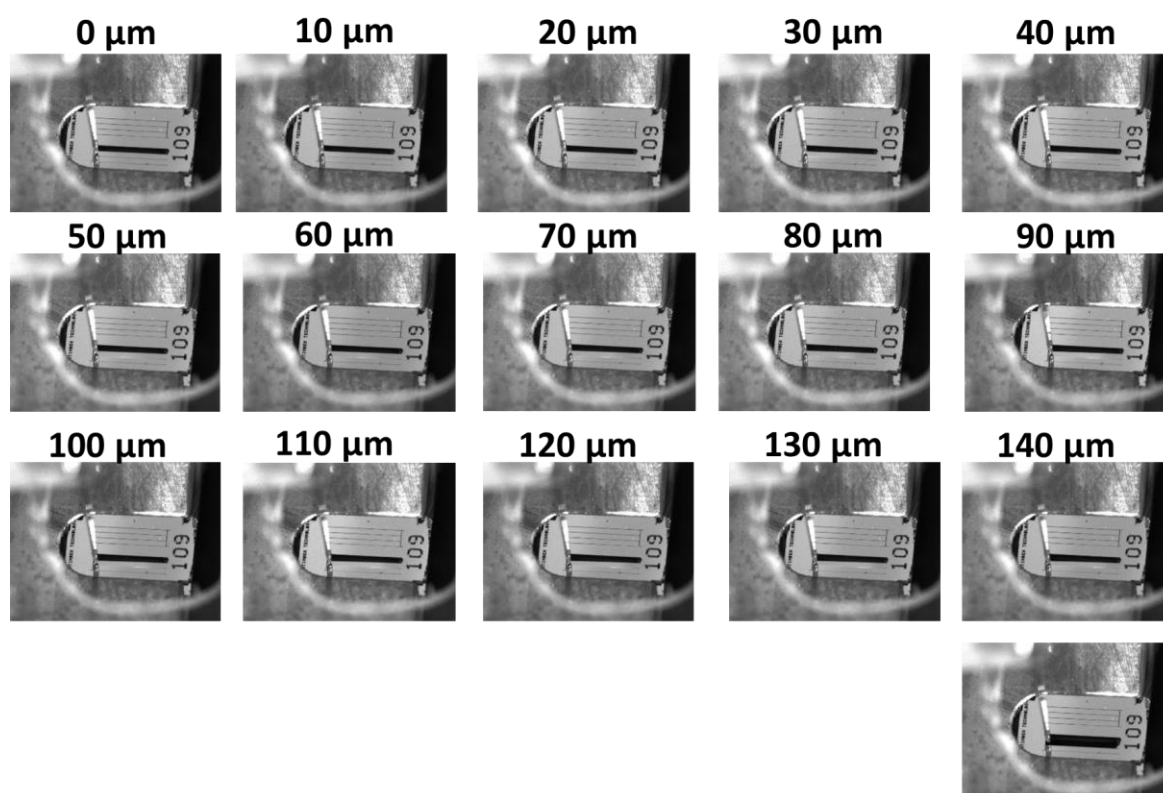


Figure 37: Photographs of the stress chip with different bending stages of one cantilever.

4.3.5 Bending the cantilever on the stress chip and measuring with SECCM

The primary objective of the project is to analyze the catalytic activity of the hydrogen evolution reaction under various strain states. These strain states are achieved by bending the cantilever on the stress chips, thereby inducing external stress within the cantilever structure. It can be inferred that the same value of stress is present in the catalyst film on top of the stress chip as in the Si cantilever which is serving as support. This inference is based on the thin thickness of the film relative to the height of the cantilever.

The concept behind analyzing the catalytic activity based on the strain state involves bending the cantilever using a bending tip positioned at the free end, and subsequently

conducting LSVs and CVs at the fixed end. According to strain simulations,^{215,226} this location represents the area of highest stress on the bent cantilever.

In an initial experiment, the cantilever on the stress chip was subjected to two different strain states to observe differences in the recorded current response during CVs. For this test, the cantilever was brought into contact with the bending tip (Figure 38 b), red), using the approach method described before to verify the contact point. A CV measurement was recorded at this contact position, referred to as “contact position”. Subsequently, the cantilever was further bent by an additional 50 μm (Figure 38 b), green), and another CV measurement was conducted at this position. After this initial reference position was fixed, these measurements served as initial investigations to assess whether different bending states would yield distinct electrochemical responses.

In the initially conducted experiments involving two different bending modes, an Ag/AgCl wire was employed as a QRCE in 0.1 M HClO₄. This setup allowed for the conversion of the potential to the RHE scale. During the experiment, three CV cycles were performed with a scan rate of 500 mV/s.

The CVs exhibit the characteristic shape expected for a Pt working electrode.^{220,221} The third cycle of the CVs is shown in red for the bending mode in contact position and in green for the bending mode at 50 μm . Hydrogen adsorption and desorption occur within the potential range of 0.2 V vs RHE to 0 V vs RHE, while HER takes place at 0 V vs RHE. This potential window is depicted in Figure 38 a) as an inset. The data is plotted without any additional modifications or averaging.

In terms of activity differences, which would be reflected by higher or lower current values at the same potentials, there is no significant difference observed in the plotted data between the two bending modes. This applies to both the hydrogen adsorption and desorption processes, as well as the hydrogen evolution reaction. However, a distinction can be made in terms of noise, with the 50 μm bending mode displaying a higher noise level compared to the contact position bending mode.

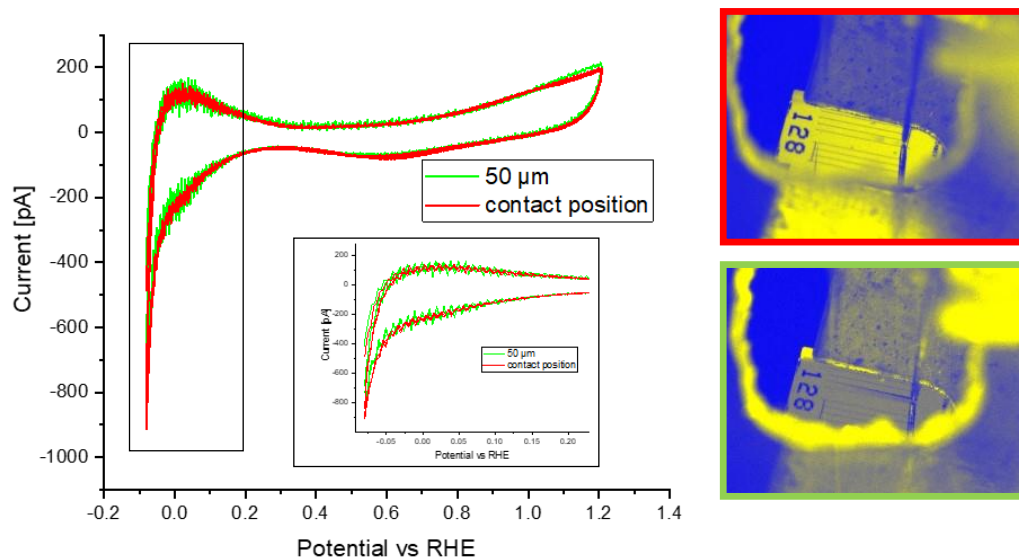


Figure 38: Comparison of two CVs in two different bending modes. Two electrode configuration with Ag/AgCl- wire as QRCE in 0.1 M HClO₄, making the conversion to RHE scale possible. Scan rate of the CV was 500 mV/s and the atmosphere was Ar.

The analysis of the CVs is influenced by the dynamic nature of the cyclic voltammetry measurement. Another approach to analyze the electrochemical reaction at the working electrode in the context of bending mode changes is to employ chronoamperometry. This technique involves observing the current signal at a constant potential, such as in the region where the HER occurs. By using chronoamperometry, the impact of bending on the current at a specific potential can be isolated, excluding the effects of dynamic measurements. Additionally, it allows for the examination of any noise changes that may arise from bending the cantilever on the stress chip.

To explore the relationship between the HER activity and the stress within the catalyst film, chronoamperometric measurements were conducted. Prior to performing the chronoamperometry, a CV was conducted to identify an appropriate potential for the HER analysis from the CV shape. The CV data, illustrating the potential range of interest, is shown in Figure 39 a). As shown in the inset of Figure 39 a), the hydrogen adsorption and desorption processes occur within the potential range of 0 to 0.3V vs RHE. The onset of the HER occurs at 0 V vs RHE. The selection of the potential for chronoamperometry depends on the expected magnitude of the effect. Considering the low effect size observed in the literature when studying the relationship between stress and HER activity,¹²⁶ it is recommended to choose a potential range where small differences in overpotential result in a significant difference in current

response. Hence, the potential region where HER is clearly taking place, specifically -0.082 V vs RHE (refer to Figure 39 a), was chosen for the chronoamperometry measurements.

In Figure 39 b), the results of the chronoamperometry measurements are presented. The experiment began with the SECCM capillary tip approaching the surface, followed by the initiation of current measurement between the QRCE and the working electrode. Due to the measurement software settings, the first applied potential was 0 V, referenced to the Ag/AgCl QRCE in 0.1 M HClO₄. Considering an open circuit potential (OCP) of the QRCE as 0.040 mV, the potential shift to the RHE scale is 0.309 V, resulting in the first potential applied as 0.309 V vs RHE. Comparing this value with the CV in Figure 39 a), it is evident that the first potential lies in the non-Faradaic region where no electrochemical reaction occurs.

Subsequently, the potential was switched to the HER region at -0.082 V vs RHE. As depicted in Figure 39 b), the current response initially decreases to -400 pA. However, the current response then exhibits an increasing trend, following a saturating pattern, rather than remaining constant. This behavior can be explained by the Nernst equation. Since the reaction at the working electrode involves H₃O⁺ ions, the reduction of these ions influences the activity coefficient of the reactants. A simplified explanation suggests that the change in cation concentration corresponds to a change in pH, resulting in a deviation of the applied potential from the reference potential. The consideration of the change in protons and its impact on the potential value is crucial, particularly due to the small volume of electrolyte in the hanging drop from the SECCM tip. This observation highlights the significance of this factor in data analysis. Similar effects have been reported in the literature for SECM experiments.²²⁷ Therefore, taking into account the influence of cation (H₃O⁺) concentration on the potential is essential to ensure accurate interpretation and analysis of the experimental results.

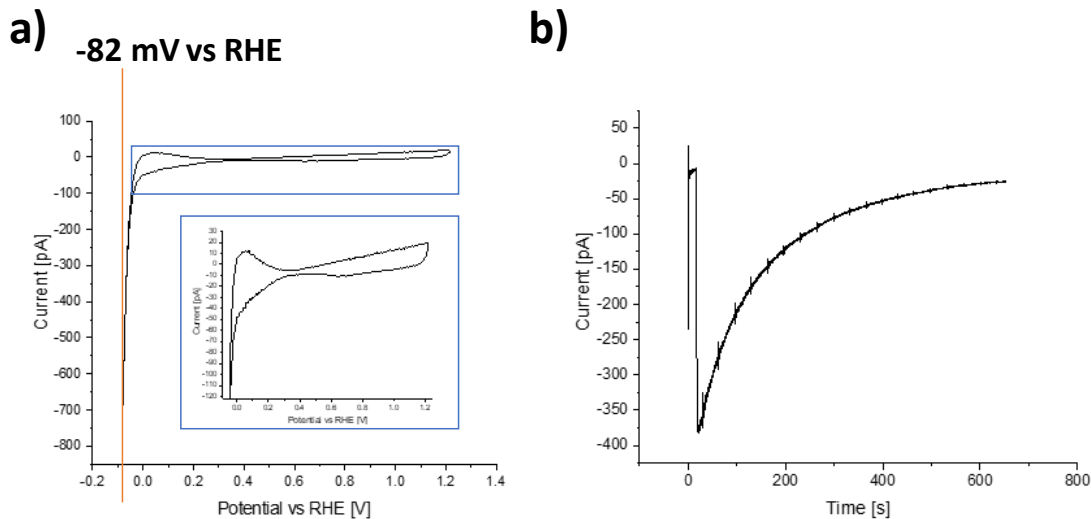


Figure 39: Electrochemical measurements on Pt cantilever at the position of highest possible stress, two electrode configuration with Ag/AgCl- wire as QRCE in 0.1 M HClO₄. a) CV with scan rate of 500 mV/s, potential of highest measured current at HER reaction marked with yellow line, inset visualizing a zoomed in image of the characteristic CV shape of Pt, b) Chronoamperometric measurement performed at -82 mV vs RHE.

To separate the effects of activity and pH change caused by the bending of the cantilever on the stress chip, a periodic bending approach is employed. This is achieved by applying a sinusoidal function using a function generator. By doing so, the pH changing effect and the sinusoidal magnitude can be isolated by fitting the current signal with an exponential function and correcting the current signal with the fitting values. This allows for the identification of the specific effect of stress variation on the HER activity, independent of the pH change. Through this approach, the influence of the stress-induced changes on the catalytic activity can be analyzed more accurately. To perform the experiment, the procedure remains the same as before. The SECCM capillary is approached to the surface, and the current is measured at a constant potential of 0.309 V vs RHE. Then, the potential is switched to the HER region (-0.082 V vs RHE). However, in addition to this, the cantilever on which the SECCM tip is positioned, is subjected to sinusoidal bending using a function generator. This bending is applied as an alternating voltage signal to the piezo element moving the bending tip, resulting in a periodic bending motion of the cantilever. The applied bending pattern is shown in Figure 40 b) in red. A frequency of 100 mHz is used to bend the cantilever in a piezo displacement variation between 30 and 70 μm at the free end of the cantilever. The accurate moving distance of the bending tip is assured by the accuracy of the piezo element.²¹⁷ This periodic bending allows for the isolation and analysis of the effects of stress variation on the HER activity.

The sinusoidal bending of the cantilever resulted in a sinusoidal current response (Figure 40 b, black). Figure 40 c) represents the correction of the current signal using an exponential fit and subtracting the value of this fit which is corresponding with the pH dependent effect from the current signal. The resulting corrected current (Figure 40 c, green) is showing the current magnitude of 42 pA between 30 and 70 μm bending, which is getting smaller while oscillating until it reaches 17 pA after 8 oscillation cycles. Although the current signal is giving a clear response in accordance with the sinusoidal bending, a complete isolation of the stress effect on the activity is not given because both, a changing of the drop size covering the sample as well as electromagnetic fields could cause a similar effect on the current signal.

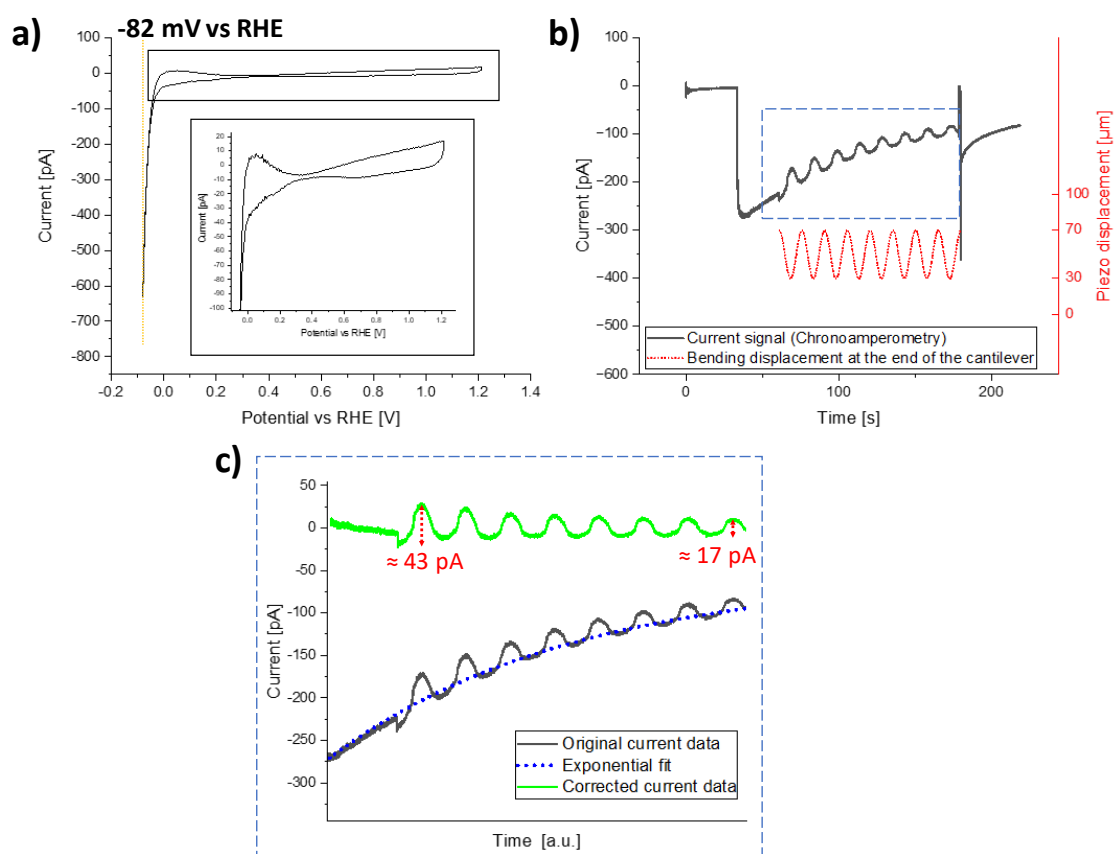


Figure 40: Electrochemical measurements on Pt cantilever at the position of highest possible stress, two electrode configuration with Ag/AgCl- wire as QRCE in 0.1 M HClO_4 using sinusoidal bending. a) CV with scan rate of 500 mV/s, potential of highest measured current at HER reaction marked with yellow line (-82 mV vs RHE), inset visualizing a zoomed in image of the characteristic CV shape of Pt, b) Chronoamperometric measurement performed at -82 mV vs RHE, current signal (black) with sinusoidal bending starting at approximately 65 s after starting the experiment and piezo displacement representing the bending of the cantilever (red), c) Correction of the current signal using an exponential fitting (blue) to receive the current magnitude (green) of the bending effect separated from the pH dependent effect.

To address the complexity and challenges associated with the simultaneous changes and isolation of factors in the bending system, a different approach is introduced to

investigate the dependency of stress in the catalyst film and catalytic activity. The SECCM system offers a significant advantage in terms of high throughput, allowing the scanning of a large number of spots on a sample surface within a reasonable timeframe.

One key aspect utilized in this approach is the presence of a stress gradient within the cantilever when it is bent on the stress chip. It has been observed that bending induces varying strains at different spots along the cantilever, which are transferred to the thin-film catalyst layer deposited on top of it.²¹⁵ The idea is to perform a scan alongside the cantilever using the cantilever on the stress chip. This eliminates certain limitations of the system, such as changes in drop size during cantilever bending, as the activity comparison can be made within a single scan with similar or comparable spot sizes. Moreover, the electrical signals do not overlap due to the dynamic bending of the cantilever, because there is no change in applied voltage for the piezoelectric screw. Furthermore, the high throughput nature of SECCM experiments provides statistical evidence by itself, increasing the reliability of the results.

Based on simulations and mechanical experiments, it has been observed that when a cantilever is bent, a gradient of external stress is generated along the cantilever, with the maximum stress occurring in the region of the fixed side of the cantilever.^{215,226} In contrast, the stress chip area, which is not influenced by the bending, virtually no external stress during the bending process. Taking advantage of the high throughput capabilities of SECCM, specifically its spatial resolution and ability to measure a large number of spots, a strategy can be employed to exploit the significant difference in external stress within a single scan area. By scanning across the fixed side of the cantilever, the SECCM can capture measurements on both the bent region of the cantilever and the stress chip area that is unaffected by bending. This approach allows for a comparative analysis of the catalytic activity between the strained region of the cantilever and the stress-free region on the stress chip. By examining the activity differences between these two areas, it may be possible to discern the influence of external stress on the catalytic activity of the hydrogen evolution reaction.

In Figure 41, the results of the experiments following the alternative approach are presented. A series of five SECCM scans were conducted in the same area of the cantilever, with each scan consisting of a grid of 6 x 26 measurement spots. The long scan direction was aligned alongside the cantilever, allowing for the observation of the stress gradient along the cantilever. By performing multiple scans in the same area, it

was possible to capture the variations in external stress across different regions of the cantilever. Additionally, having six measurement spots in each scan provided the opportunity to average the data and reduce potential measurement errors. Due to the size limitation of the piezo cube, the scan area covered a distance of 20 x 100 μm , with a hopping distance of 4 μm between each measurement spot in both lateral directions. After each scan, the middle of the scan grid was shifted by 2 μm in one direction. This ensured that for every scan, the same area of the cantilever was targeted, but with a slightly different position due to the relative movement of the scan grid. As a result, each scan covered a fresh sample surface, introducing a slight neglectable variation in the scanned surface position by a few micrometers. Despite the small variation in the scanned surface, the stress gradient induced by the bending of the cantilever remained consistent within each scan. This allowed for a comparative analysis of the stress-induced effects on the catalytic activity across different spots within the same scan.

Figure 41 b) depicts the experimental setup, showing a photograph of the cantilever on the stress chip (represented in black and white) and the region where the SECCM scans were conducted (represented in yellow and blue). The SECCM scans covered a specific area, with each scan slightly shifting the middle point by 2 μm in one direction. This ensured that the same stress gradient induced by the cantilever bending was observed within each scan, despite slight variations in the scanned surface. During each scan, a LSV was performed at every spot using a scan rate of 2.0 V/s in the HER region. The LSV measurements covered a potential range from 0 V vs RHE to -0.18 V vs RHE. Figure 41 a) displays the spatially illustrated recorded current data specifically at -0.18 V vs RHE using a color code. The SECCM scan direction for the activity map was from top to bottom, starting from the upper left corner and switching between right and left direction for each line, as illustrated in Figure 41.

The investigation involved a series of scans to detect changes in activity caused by bending the cantilever and inducing stress in the film. The procedure consisted of the following steps: First, a scan was conducted in the specified area without bending the cantilever of the stress chip. Subsequently, the cantilever was bent downward by 60 μm at the free end. Another scan was performed with a relative lateral displacement of 2 μm . Following this, the bending was released, and a subsequent scan was taken. These steps were repeated five times in total. Additionally, the entire procedure was repeated at least twice to ensure the reliability and consistency of the results. By

comparing the scans obtained from different bending modes and repetitions, the aim was to determine whether changes in current were solely attributed to the bending of the cantilever or influenced by the repetition of the experiments.

Figure 41 a) displays the results of the experiments, depicting the recorded current data at a potential of -0.18 V vs RHE. The color-coded representation provides a visual representation of the spatial distribution of current values across the scanned area. Accompanying Figure 41 a), the corresponding LSVs, showcasing the current response as a function of the applied potential for each spot in the scan. During the first scan of the experiments in the non-bent mode, a noticeable abrupt change in current magnitude is observed in the middle of the scan. This phenomenon is commonly observed in the initial SECCM scans following the preparation of the experiment and can be attributed to sudden changes in the capillary, such as the presence of an gas bubble or variations in wetting properties. It is worth noting that these occurrences, if present, tend to happen primarily at the beginning of the experiments and subsequently remain relatively constant without further sudden changes. To facilitate a more accurate comparison, only lines 4 to 6 from the first scan were selected, reducing the number of data points while still retaining significant information. Upon examining the subsequent scans performed following the aforementioned procedure, it is evident that with each scan, the current response at the potential of -0.18 V vs RHE increases in the scan direction (from top to bottom). This trend results in an overall incremental rise in the current magnitude from one scan to the next.

Tracking changes in activity caused by the bending of the cantilever in the x-direction (cantilever direction) of the SECCM scan is not as evident. It may be challenging to observe distinct variations solely attributed to the bending-induced stress in the catalyst film. Other factors, such as experimental noise, variations in the electrolyte, and potential fluctuations, could overshadow the specific effects of the cantilever bending on the catalytic activity. Therefore, it may require further analysis and careful interpretation to identify and quantify the influence of cantilever bending on the activity in the x-direction.

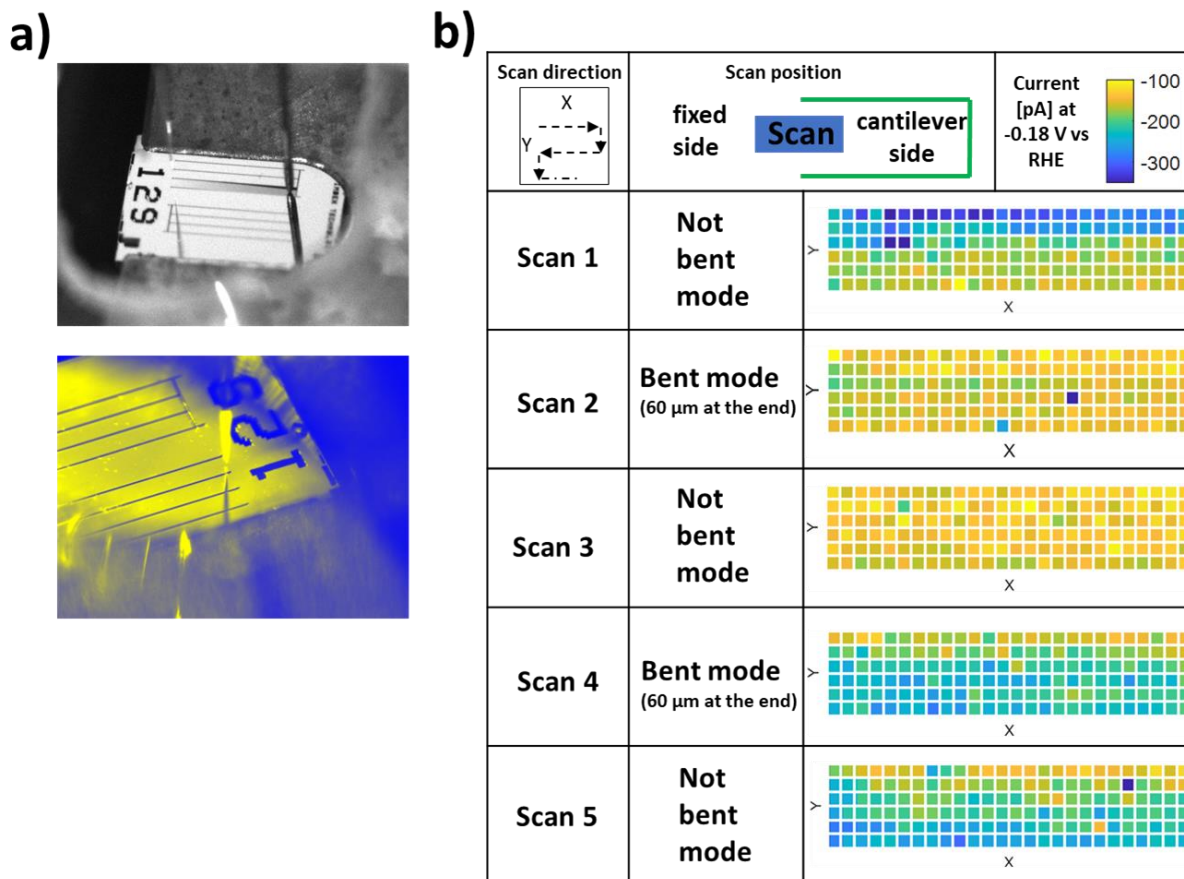


Figure 41: SECCM scan at the area of highest strain in film at different bending modes, two electrode configuration with Ag/AgCl- wire as QRCE in 0.1 M HClO₄, a) photographs of the bent cantilever (black and white) and the position of the SECCM measurements, b) activity maps of SECCM scan representing the current signal recorded in a LSV with scan rate of 2.0 V/s for 5 different bending modes.

To analyze the effect of cantilever bending on the catalytic activity, another procedure is applied to the five measured scans. Each scan is divided into three sections along the y-direction, which corresponds to the cantilever direction where changes in stress are expected during bending. The sections are labeled as "fixed side," "middle," and "cantilever side," representing their positions on the cantilever of the stress chip. For each section within a scan, the current values are plotted in a histogram and fitted with a Gaussian distribution. The arithmetic mean and median of the current values are then calculated. The objective of this analysis is to compare the differences between the median and arithmetic mean of the fixed side, where minimal stress is expected, and the cantilever side, which experiences the highest stress due to bending. The "middle area" is taken out of the analysis. By comparing the differences in current between the bent mode and non-bent mode scans, it becomes possible to identify any variations in current that may be attributed to the cantilever bending-induced stress in

the catalyst film. This analysis approach aims to provide an objective assessment of the current differences, independent of subjective perception.

Figure 42 illustrates the analysis procedure applied to the five SECCM scans in different bending modes. The histograms were created using the current values obtained from the LSV measurements at -0.18 V vs RHE, and Gaussian distribution curves were fitted using Matlab. In Figure 42 b this procedure is explained schematically. The arithmetic mean, representing the center of the Gaussian distribution, is shown as a straight line in each histogram for easier identification. The differences for both the arithmetic mean and median are plotted as a function of the LSV potential for each scan. Negative values of the differences indicate lower current values on the cantilever side compared to the fixed side, suggesting a decrease in activity due to bending.

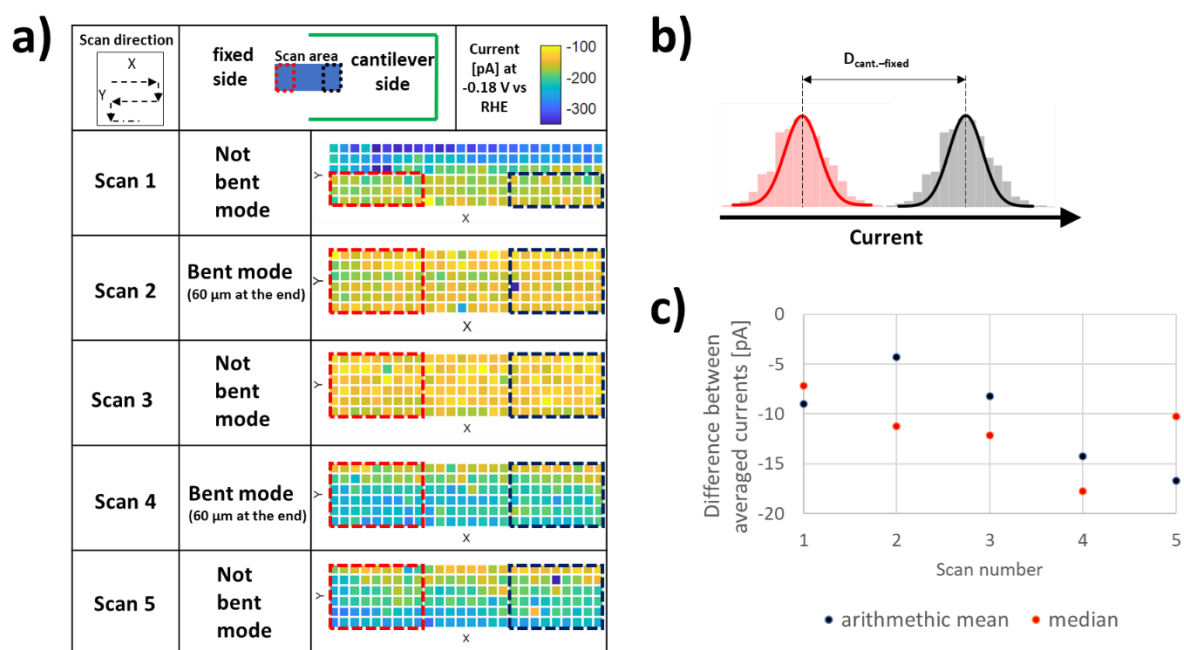


Figure 42: Further statistical analysis of the SECCM experiments represented in Figure 41. a) Activity maps of SECCM scan at the area of highest strain (centre of the scan at the position represented in Figure 41 b) film at different bending modes, two electrode configuration with Ag/AgCl- wire as QRCE in 0.1 M HClO₄, b) schematical explanation of the data procession using histograms of the current distribution of the LSVs (scan rate:2.0 V/s) at a potential of -0.18 V vs RHE for 2 zones within the SECCM scan, c) differences (differentiated between arithmetic mean and median) of the averaged currents in the area with lowest stress (blue frame) and the area with highest strain) green frame.

The comparison of the arithmetic mean and median reveals a consistent trend of decreasing change for every scan, regardless of the bending mode. Figure 42 c) specifically shows the differences in the arithmetic mean and median values at a potential of -0.18 V. However, no significant correspondence between the not bend and bent modes is observed, and there is variation between the median and arithmetic

mean. It should be noted that this approach to data processing may have limitations due to the loss of information in the statistical error.

Another approach to detect differences in the catalytic activity of the hydrogen evolution reaction (HER) along the cantilever on the stress chip is to perform a SECCM scan with cyclic voltammetry (CV) measurements and analyze the area of hydrogen adsorption at different bending states.

To investigate the influence of stress on the activity change, a specific potential range of 0 V to 0.2 V vs RHE, where hydrogen adsorption occurs, was examined. In addition to the fixed side of the cantilever, two more regions alongside the cantilever were investigated, one at a distance of 105 μm and the other at 900 μm towards the cantilever fixation. Based on stress simulations and experiments, it was expected that the stress in the cantilever direction would decrease, potentially resulting in a different activity change if detected.

In each of the designated regions, the experimental procedure involved performing a LSV after the approach at each spot, followed by a CV with three cycles, with particular focus on the last cycle. The results of these experiments, specifically the LSV measurements in the HER region, are presented in Figure 43.

The replicated experiments aimed to reproduce the previous findings, but similarly did not reveal any noticeable difference along the cantilever in the HER potential area. However, there was a difference observed in the scans performed at the cantilever side. Interestingly, the current response of the electrochemical cell appeared to overlap with the expected current response of an ohmic resistance.

Figure 43 illustrates the average of all CV responses from one scan, compared with scans from different bending modes or positions on the cantilever. Only the cathodic side of the CV, which represents the current associated with hydrogen adsorption, is shown in the plots. No clear difference corresponding to the bending mode is observed. It is worth noting that in the last scan, considering the measurement time, there appears to be a small difference (for the unbent mode after bending). However, this could also be attributed to a shift in the OCP) of the QRCE during the course of successive scans.

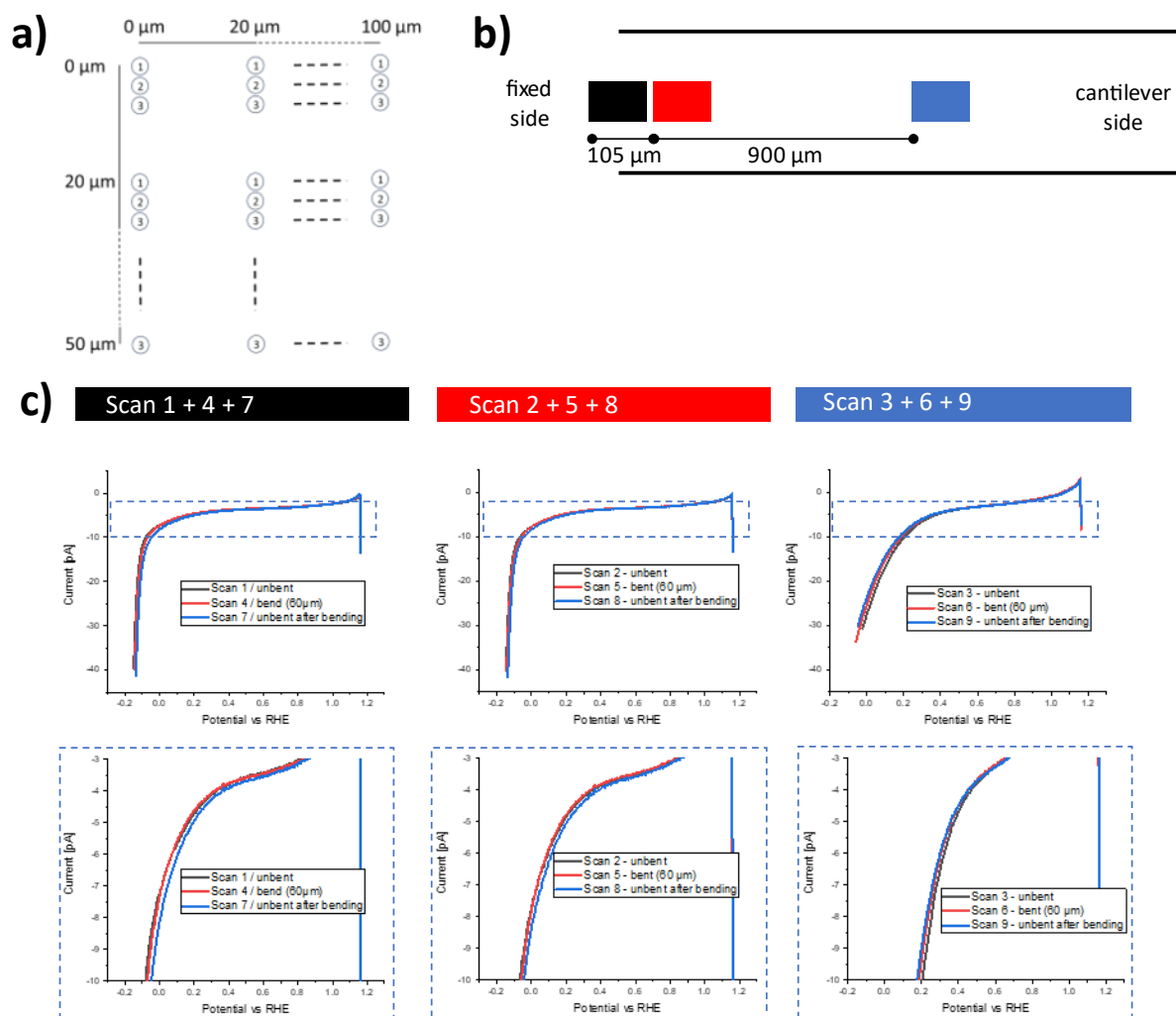


Figure 43: Multiple CV experiments within several SECCM scans in different regions of the cantilever of a stress chip coated with Pt. Experimental conditions: capillary tip size 125 μm, in Ar atmosphere, 0.1 HClO₄, cantilever bent with 60 μm at the free end, scan size 11x6 point (100 x 50 μm), 3 μm in between scans a) schematic representation of the scan within another scan to avoid measuring the same spot twice, b) regions of the scans on the cantilever of the stress chip, c) Average of cathodic scans of the CV experiments (scan rate 1 V/s) for 3 bending modes and 3 regions on the cantilever, blue frame representing a zoom-in into the region of hydrogen adsorption.

4.3.6 Problem analysis of the SECCM experiments on the stress chip samples

Despite the various approaches taken to investigate the relationship between strain in the catalyst film and catalytic activity in the hydrogen evolution reaction, no significant evidence of a direct correlation could be detected. Several factors contribute to the complexity and challenges faced in the measurement system, including potential shifts of the QRCE, variations in residual oxygen concentration within the electrolyte, and differences in spot size of the hanging drop at the cantilever tip. Additionally, issues related to the stress chip sample and the bending system introduce additional sources of noise and potential surface distortions.

The overall inaccuracy in the measurement system likely leads to the loss of sensitivity in detecting the expected change in activity, which may be relatively small. Moreover, it is possible that certain properties within the sample itself hinder the transmission of the strain induced by the cantilever bending to the surface of the stress chip. These sample-related factors can further contribute to the lack of observed correlation between stress and catalytic activity.

5. Conclusion and outlook

In the pursuit of discovering optimized electrocatalysts for energy conversion-related reactions, high-throughput experimentation techniques have proven to be invaluable tools in the analysis of electrocatalysts for energy conversion processes. By rapidly synthesizing and testing a wide range of materials, these techniques enable the generation of vast experimental datasets, providing critical insights into catalytic performance. The use of scanning droplet cell and scanning electrochemical cell microscopy has allowed for the screening of various electrocatalytic reactions, such as the hydrogen evolution reaction and oxygen reduction reaction, on diverse material configurations.

Through this high-throughput approach using the scanning droplet cell, novel high-entropy material systems and composition-dependent activity profiles have been discovered including (TiNi)-Cu-Hf-Pd-Zr and Co-Cr-Fe-Mo-Ni. Surprising combinations of elements previously considered non-active in catalysis such as Ti, Hf and Zr, have demonstrated significant influence on the catalytic behavior. The understanding of how different compositions affect the electrocatalytic reactions has been crucial in identifying optimized catalysts for specific energy conversion processes. Two successful approaches have been utilized to discover starting points in the vast search space of HEAs. In the first approach elements known for their catalytic activity are combined with elements which have not shown any significant catalytic activity. Another strategy for discovering new catalytically active HEA that was established using the element combination Co-Cr-Fe-Mo-Ni was to choose one specific HEA composition out of literature which was shown to be active and spread the composition space using high throughput methods for fabrication and characterization of the HEAs. These two approaches have resulted in promising HEA compositions and valuable insights for future investigations.

Furthermore, the large and growing datasets obtained through high-throughput experimentation, in this case especially scanning droplet cell measurements, serve as valuable resources for future machine learning applications. Machine learning techniques can utilize these datasets to make improved predictions and identify promising starting compositions for further exploration.

In the specific case of MoS₂, high-throughput methods, such as scanning electrochemical cell microscopy, have provided valuable insights into the electrocatalytic behavior of this 2D material. In this work SECCM allowed for the investigation of lateral heterogeneity in large single-layer MoS₂ samples, which were grown using chemical vapor deposition and subsequently transferred onto conductive substrates. Through SECCM activity maps, the identification of significant variations in the catalytic activity of MoS₂ over extended areas was possible. Also, the comparison between single- and multilayer of the material could be investigated. Since no difference in activity was recorded between single-layer and multi-layer MoS₂, the observed lateral heterogeneity can be attributed to the presence of polymer residues or a layer of water or gas bubbles that formed between the MoS₂ sheet and the GC during the transfer process. These findings shed light on the spatial distribution of catalytic sites within the material, crucial for optimizing the performance of MoS₂-based electrocatalysts.

The investigations on strained stress chips have been a valuable learning experience, even though clear dependencies of the strained cantilever on the stress chip influencing the catalytic activity of the HER were not evident. The process of exploring the potential of the stress chip involved significant achievements, including successfully integrating it into the SECCM setup, establishing a functional atmosphere chamber for SECCM measurements, and implementing various methods for analyzing the stress chips. However, further optimization of the technical aspects of the SECCM setup and the sample configuration is still necessary to obtain conclusive and reliable findings. It is important to acknowledge that unexpected results and failures are an inherent part of the research process. Despite encountering obstacles, every step taken in the pursuit of knowledge brings us closer to the goal.

In the end, it is the collective efforts, even the smallest ones, that propel scientific progress forward. The journey of exploration and discovery continues, and with perseverance and dedication, we move towards a deeper understanding of electrocatalysis and energy conversion processes. These endeavors contribute to the advancement of sustainable technologies and ultimately pave the way for a greener and more sustainable future.

6. Experimental procedures

In this subsequent chapter, the methods and tools employed to obtain the results presented in this thesis are detailed. The aim is to provide a suitable context for the results by describing all the synthesis, preparation, and characterization methods utilized in the studies presented. In cases where methods were conducted by other researchers, it will be explicitly mentioned at the beginning of the corresponding subchapters.

6.1 Materials/Tools Used

6.1.1 List of chemicals

Ar gas 99.999 %	Air Liquide (Germany)
HClO ₄	Sigma-Aldrich (Germany)
KCl	VWR (Germany)
KOH	Carl Roth (Germany)
O ₂	Air Liquide (Germany)

6.1.2 List of materials

Aluminium tape	3M (Germany)
Blu tack	Bostik (Germany)
Capillaries, quartz double-barrel with filaments	Friedrich & Dimmock (USA)
Carbon tape	Plano (Germany)
Copper wire	Conrad Electronics (Germany)
Copper tape	Conrad Electronics (Germany)
Parafilm	Pechiney Plastic Packaging (USA)
Platinum mesh electrode	Goodfellow (Germany)
Platinum wire (0.22 mm)	Goodfellow (Germany)
Soldering tin	Stannol (Germany)
Silver wire	Goodfellow (Germany)

6.1.3 List of devices

Laser puller (S-2000)	Sutter (USA)
MicroFill (MF34G-5)	World Precision Instruments
Microscope (BX41)	Olympus (Germany)
Multimeter (UT70A)	Uni-T, Reichelt (Germany)
pH meter (CP-411)	Elmetron, PCE Group (Germany)
Power supply for AgCl deposition (DC Power Supply)	Voltcraft, Conrad (Germany)
SEM (Quanta 3D FEG ESEM)	FEI, Thermo Fisher Scientific (Germany)
Soldering station (LF-3200)	XYtronic, Reichelt (Germany)
Water purification system	SG Water (Germany)

6.1.4 List of software

LabVIEW (2017, with FPGA and Real-Time modules)	National Instruments (Germany)
Origin (2016-2018b)	Origin Lab Corp. (USA)
TDMS-Extract	Dr. Tsvetan Tarnev. Analytical Chemistry, RUB (Germany)
WEC-SPM (modified)	Prof. P. R. Unwin, University of Warwick (United Kingdom)
MATLAB (2020a – 2022a)	MathWorks (USA)

6.2 Sample and probe fabrication and preparation

6.2.1 Sputtering process

The sputtering processes were carried out by Sabrina Baha and Alan Savan from the Chair of Materials Discovery and Interfaces at the RUB lead by Prof. Dr. Alfred Ludwig.

Thin-film material libraries were fabricated using a commercial sputter system (CMS 600/400 LIN, DCA Instruments) by co-sputtering from five confocal sources. The substrates used were polished single crystal, (100) orientation Si wafers (Siegert Wafer, Germany) with a diameter of 100 mm, which were positioned at the confocal sputtering position. To prevent any potential reactions with the substrate, a 500 nm thick wet thermal SiO₂ layer was deposited as a barrier.

For the fabrication of (TiNi)-Cu-Hf-Pd-Zr:

The sputter targets used were single elements, including Cu (99.99%), Hf (99.95%), Pd (99.99%), Zr (>99.2%), and a custom-made TiNi₄₆₉ (FHR). The substrates were loaded into the deposition chamber through a loadlock system. The chamber had a base vacuum of 7×10^{-7} Pa, and the deposition was carried out at a pressure of 0.67 Pa in pure Ar (99.9999%) at room temperature (25 °C) without intentional heating. The power applied to each cathode was adjusted to achieve a desired composition, resulting in a centerpoint composition of Ti 14 at.%, Ni 17 at.%, Cu 16 at.%, Zr 21 at.%, Pd 17 at.%, and Hf 15 at.%. The total deposition rate was maintained at 0.1 nm/s.

For the fabrication of Co-Cr-Fe-Mo-Ni:

The sputter targets used were single elements, including Co (99.99%), Cr (99.95%), Fe (99.99%), Mo (99.95%) and Ni (99.995%). The chamber had a base vacuum of $< 3.6 \times 10^{-7}$ Pa, and the deposition was carried out at a pressure of 0.67 Pa in pure Ar (99.9999%) at room temperature (25 °C) without intentional heating. The power applied to each cathode was adjusted to achieve a desired composition, resulting in following centerpoints: ML1: Co 20 at.%, Cr 24 at.%, Fe 14 at.%, Mo 21 at.%, Ni 21 at.%; ML2: Co 43 at.%, Cr 12 at.%, Fe 31 at.%, Mo 5 at.%; Ni 9 at.%; ML3: Co 36 at.%, Cr 16 at.%, Fe 20 at.%, Mo 8 at.%, Ni 20 at.%. The average of the layer thickness of each ML is approx. 150 nm.

6.2.2 CVD process

The CVD and Transfer processes were carried out by Dr. Lukas Madauß from the Faculty of Physics (AG Schleberger) of the UDE.

The CVD process involves the utilization of a three-zone tube furnace. This furnace comprises three heating zones where sulfur (S) and droplets of ammonium heptamolybdate (AHM) solution are independently heated to their respective evaporation temperatures. To facilitate faster cooling of the samples and precise placement within the tube, the furnace can be opened. At the left end of the tube, air is introduced through a metering valve to heat the tube furnace from the outside. In a typical CVD process, argon gas is introduced through this end. The flow of argon is regulated by a mass flow controller, which is controlled by a computer. At the right end

of the tube, the argon gas and any remaining carrier gas residues are expelled through a connecting piece in the exhaust air.

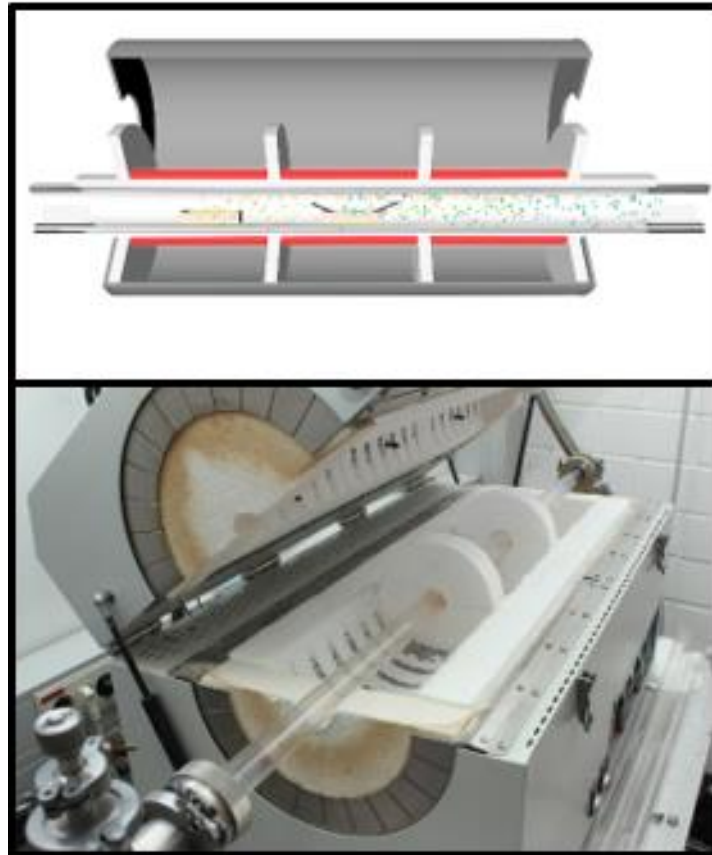


Figure 44: Three phase tube-furnace used for CVD process.(Adapted with permission of the work group Schleberger (Faculty of Physics, UDE) Image of the furnace were provided by Dr. Andreas Reichert, while the C4D illustrations were created by Dr. Lukas Madauß.)

6.2.3 Transfer of MoS₂

Initially, the MoS₂ samples, prepared through the CVD process, are cut into smaller pieces measuring approximately 1 x 0.5 cm. These substrate pieces are then placed with the MoS₂ side facing downwards on a watch glass, ensuring that only the corners of the substrates make contact with the glass. The back of the substrates is cut to an appropriate size of around 0.5 cm². To eliminate any dust or dirt particles adhering to the substrates, a nitrogen gun is employed for cleaning.

Next, a liquid PMMA is applied to coat the substrates using a spin coater. In order for the photoresist to dry, the coated substrates are subjected to a hot plate set at 100 °C for a duration of 5 minutes. To remove the PMMA present on the back of the substrate, the substrates are placed on wipes soaked in acetone. Subsequently, the substrates are positioned with the MoS₂ side facing upwards on the surface of a KOH solution, where they float due to the surface tension of the solution. The substrates remain in

the solution until the PMMA dissolves, thereby detaching from the SiO₂ substrate while still holding the MoS₂.

Once the PMMA has separated from the substrate, it floats on the solution's surface. The PMMA/MoS₂ stack is then transferred to a water container with minimal KOH solution content, and excess alkaline solution is removed by gently agitating the stack using a spoon. This washing process involves changing the water 2-3 times and allowing the samples to soak for several hours. After washing, a glassy carbon substrate that has been cleaned in an ultrasonic bath is placed in a watch glass containing water, allowing the PMMA/MoS₂ stack to gradually adhere to the glassy carbon surface. Finally, the PMMA is dissolved in acetone, and the sample undergoes additional cleaning by immersion in a bath of isopropanol.

6.3 Sample and probe characterization

6.3.1 Scanning electron microscopy

SEM images were captured using a Quanta 3D FEG microscope (FEI, Thermo Fisher Scientific, Germany) at either 20 or 30 kV, employing a spot size of 4.5 and maintaining a working distance of approximately 10 mm under high vacuum conditions. The samples were affixed to aluminum stubs using conductive carbon tape to ensure reliable electrical contact.

The SEM was utilized to examine the dimensions of the openings at the capillary tips and to observe any remaining electrolyte residuals after conducting a SECCM scan on a scanned MoS₂ sample.

6.3.2 Preparation of Ag/AgCl QRCE

A 0.25 mm thick silver wire was subjected to roughening by using abrasive paper and then submerged in a 3 M KCl solution. The wire was subjected to an applied potential of 5 V vs. a circular platinum electrode mounted around the silver wire for a duration of 2 minutes, followed by an applied potential of 10 V for ten minutes. After the electrochemical treatment, the wire was thoroughly washed with water.

6.3.3 Preparation of SECCM probes (capillaries)

The capillaries used for the experiments were cleaned externally with acetone to ensure uniform heating and then inserted into the CO₂-laser puller (P-2000, Sutter Instruments). Various capillaries and programs were employed for the pulling process.

For the initial measurements on MoS₂ (Chapter 4.2.1), quartz theta capillaries (double barrel) with filaments (WAR-QTF-120-90, Friedrich & Dimmock) having dimensions of 1.2 mm outer diameter, 0.9 mm inner diameter, and 10 cm length were utilized. The following two-line pulling procedure was implemented and was leading to a tip size of approximately 750 nm:

Line 1: HEAT 800, FIL 4, VEL 40, DEL 130, PUL 0

Line 2: HEAT 650, FIL 3, VEL 30, DEL 130, PUL 90

Single-barrel SECCM capillaries were fabricated from quartz filamented capillaries (ZQF-120-90-10, Science Products) for all other experiments. Different pulling

procedures (one-line pulling procedures) were used to achieve capillaries with various tip sizes:

$d \approx 50$ nm HEAT 790, FIL 4, VEL 40, DEL 130, PUL 110

$d \approx 150$ nm HEAT 780, FIL 4, VEL 40, DEL 130, PUL 110

$d \approx 300$ nm HEAT 760, FIL 4, VEL 40, DEL 130, PUL 100

$d \approx 600$ nm HEAT 730, FIL 4, VEL 40, DEL 130, PUL 100

6.3.4 Filling of the capillaries

The capillaries were filled using a MicroFill needle, and any air bubbles in the thin part of the tip were removed by either flicking the capillary or applying air pressure. Other possibilities of removing air bubbles from the tip was gently heating with a heating plate or cooling them down.

6.3.5 Checking the OCP of the QRCE

Before each SECCM measurement, the open circuit potential of the quasi-reference counter electrode (QRCE) was determined. To do this, the capillary filled with electrolyte and the QRCE were inserted into a vessel filled with electrolyte. A commercial reference electrode (Double junction Ag/AgCl/3 M KCl, Metrohm) was also inserted into the vessel. Using a digital multimeter, the potential difference between the QRCE and the reference electrode was measured. This potential value was later used to convert the applied potential during SECCM measurements to the reversible hydrogen electrode (RHE) scale using following equation:

$$E_{RHE}[V] = E_{Ag|AgCl|3MKCl} + 0.210 + 0.059 \times pH + OCP \quad eq.18$$

6.4 SDC experiments

6.4.1 SDC experiments on (TiNi) -Cu-Hf-Pd-Zr

The electrochemical analysis of the material libraries (MLs) was conducted using a scanning droplet cell, which automatically evaluated 342 measurement areas (MAs) on each ML. The formation of the electrochemical cell occurred when the droplet cell made contact with the ML, ensuring proper contact by monitoring the applied pressure force. The electrochemical cell comprised three electrodes: the ML served as the working electrode, an Ag|AgCl|3M KCl reference electrode, and a Pt wire as the counter electrode. The electrolyte used was a 0.1 M KOH solution, which was automatically replaced before evaluating each MA. In the case of the oxygen reduction reaction (ORR), linear sweep voltammetry (LSV) experiments were conducted over the potential range from 1 V to 200 mV vs. the reversible hydrogen electrode (RHE), with a scan rate of 10 mV·s⁻¹. For the hydrogen evolution reaction (HER), LSV measurements were performed in the potential range from 0 V to -700 mV vs. RHE. For data analysis, the conversion from the Ag|AgCl|3M KCl scale to the reversible hydrogen electrode (RHE) scale was performed using the given equation:

$$E_{RHE}[V] = E_{Ag|AgCl|3MKCl} + 0.210 + 0.059 \times pH \quad eq.19$$

where $E_{Ag|AgCl|3MKCl}$ is the applied potential vs the reference electrode (Ag|AgCl|3 M KCl), 0.210 V is the standard potential of the Ag|AgCl|3 M KCl at 25 °C, while 0.059 V is the result of $(RT)/(nF)$, where R is the universal gas constant, T the temperature at 25 °C, F the Faraday constant and n equals 1.

6.4.2 SDC experiments on Co-Cr-Fe-Mo-Ni

Same procedure as in 6.4.1 is applied for the HER measurements.

6.5 SECCM experiments

6.5.1 Initial SECCM setup

The SECCM system how it was used for the initial experiments on MoS₂ (chapter 4.2.1) consists of several components, including a precise positioning system, fast current acquisition devices, and a system to oscillate the capillary and detect the resulting AC signal. For high-resolution imaging with small pipette diameters, a piezo-based positioning system is employed, using a piezo cube (P-611.3S nanocube, PhysikInstrumente) and an analogue amplifier (E-664, Physik Instrumente). The sample can be moved laterally in x-y directions and vertically in the z direction using the piezo cube. Additionally, a separate piezo rod (PSt 150/5/60 VS10, Piezomechanik) with an amplifier from Piezomechanik (LE150/100/EBW) mounted on the capillary holder can be used to oscillate the capillary with a small amplitude to create the AC signal via changing of the meniscus shape.

The AC perturbation signal for piezo vibration is generated by the internal oscillator of a lock-in amplifier (7280 DSP, SignalRecovery). A coarse positioning system is employed to bring the tip close to the investigated surface and within the overall travel range of the piezo actuators (100 μm for the piezo cube). Prepositioning can be by computer-controlled devices, facilitated by a microscope camera (DMK 21AU04, The Imaging Source) with external lighting from a cold light source (KL1500 LCD, Schott).

To isolate the SECCM from external noise, the positioning system and the electrochemical cell are located in a Faraday cage equipped with a thermal isolation panel (Vaku-Isotherm) to prevent temperature drift during measurements. The setup is built on a vibration damping table (RS 2000, Newport) set on four S-2000 stabilizers (Newport) to decouple it from building oscillations. Data acquisition and instrument control are achieved by an FPGA card (PCIe-7852R, National Instruments) connected to a computer running a modified version of LabVIEW software (WEC-SPM) provided by the University of Warwick. The FPGA card enables fast data acquisition and control of the tip position and electrode potentials through embedded instructions. Two commercial current amplifiers, VA-10 and ELC-03XS from NPI, are used for the AC double barrel approach. The first amplifier measures the current between the two QRCEs in the barrels of the capillary, while the second measures the current between

one of the QRCEs and the sample. The measured currents are forwarded to the lock-in amplifier for further analysis.

6.5.2 SECCM setup optimization

As described in chapter 4.2.2, the current amplifier in the SECCM setup was replaced with the FEMTO DLPCA-200 to optimize the signal to noise ratio. This change also involved transitioning from the double barrel approach to SECCM experiments with single barrels. Consequently, devices used for the double barrel approach, such as the lock-in amplifier, rod piezo, and headstage of the other current amplifier, were removed from the setup. Additionally, the piezo cube for fine movement was fixed upside down, and the probe was fixed to it. The relative movement between the sample and the probe is the critical factor, and it does not matter which part is moving. The details of this setup change will be discussed further in chapter 6.5.5.

6.5.3 SECCM experiments on MoS₂

A nanopipette with an opening diameter of approximately 55 nm was used in the SECCM experiments. The nanopipettes were filled with 0.1 M HClO₄ using a MicroFil syringe, and a Ag/AgCl wire served as the quasi-reference counter electrode (QRCE) during the SECCM measurements. The Ag/AgCl QRCE was prepared by immersing a polished Ag wire (diameter: 0.125 mm, Goodfellow, 99.99%) in a 3 M KCl solution and applying a potential of +5 V versus a Pt electrode for 10 minutes. The open-circuit potential of the QRCE was measured before and after the SECCM measurement using a Ag/AgCl/3 M KCl reference electrode. The SECCM workstation used a sample holder supporting the GC/MoS₂ sample mounted on a 3-axis step motor microscrew system (Owis) controlled by an L-Step PCIe controller card (Lang) for coarse positioning. The filled single-barrel capillary with the QRCE was mounted on a 3-axis piezo nanopositioner (P-611.3S nanocube, Physik Instrumente) for fine positioning of the pipette tip above the surface, using an analog amplifier (E-664, Physik Instrumente). In the electrochemical experiments, the MoS₂ sample transferred on the GC served as the working electrode (WE), while the Ag/AgCl wire acted as the QRCE in a 2-electrode system. The electrochemical cell was formed when the MoS₂/GC made contact with the hanging drop of the filled nanopipette. The surface contact was detected by measuring the current between the WE and the QRCE, stopping the approach immediately after a current threshold of 2 pA was recorded using a low-noise current

amplifier (DLPCA-200, FEMTO). The size of the formed electrochemical cell was estimated based on the size of the nanopipette opening. A hopping-mode measurement protocol was employed for spatial resolution, measuring 61×81 individual spots with a distance of 500 nm, resulting in a map of 30×40 μm.

6.5.4 SECCM experiments on stress chips

Due to the weight of approximately 1 kg of the holder for the stress chip holder, the piezo cube is unable to support such a heavy load. When excessive weight is placed on the piezo, it starts to oscillate, leading to a loss of precision in measurements. As a result, it is crucial to avoid exceeding the piezo's weight capacity to ensure accurate and reliable measurements.

Same procedure as in 6.5.3 is applied for the HER measurements.

7. List of contributions

7.1 First author publications

- O. A. Krysiak[#], S. Schumacher[#], A. Savan, W. Schuhmann*, A. Ludwig*, C. Andronescu* Searching novel complex solid solution electrocatalysts in unconventional element combinations, NanoResearch, 2022, 15(6):4780-4784
- S. Schumacher, S. Baha, A. Savan, C. Andronescu*, A. Ludwig*, High-throughput discovery of hydrogen evolution electrocatalysts in the complex solid solution system Co-Cr-Fe-Mo-Ni, Journal of Material Chemistry A, 2022, 10, 9981-9987
- S. Schumacher, L. Madauß, Y. Liebsch, E. Batsa Tetteh, S. Varhade, W. Schuhmann, M. Schleberger, C. Andronescu*, Revealing the heterogeneity of large-area MoS₂ layers in the electrocatalytic hydrogen evolution reaction, ChemElectroChem, 2022, 9, e202200586

7.2 Co-author publications

- E. Batsa Tetteh, L. Banko, O. A. Krysiak, T. Löffler, B. Xiao, S. Varhade, S. Schumacher, A. Savan, C. Andronescu, A. Ludwig, W. Schuhmann, Zooming-in - Visualization of active site heterogeneity in high entropy alloy electrocatalysts using scanning electrochemical cell microscopy, Electrochemical Science Advances, 2021, 2, e2100105 doi.org/10.1002/elsa.202100105 [Titel anhand dieser DOI in Citavi-Projekt übernehmen]
- E. Batsa Tetteh, T. Löffler, T. Tarnev, T. Quast, P. Wilde, H. Barikke Aiyappa, S. Schumacher, C. Andronescu, R. D. Tilley, X. Chen, W. Schuhmann, Calibrating SECCM measurements by means of a nanoelectrode ruler. The intrinsic oxygen reduction activity of PtNi catalyst nanoparticles, NanoResearch, 2022, 15(2) 1564-1569.
- S. Varhade, E. Batsa Tetteh, S. Saddeler, S. Schumacher, H. Barikke Aiyappa, S. Schulz, C. Andronescu,* W. Schuhmann* Crystal plane-related oxygen evolution activity of single hexagonal Co₃O₄ spinel particles, Chemistry – A European Journal, 2023, 29, e202203474

- S. Varhade, G. Meloni, E. Batsa Tetteh, M. Kim, S. Schumacher, T. Quast, C. Andronescu*, P. Unwin*, W. Schuhmann*, Elucidation of alkaline electrolyte-surface interaction in SECCM using a pH-independent redox probe, *Electrochimica Acta*, 2023, 460, 142548

8. References

- (1) Momirlan, M.; Veziroglu, T. The properties of hydrogen as fuel tomorrow in sustainable energy system for a cleaner planet. *International Journal of Hydrogen Energy* **2005**, *30* (7), 795–802. DOI: 10.1016/j.ijhydene.2004.10.011.
- (2) Hosseini, S. E.; Wahid, M. A. Hydrogen production from renewable and sustainable energy resources: Promising green energy carrier for clean development. *Renewable and Sustainable Energy Reviews* **2016**, *57*, 850–866. DOI: 10.1016/j.rser.2015.12.112.
- (3) Edwards, P. P.; Kuznetsov, V. L.; David, W.; Brandon, N. P. Hydrogen and fuel cells: Towards a sustainable energy future. *Energy Policy* **2008**, *36* (12), 4356–4362. DOI: 10.1016/j.enpol.2008.09.036.
- (4) Pickard, W. F.; Shen, A. Q.; Hansing, N. J. Parking the power: Strategies and physical limitations for bulk energy storage in supply–demand matching on a grid whose input power is provided by intermittent sources. *Renewable and Sustainable Energy Reviews* **2009**, *13* (8), 1934–1945. DOI: 10.1016/j.rser.2009.03.002.
- (5) Abdin, Z.; Webb, C. J.; Gray, E. RETRACTED: Solar hydrogen hybrid energy systems for off-grid electricity supply: A critical review. *Renewable and Sustainable Energy Reviews* **2015**, *52*, 1791–1808. DOI: 10.1016/j.rser.2015.08.011.
- (6) Inocêncio, C. V. M.; Holade, Y.; Morais, C.; Kokoh, K. B.; Napporn, T. W. Electrochemical hydrogen generation technology: Challenges in electrodes materials for a sustainable energy. *Electrochemical Science Adv* **2022**. DOI: 10.1002/elsa.202100206.
- (7) Hansen, J. N.; Prats, H.; Toudahl, K. K.; Mørch Secher, N.; Chan, K.; Kibsgaard, J.; Chorkendorff, I. Is There Anything Better than Pt for HER? *ACS energy letters* **2021**, *6* (4), 1175–1180. DOI: 10.1021/acscenergylett.1c00246. Published Online: Mar. 19, 2021.
- (8) Jiang, P.; Liu, Q.; Liang, Y.; Tian, J.; Asiri, A. M.; Sun, X. A Cost-Effective 3D Hydrogen Evolution Cathode with High Catalytic Activity: FeP Nanowire Array as the Active Phase. *Angew. Chem.* **2014**, *126* (47), 13069–13073. DOI: 10.1002/ange.201406848.
- (9) Liang, Y.; Liu, Q.; Asiri, A. M.; Sun, X.; Luo, Y. Self-Supported FeP Nanorod Arrays: A Cost-Effective 3D Hydrogen Evolution Cathode with High Catalytic Activity. *ACS Catal.* **2014**, *4* (11), 4065–4069. DOI: 10.1021/cs501106g.
- (10) Wang, S.; Wang, J.; Zhu, M.; Bao, X.; Xiao, B.; Su, D.; Li, H.; Wang, Y. Molybdenum-Carbide-Modified Nitrogen-Doped Carbon Vesicle Encapsulating Nickel Nanoparticles: A Highly Efficient, Low-Cost Catalyst for Hydrogen Evolution Reaction. *J. Am. Chem. Soc.* **2015**, *137* (50), 15753–15759. DOI: 10.1021/jacs.5b07924. Published Online: Dec. 15, 2015.
- (11) Löffler, T.; Savan, A.; Garzón-Manjón, A.; Meischein, M.; Scheu, C.; Ludwig, A.; Schuhmann, W. Toward a Paradigm Shift in Electrocatalysis Using Complex Solid Solution Nanoparticles. *ACS Energy Lett.* **2019**, *4* (5), 1206–1214. DOI: 10.1021/acscenergylett.9b00531.
- (12) Batchelor, T. A. A.; Löffler, T.; Xiao, B.; Krysiak, O. A.; Strotkötter, V.; Pedersen, J. K.; Clausen, C. M.; Savan, A.; Li, Y.; Schuhmann, W.; Rossmeisl, J.; Ludwig, A. Complex-Solid-Solution Electrocatalyst Discovery by Computational Prediction and High-Throughput Experimentation*. *Angew. Chem. Int. Ed. Engl.* **2021**, *60* (13), 6932–6937. DOI: 10.1002/anie.202014374. Published Online: Feb. 10, 2021.
- (13) Masa, J.; Andronesco, C.; Schuhmann, W. Electrocatalysis as the Nexus for Sustainable Renewable Energy: The Gordian Knot of Activity, Stability, and Selectivity. *Angew. Chem. Int. Ed. Engl.* **2020**, *59* (36), 15298–15312. DOI: 10.1002/anie.202007672. Published Online: Aug. 18, 2020.
- (14) Masa, J.; Schuhmann, W. Breaking scaling relations in electrocatalysis. *J Solid State Electrochem* **2020**, *24* (9), 2181–2182. DOI: 10.1007/s10008-020-04757-1.
- (15) Unwin, P. Concluding remarks: next generation nanoelectrochemistry - next generation nanoelectrochemists. *Faraday Discuss.* **2022**, *233* (0), 374–391. DOI: 10.1039/d2fd00020b. Published Online: Apr. 5, 2022.

- (16) Hattrick-Simpers, J.; Wen, C.; Lauterbach, J. The Materials Super Highway: Integrating High-Throughput Experimentation into Mapping the Catalysis Materials Genome. *Catal Lett* **2015**, *145* (1), 290–298. DOI: 10.1007/s10562-014-1442-y.
- (17) Allen, C. L.; Leitch, D. C.; Anson, M. S.; Zajac, M. A. The power and accessibility of high-throughput methods for catalysis research. *Nat Catal* **2019**, *2* (1), 2–4. DOI: 10.1038/s41929-018-0220-4.
- (18) Hagemeyer, A.; Volpe, A. *Modern Applications of High Throughput R&D in Heterogeneous Catalysis*; BENTHAM SCIENCE PUBLISHERS, 2014. DOI: 10.2174/97816080587231140101.
- (19) Sun, X.; Xu, K.; Fleischer, C.; Liu, X.; Grandcolas, M.; Strandbakke, R.; Bjørheim, T.; Norby, T.; Chatzidakis, A. Earth-Abundant Electrocatalysts in Proton Exchange Membrane Electrolyzers. *Catalysts* **2018**, *8* (12), 657. DOI: 10.3390/catal8120657.
- (20) David, M.; Ocampo-Martínez, C.; Sánchez-Peña, R. Advances in alkaline water electrolyzers: A review. *J. Energy Storage* **2019**, *23*, 392–403. DOI: 10.1016/j.est.2019.03.001.
- (21) Pandiyan, A.; Uthayakumar, A.; Subrayan, R.; Cha, S. W.; Krishna Moorthy, S. B. Review of solid oxide electrolysis cells: a clean energy strategy for hydrogen generation. *Nanomater. Energy* **2019**, *8* (1), 2–22. DOI: 10.1680/jnaen.18.00009.
- (22) Smolinka, T. FUELS – HYDROGEN PRODUCTION | Water Electrolysis. In *Encyclopedia of Electrochemical Power Sources*; Elsevier, 2009; pp 394–413. DOI: 10.1016/B978-044452745-5.00315-4.
- (23) Liang, Q.; Brocks, G.; Bieberle-Hütter, A. Oxygen evolution reaction (OER) mechanism under alkaline and acidic conditions. *J. Phys. Energy* **2021**, *3* (2), 26001. DOI: 10.1088/2515-7655/abdc85.
- (24) Rossmesl, J.; Qu, Z.-W.; Zhu, H.; Kroes, G.-J.; Nørskov, J. K. Electrolysis of water on oxide surfaces. *J. Electroanal. Chem.* **2007**, *607* (1-2), 83–89. DOI: 10.1016/j.jelechem.2006.11.008.
- (25) Lasia, A. Mechanism and kinetics of the hydrogen evolution reaction. *International Journal of Hydrogen Energy* **2019**, *44* (36), 19484–19518. DOI: 10.1016/j.ijhydene.2019.05.183.
- (26) Zheng, Y.; Jiao, Y.; Vasileff, A.; Qiao, S.-Z. The Hydrogen Evolution Reaction in Alkaline Solution: From Theory, Single Crystal Models, to Practical Electrocatalysts. *Angew. Chem. Int. Ed. Engl.* **2018**, *57* (26), 7568–7579. DOI: 10.1002/anie.201710556.
- (27) Dubouis, N.; Grimaud, A. The hydrogen evolution reaction: from material to interfacial descriptors. *Chem. Sci.* **2019**, *10* (40), 9165–9181. DOI: 10.1039/C9SC03831K.
- (28) Hamann, C. H.; Hamnett, A.; Vielstich, W. *Electrochemistry*, 2nd completely rev. and updated ed.; Wiley-VCH; [Chichester : John Wiley, 2007.
- (29) Laursen, A. B.; Varela, A. S.; Dionigi, F.; Fanchiu, H.; Miller, C.; Trinhammer, O. L.; Rossmesl, J.; Dahl, S. Electrochemical Hydrogen Evolution: Sabatier’s Principle and the Volcano Plot. *J. Chem. Educ.* **2012**, *89* (12), 1595–1599. DOI: 10.1021/ed200818t.
- (30) Li, Y.; Wang, H.; Xie, L.; Liang, Y.; Hong, G.; Dai, H. MoS₂ nanoparticles grown on graphene: an advanced catalyst for the hydrogen evolution reaction. *J. Am. Chem. Soc.* **2011**, *133* (19), 7296–7299. DOI: 10.1021/ja201269b. Published Online: Apr. 21, 2011.
- (31) Shinagawa, T.; Garcia-Esparza, A. T.; Takanabe, K. Insight on Tafel slopes from a microkinetic analysis of aqueous electrocatalysis for energy conversion. *Sci. Rep.* **2015**, *5*, 13801. DOI: 10.1038/srep13801. Published Online: Sep. 8, 2015.
- (32) Ioroi, T.; Siroma, Z.; Yamazaki, S.; Yasuda, K. Electrocatalysts for PEM Fuel Cells. *Adv. Energy Mater.* **2019**, *9* (23), 1801284. DOI: 10.1002/aenm.201801284.
- (33) Fu, J.; Cano, Z. P.; Park, M. G.; Yu, A.; Fowler, M.; Chen, Z. Electrically Rechargeable Zinc-Air Batteries: Progress, Challenges, and Perspectives. *Adv. Mater.* **2017**, *29* (7). DOI: 10.1002/adma.201604685. Published Online: Nov. 28, 2016.
- (34) Li, Y.; Dai, H. Recent advances in zinc-air batteries. *Chem. Soc. Rev.* **2014**, *43* (15), 5257–5275. DOI: 10.1039/C4CS00015C.

- (35) Debe, M. K. Electrocatalyst approaches and challenges for automotive fuel cells. *Nature* **2012**, *486* (7401), 43–51. DOI: 10.1038/nature11115. Published Online: Jun. 6, 2012.
- (36) Schmidt, T. J.; Paulus, U. A.; Gasteiger, H. A.; Behm, R. J. The oxygen reduction reaction on a Pt/carbon fuel cell catalyst in the presence of chloride anions. *J. Electroanal. Chem.* **2001**, *508* (1-2), 41–47. DOI: 10.1016/S0022-0728(01)00499-5.
- (37) Hansen, H. A.; Viswanathan, V.; Nørskov, J. K. Unifying Kinetic and Thermodynamic Analysis of 2 e⁻ and 4 e⁻ Reduction of Oxygen on Metal Surfaces. *J. Phys. Chem. C* **2014**, *118* (13), 6706–6718. DOI: 10.1021/jp4100608.
- (38) Holton, O. T.; Stevenson, J. W. The Role of Platinum in Proton Exchange Membrane Fuel Cells. *platin met. rev.* **2013**, *57* (4), 259–271. DOI: 10.1595/147106713X671222.
- (39) Song, C.; Zhang, J. Electrocatalytic Oxygen Reduction Reaction. In *PEM Fuel Cell Electrocatalysts and Catalyst Layers*; Zhang, J., Ed.; Springer London, 2008; pp 89–134. DOI: 10.1007/978-1-84800-936-3_2.
- (40) Ma, R.; Lin, G.; Zhou, Y.; Liu, Q.; Zhang, T.; Shan, G.; Yang, M.; Wang, J. A review of oxygen reduction mechanisms for metal-free carbon-based electrocatalysts. *npj Comput. Mater.* **2019**, *5* (1). DOI: 10.1038/s41524-019-0210-3.
- (41) Guo, S.; Sun, S. FePt nanoparticles assembled on graphene as enhanced catalyst for oxygen reduction reaction. *J. Am. Chem. Soc.* **2012**, *134* (5), 2492–2495. DOI: 10.1021/ja2104334. Published Online: Jan. 26, 2012.
- (42) Jaouen, F.; Proietti, E.; Lefèvre, M.; Chenitz, R.; Dodelet, J.-P.; Wu, G.; Chung, H. T.; Johnston, C. M.; Zelenay, P. Recent advances in non-precious metal catalysis for oxygen-reduction reaction in polymer electrolyte fuelcells. *Energy Environ. Sci.* **2011**, *4* (1), 114–130. DOI: 10.1039/C0EE00011F.
- (43) Guerrero Moreno, N.; Cisneros Molina, M.; Gervasio, D.; Pérez Robles, J. F. Approaches to polymer electrolyte membrane fuel cells (PEMFCs) and their cost. *Renewable and Sustainable Energy Reviews* **2015**, *52*, 897–906. DOI: 10.1016/j.rser.2015.07.157.
- (44) Chattot, R.; Martens, I.; Scohy, M.; Herranz, J.; Drnec, J.; Maillard, F.; Dubau, L. Disclosing Pt-Bimetallic Alloy Nanoparticle Surface Lattice Distortion with Electrochemical Probes. *ACS Energy Lett.* **2020**, *5* (1), 162–169. DOI: 10.1021/acseenergylett.9b02287.
- (45) Stamenkovic, V. R.; Mun, B. S.; Arenz, M.; Mayrhofer, K. J. J.; Lucas, C. A.; Wang, G.; Ross, P. N.; Markovic, N. M. Trends in electrocatalysis on extended and nanoscale Pt-bimetallic alloy surfaces. *Nat. Mater.* **2007**, *6* (3), 241–247. DOI: 10.1038/nmat1840. Published Online: Feb. 18, 2007.
- (46) Huang, X.; Zhao, Z.; Cao, L.; Chen, Y.; Zhu, E.; Lin, Z.; Li, M.; Yan, A.; Zettl, A.; Wang, Y. M.; Duan, X.; Mueller, T.; Huang, Y. ELECTROCHEMISTRY. High-performance transition metal-doped Pt₃Ni octahedra for oxygen reduction reaction. *Science* **2015**, *348* (6240), 1230–1234. DOI: 10.1126/science.aaa8765. Published Online: Nov. 6, 2015.
- (47) Bu, L.; Zhang, N.; Guo, S.; Zhang, X.; Li, J.; Yao, J.; Wu, T.; Lu, G.; Ma, J.-Y.; Su, D.; Huang, X. Biaxially strained PtPb/Pt core/shell nanoplate boosts oxygen reduction catalysis. *Science* **2016**, *354* (6318), 1410–1414. DOI: 10.1126/science.aah6133.
- (48) Yano, H.; Arima, I.; Watanabe, M.; Iiyama, A.; Uchida, H. Oxygen Reduction Activity and Durability of Ordered and Disordered Pt₃Co Alloy Nanoparticle Catalysts at Practical Temperatures of Polymer Electrolyte Fuel Cells. *J. Electrochem. Soc.* **2017**, *164* (9), F966-F972. DOI: 10.1149/2.1141709jes.
- (49) Xie, P.; Yao, Y.; Huang, Z.; Liu, Z.; Zhang, J.; Li, T.; Wang, G.; Shahbazian-Yassar, R.; Hu, L.; Wang, C. Highly efficient decomposition of ammonia using high-entropy alloy catalysts. *Nat. Commun.* **2019**, *10* (1), 4011. DOI: 10.1038/s41467-019-11848-9. Published Online: May. 9, 2019.
- (50) Wang, H.; Wei, R.; Li, X.; Ma, X.; Hao, X.; Guan, G. Nanostructured amorphous Fe₂₉Co₂₇Ni₂₃Si₉B₁₂ high-entropy-alloy: an efficient electrocatalyst for oxygen evolution reaction. *J. Mater. Sci. Technol.* **2021**, *68*, 191–198. DOI: 10.1016/j.jmst.2020.06.045.

- (51) Pedersen, J. K.; Batchelor, T. A. A.; Bagger, A.; Rossmeisl, J. High-Entropy Alloys as Catalysts for the CO₂ and CO Reduction Reactions. *ACS Catal.* **2020**, *10* (3), 2169–2176. DOI: 10.1021/acscatal.9b04343.
- (52) Jin, Z.; Lv, J.; Jia, H.; Liu, W.; Li, H.; Chen, Z.; Lin, X.; Xie, G.; Liu, X.; Sun, S.; Qiu, H.-J. Nanoporous Al-Ni-Co-Ir-Mo High-Entropy Alloy for Record-High Water Splitting Activity in Acidic Environments. *Small (Weinheim an der Bergstrasse, Germany)* **2019**, *15* (47), e1904180. DOI: 10.1002/smll.201904180. Published Online: Sep. 10, 2019.
- (53) Pickering, E. J.; Jones, N. G. High-entropy alloys: a critical assessment of their founding principles and future prospects. *Int. Mater. Rev.* **2016**, *61* (3), 183–202. DOI: 10.1080/09506608.2016.1180020.
- (54) Löffler, T.; Ludwig, A.; Rossmeisl, J.; Schuhmann, W. What Makes High-Entropy Alloys Exceptional Electrocatalysts? *Angew. Chem. Int. Ed. Engl.* **2021**, *60* (52), 26894–26903. DOI: 10.1002/anie.202109212. Published Online: Jan. 10, 2021.
- (55) Zhang, G.; Ming, K.; Kang, J.; Huang, Q.; Zhang, Z.; Zheng, X.; Bi, X. High entropy alloy as a highly active and stable electrocatalyst for hydrogen evolution reaction. *Electrochim. Acta* **2018**, *279*, 19–23. DOI: 10.1016/j.electacta.2018.05.035.
- (56) Liu, M.; Zhang, Z.; Okejiri, F.; Yang, S.; Zhou, S.; Dai, S. Entropy-Maximized Synthesis of Multimetallic Nanoparticle Catalysts via a Ultrasonication-Assisted Wet Chemistry Method under Ambient Conditions. *Adv. Mater. Interfaces* **2019**, *6* (7), 1900015. DOI: 10.1002/admi.201900015.
- (57) Yao, R.-Q.; Zhou, Y.-T.; Shi, H.; Wan, W.-B.; Zhang, Q.-H.; Gu, L.; Zhu, Y.-F.; Wen, Z.; Lang, X.-Y.; Jiang, Q. Nanoporous Surface High-Entropy Alloys as Highly Efficient Multisite Electrocatalysts for Nonacidic Hydrogen Evolution Reaction. *Adv. Funct. Mater.* **2020**, 2009613. DOI: 10.1002/adfm.202009613.
- (58) Ma, P.; Zhao, M.; Zhang, L.; Wang, H.; Gu, J.; Sun, Y.; Ji, W.; Fu, Z. Self-supported high-entropy alloy electrocatalyst for highly efficient H₂ evolution in acid condition. *J. Mater. Chem. A* **2020**, *8* (4), 736–742. DOI: 10.1016/j.jmat.2020.06.001.
- (59) Feng, G.; Ning, F.; Song, J.; Shang, H.; Zhang, K.; Ding, Z.; Gao, P.; Chu, W.; Xia, D. Sub-2 nm Ultrasmall High-Entropy Alloy Nanoparticles for Extremely Superior Electrocatalytic Hydrogen Evolution. *J. Am. Chem. Soc.* **2021**, *143* (41), 17117–17127. DOI: 10.1021/jacs.1c07643. Published Online: Sep. 23, 2021.
- (60) Gao, S.; Hao, S.; Huang, Z.; Yuan, Y.; Han, S.; Lei, L.; Zhang, X.; Shahbazian-Yassar, R.; Lu, J. Synthesis of high-entropy alloy nanoparticles on supports by the fast moving bed pyrolysis. *Nat. Commun.* **2020**, *11* (1), 2016. DOI: 10.1038/s41467-020-15934-1. Published Online: Apr. 24, 2020.
- (61) Li, H.; Han, Y.; Zhao, H.; Qi, W.; Zhang, D.; Yu, Y.; Cai, W.; Li, S.; Lai, J.; Huang, B.; Wang, L. *Fast Site-to-site Electron Transfer of High-entropy Alloy Nanocatalyst Driving Redox Electrocatalysis*, 2020. DOI: 10.21203/rs.3.rs-48124/v1.
- (62) Löffler, T.; Waag, F.; Gökce, B.; Ludwig, A.; Barcikowski, S.; Schuhmann, W. Comparing the Activity of Complex Solid Solution Electrocatalysts Using Inflection Points of Voltammetric Activity Curves as Activity Descriptors. *ACS Catal.* **2021**, *11* (3), 1014–1023. DOI: 10.1021/acscatal.0c03313.
- (63) Qiu, H.-J.; Fang, G.; Wen, Y.; Liu, P.; Xie, G.; Liu, X.; Sun, S. Nanoporous high-entropy alloys for highly stable and efficient catalysts. *J. Mater. Chem. A* **2019**, *7* (11), 6499–6506. DOI: 10.1039/C9TA00505F.
- (64) Löffler, T.; Meyer, H.; Savan, A.; Wilde, P.; Garzón Manjón, A.; Chen, Y.-T.; Ventosa, E.; Scheu, C.; Ludwig, A.; Schuhmann, W. Discovery of a Multinary Noble Metal-Free Oxygen Reduction Catalyst. *Adv. Energy Mater.* **2018**, *8* (34), 1802269. DOI: 10.1002/aenm.201802269.
- (65) Wang, S.; Xu, B.; Huo, W.; Feng, H.; Zhou, X.; Fang, F.; Xie, Z.; Shang, J. K.; Jiang, J. Efficient FeCoNiCuPd thin-film electrocatalyst for alkaline oxygen and hydrogen evolution reactions. *Applied Catalysis B: Environmental* **2022**, *313*, 121472. DOI: 10.1016/j.apcatb.2022.121472.

- (66) Wang, T.; Chen, H.; Yang, Z.; Liang, J.; Dai, S. High-Entropy Perovskite Fluorides: A New Platform for Oxygen Evolution Catalysis. *J. Am. Chem. Soc.* **2020**, *142* (10), 4550–4554. DOI: 10.1021/jacs.9b12377. Published Online: Feb. 3, 2020.
- (67) Zhao, X.; Xue, Z.; Chen, W.; Wang, Y.; Mu, T. Eutectic Synthesis of High-Entropy Metal Phosphides for Electrocatalytic Water Splitting. *ChemSusChem* **2020**, *13* (8), 2038–2042. DOI: 10.1002/cssc.202000173. Published Online: Mar. 3, 2020.
- (68) Dai, W.; Lu, T.; Pan, Y. Novel and promising electrocatalyst for oxygen evolution reaction based on MnFeCoNi high entropy alloy. *J. Power Sources* **2019**, *430*, 104–111. DOI: 10.1016/j.jpowsour.2019.05.030.
- (69) Waag, F.; Li, Y.; Ziefuß, A. R.; Bertin, E.; Kamp, M.; Duppel, V.; Marzun, G.; Kienle, L.; Barcikowski, S.; Gökce, B. Kinetically-controlled laser-synthesis of colloidal high-entropy alloy nanoparticles. *RSC Adv.* **2019**, *9* (32), 18547–18558. DOI: 10.1039/c9ra03254a. Published Online: Dec. 6, 2019.
- (70) Zhai, S.; Rojas, J.; Ahlborg, N.; Lim, K.; Toney, M. F.; Jin, H.; Chueh, W. C.; Majumdar, A. The use of poly-cation oxides to lower the temperature of two-step thermochemical water splitting. *Energy Environ. Sci.* **2018**, *11* (8), 2172–2178. DOI: 10.1039/C8EE00050F.
- (71) Nellaiappan, S.; Katiyar, N. K.; Kumar, R.; Parui, A.; Malviya, K. D.; Pradeep, K. G.; Singh, A. K.; Sharma, S.; Tiwary, C. S.; Biswas, K. High-Entropy Alloys as Catalysts for the CO₂ and CO Reduction Reactions: Experimental Realization. *ACS Catal.* **2020**, *10* (6), 3658–3663. DOI: 10.1021/acscatal.9b04302.
- (72) Yusenko, K. V.; Riva, S.; Carvalho, P. A.; Yusenko, M. V.; Arnaboldi, S.; Sukhikh, A. S.; Hanfland, M.; Gromilov, S. A. First hexagonal close packed high-entropy alloy with outstanding stability under extreme conditions and electrocatalytic activity for methanol oxidation. *Scr. Mater.* **2017**, *138*, 22–27. DOI: 10.1016/j.scriptamat.2017.05.022.
- (73) Yao, Y.; Huang, Z.; Xie, P.; Lacey, S. D.; Jacob, R. J.; Xie, H.; Chen, F.; Nie, A.; Pu, T.; Rehwoldt, M.; Yu, D.; Zachariah, M. R.; Wang, C.; Shahbazian-Yassar, R.; Li, J.; Hu, L. Carbothermal shock synthesis of high-entropy-alloy nanoparticles. *Science* **2018**, *359* (6383), 1489–1494. DOI: 10.1126/science.aan5412.
- (74) Glasscott, M. W.; Pendergast, A. D.; Goines, S.; Bishop, A. R.; Hoang, A. T.; Renault, C.; Dick, J. E. Electrosynthesis of high-entropy metallic glass nanoparticles for designer, multi-functional electrocatalysis. *Nat. Commun.* **2019**, *10* (1), 2650. DOI: 10.1038/s41467-019-10303-z. Published Online: Jun. 14, 2019.
- (75) Li, S.; Tang, X.; Jia, H.; Li, H.; Xie, G.; Liu, X.; Lin, X.; Qiu, H.-J. Nanoporous high-entropy alloys with low Pt loadings for high-performance electrochemical oxygen reduction. *J. Catal.* **2020**, *383*, 164–171. DOI: 10.1016/j.jcat.2020.01.024.
- (76) Cantor, B. Multicomponent high-entropy Cantor alloys. *Prog. Mater. Sci.* **2021**, *120*, 100754. DOI: 10.1016/j.pmatsci.2020.100754.
- (77) Banko, L.; Krysiak, O. A.; Pedersen, J. K.; Xiao, B.; Savan, A.; Löffler, T.; Baha, S.; Rossmeisl, J.; Schuhmann, W.; Ludwig, A. Unravelling composition–activity–stability trends in high entropy alloy electrocatalysts by using a data-guided combinatorial synthesis strategy and computational modeling. *Adv. Energy Mater.* **2022**, 2103312. DOI: 10.1002/aenm.202103312.
- (78) Ludwig, A. Discovery of new materials using combinatorial synthesis and high-throughput characterization of thin-film materials libraries combined with computational methods. *npj Comput. Mater.* **2019**, *5* (1). DOI: 10.1038/s41524-019-0205-0.
- (79) Koinuma, H.; Takeuchi, I. Combinatorial solid-state chemistry of inorganic materials. *Nat. Mater.* **2004**, *3* (7), 429–438. DOI: 10.1038/nmat1157.
- (80) Li, Z.; Ludwig, A.; Savan, A.; Springer, H.; Raabe, D. Combinatorial metallurgical synthesis and processing of high-entropy alloys. *J. Mater. Res.* **2018**, *33* (19), 3156–3169. DOI: 10.1557/jmr.2018.214.

- (81) Lee, C.; Wei, X.; Kysar, J. W.; Hone, J. Measurement of the elastic properties and intrinsic strength of monolayer graphene. *Science* **2008**, *321* (5887), 385–388. DOI: 10.1126/science.1157996.
- (82) Bolotin, K. I.; Sikes, K. J.; Jiang, Z.; Klima, M.; Fudenberg, G.; Hone, J.; Kim, P.; Stormer, H. L. Ultrahigh electron mobility in suspended graphene. *Solid State Communications* **2008**, *146* (9-10), 351–355. DOI: 10.1016/j.ssc.2008.02.024.
- (83) Mak, K. F.; Lee, C.; Hone, J.; Shan, J.; Heinz, T. F. Atomically thin MoS₂: a new direct-gap semiconductor. *Phys. Rev. Lett.* **2010**, *105* (13), 136805. DOI: 10.1103/physrevlett.105.136805. Published Online: Sep. 24, 2010.
- (84) Fradkin, E. Critical behavior of disordered degenerate semiconductors. II. Spectrum and transport properties in mean-field theory. *Physical review. B, Condensed matter* **1986**, *33* (5), 3263–3268. DOI: 10.1103/PhysRevB.33.3263.
- (85) *Collected Papers of L.D. Landau*; Elsevier, 1965.
- (86) Rudolf Peierls. Quelques propriétés typiques des corps solides. In , 1935.
- (87) Mermin, N. D. Crystalline Order in Two Dimensions. *Phys. Rev.* **1968**, *176* (1), 250–254. DOI: 10.1103/PhysRev.176.250.
- (88) Novoselov, K. S.; Geim, A. K.; Morozov, S. V.; Jiang, D.; Zhang, Y.; Dubonos, S. V.; Grigorieva, I. V.; Firsov, A. A. Electric field effect in atomically thin carbon films. *Science* **2004**, *306* (5696), 666–669. DOI: 10.1126/science.1102896.
- (89) Novoselov, K. S.; Jiang, D.; Schedin, F.; Booth, T. J.; Khotkevich, V. V.; Morozov, S. V.; Geim, A. K. Two-dimensional atomic crystals. *Proc. Natl. Acad. Sci. U S A* **2005**, *102* (30), 10451–10453. DOI: 10.1073/pnas.0502848102. Published Online: Jul. 18, 2005.
- (90) Meyer, J. C.; Geim, A. K.; Katsnelson, M. I.; Novoselov, K. S.; Booth, T. J.; Roth, S. The structure of suspended graphene sheets. *Nature* **2007**, *446* (7131), 60–63. DOI: 10.1038/nature05545.
- (91) Jerusalem Winter School for Theoretical Physics (1987, *J. Statistical mechanics of membranes and surfaces: Proceedings of the 5th Jerusalem Winter School for Theoretical Physics, Jerusalem, 28 Dec. 87-6 Jan. 88*; Jerusalem Winter School for Theoretical Physics, vol. 5; World Scientific, 1989.
- (92) He, Z.; Que, W. Molybdenum disulfide nanomaterials: Structures, properties, synthesis and recent progress on hydrogen evolution reaction. *Appl. Mater. Today* **2016**, *3*, 23–56. DOI: 10.1016/j.apmt.2016.02.001.
- (93) Li, X.; Zhu, H. Two-dimensional MoS₂: Properties, preparation, and applications. *J. Materiomics* **2015**, *1* (1), 33–44. DOI: 10.1016/j.jmat.2015.03.003.
- (94) Mortimer, C. E.; Beck, J.; Müller, U. *Chemie: Das Basiswissen der Chemie*, 12., korr. und aktualisierte Aufl.; Thieme, 2015.
- (95) Yin, Z.; Li, H.; Li, H.; Jiang, L.; Shi, Y.; Sun, Y.; Lu, G.; Zhang, Q.; Chen, X.; Zhang, H. Single-layer MoS₂ phototransistors. *ACS nano* **2012**, *6* (1), 74–80. DOI: 10.1021/nn2024557. Published Online: Dec. 21, 2011.
- (96) Di Bartolomeo, A.; Genovese, L.; Foller, T.; Giubileo, F.; Luongo, G.; Croin, L.; Liang, S.-J.; Ang, L. K.; Schleberger, M. Electrical transport and persistent photoconductivity in monolayer MoS₂ phototransistors. *Nanotechnology* **2017**, *28* (21), 214002. DOI: 10.1088/1361-6528/aa6d98. Published Online: May. 4, 2017.
- (97) Lee, C.; Yan, H.; Brus, L. E.; Heinz, T. F.; Hone, J.; Ryu, S. Anomalous lattice vibrations of single- and few-layer MoS₂. *ACS nano* **2010**, *4* (5), 2695–2700. DOI: 10.1021/nn1003937.
- (98) Hinnemann, B.; Moses, P. G.; Bonde, J.; Jørgensen, K. P.; Nielsen, J. H.; Horch, S.; Chorkendorff, I.; Nørskov, J. K. Biomimetic hydrogen evolution: MoS₂ nanoparticles as catalyst for hydrogen evolution. *J. Am. Chem. Soc.* **2005**, *127* (15), 5308–5309. DOI: 10.1021/ja0504690.
- (99) Jaramillo, T. F.; Jørgensen, K. P.; Bonde, J.; Nielsen, J. H.; Horch, S.; Chorkendorff, I. Identification of active edge sites for electrochemical H₂ evolution from MoS₂ nanocatalysts. *Science* **2007**, *317* (5834), 100–102. DOI: 10.1126/science.1141483.

- (100) Yu, Y.; Huang, S.-Y.; Li, Y.; Steinmann, S. N.; Yang, W.; Cao, L. Layer-dependent electrocatalysis of MoS₂ for hydrogen evolution. *Nano Lett.* **2014**, *14* (2), 553–558. DOI: 10.1021/nl403620g. Published Online: Jan. 16, 2014.
- (101) Tan, S. M.; Ambrosi, A.; Sofer, Z.; Huber, Š.; Sedmidubský, D.; Pumera, M. Pristine Basal- and Edge-Plane-Oriented Molybdenite MoS₂ Exhibiting Highly Anisotropic Properties. *Chemistry* **2015**, *21* (19), 7170–7178. DOI: 10.1002/chem.201500435. Published Online: Mar. 27, 2015.
- (102) Takahashi, Y.; Kobayashi, Y.; Wang, Z.; Ito, Y.; Ota, M.; Ida, H.; Kumatani, A.; Miyazawa, K.; Fujita, T.; Shiku, H.; Korchev, Y. E.; Miyata, Y.; Fukuma, T.; Chen, M.; Matsue, T. High-Resolution Electrochemical Mapping of the Hydrogen Evolution Reaction on Transition-Metal Dichalcogenide Nanosheets. *Angew. Chem. Int. Ed. Engl.* **2020**, *59* (9), 3601–3608. DOI: 10.1002/anie.201912863. Published Online: Jan. 24, 2020.
- (103) Tao, B.; Unwin, P. R.; Bentley, C. L. Nanoscale Variations in the Electrocatalytic Activity of Layered Transition-Metal Dichalcogenides. *J. Phys. Chem. C* **2020**, *124* (1), 789–798. DOI: 10.1021/acs.jpcc.9b10279.
- (104) Bentley, C. L.; Kang, M.; Maddar, F. M.; Li, F.; Walker, M.; Zhang, J.; Unwin, P. R. Electrochemical maps and movies of the hydrogen evolution reaction on natural crystals of molybdenite (MoS₂): basal vs. edge plane activity. *Chem. Sci.* **2017**, *8* (9), 6583–6593. DOI: 10.1039/c7sc02545a. Published Online: Jul. 26, 2017.
- (105) Kari, J.; Olsen, J. P.; Jensen, K.; Badino, S. F.; Krogh, K. B. R. M.; Borch, K.; Westh, P. Sabatier Principle for Interfacial (Heterogeneous) Enzyme Catalysis. *ACS Catal.* **2018**, *8* (12), 11966–11972. DOI: 10.1021/acscatal.8b03547.
- (106) Exner, K. S. Does a Thermoneutral Electrocatalyst Correspond to the Apex of a Volcano Plot for a Simple Two-Electron Process? *Angew. Chem. Int. Ed. Engl.* **2020**, *59* (26), 10236–10240. DOI: 10.1002/anie.202003688. Published Online: Jul. 5, 2020.
- (107) Roduner, E. Understanding catalysis. *Chem. Soc. Rev.* **2014**, *43* (24), 8226–8239. DOI: 10.1039/C4CS00210E. Published Online: Oct. 14, 2014.
- (108) Kuo, D.-Y.; Paik, H.; Kloppenburg, J.; Faeth, B.; Shen, K. M.; Schlom, D. G.; Hautier, G.; Suntivich, J. Measurements of Oxygen Electroadsorption Energies and Oxygen Evolution Reaction on RuO₂(110): A Discussion of the Sabatier Principle and Its Role in Electrocatalysis. *J. Am. Chem. Soc.* **2018**, *140* (50), 17597–17605. DOI: 10.1021/jacs.8b09657. Published Online: Oct. 12, 2018.
- (109) Zhu, L.; Lin, H.; Li, Y.; Liao, F.; Lifshitz, Y.; Sheng, M.; Lee, S.-T.; Shao, M. A rhodium/silicon co-electrocatalyst design concept to surpass platinum hydrogen evolution activity at high overpotentials. *Nat. Commun.* **2016**, *7*, 12272. DOI: 10.1038/ncomms12272. Published Online: Jul. 22, 2016.
- (110) Hammer, B.; Norskov, J. K. Why gold is the noblest of all the metals. *Nature* **1995**, *376* (6537), 238–240. DOI: 10.1038/376238a0.
- (111) Norsko, J. K. Chemisorption on metal surfaces. *Rep. Prog. Phys.* **1990**, *53* (10), 1253–1295. DOI: 10.1088/0034-4885/53/10/001.
- (112) Hammer, B.; Morikawa, Y.; Norskov, J. K. CO chemisorption at metal surfaces and overlayers. *Phys. Rev. Lett.* **1996**, *76* (12), 2141–2144. DOI: 10.1103/PhysRevLett.76.2141.
- (113) Hammer, B.; Nørskov, J. K. Theoretical surface science and catalysis—calculations and concepts. In *Impact of Surface Science on Catalysis*; Advances in Catalysis; Elsevier, 2000; pp 71–129. DOI: 10.1016/S0360-0564(02)45013-4.
- (114) Pettersson, L. G. M.; Nilsson, A. A Molecular Perspective on the d-Band Model: Synergy Between Experiment and Theory. *Top. Catal.* **2014**, *57* (1-4), 2–13. DOI: 10.1007/s11244-013-0157-4.
- (115) Kibler, L. A.; El-Aziz, A. M.; Hoyer, R.; Kolb, D. M. Tuning reaction rates by lateral strain in a palladium monolayer. *Angew. Chem. Int. Ed. Engl.* **2005**, *44* (14), 2080–2084. DOI: 10.1002/anie.200462127.

- (116) Strasser, P.; Koh, S.; Anniyev, T.; Greeley, J.; More, K.; Yu, C.; Liu, Z.; Kaya, S.; Nordlund, D.; Ogasawara, H.; Toney, M. F.; Nilsson, A. Lattice-strain control of the activity in dealloyed core-shell fuel cell catalysts. *Nature chemistry* **2010**, *2* (6), 454–460. DOI: 10.1038/nchem.623. Published Online: Apr. 25, 2010.
- (117) Yang, X.; Wang, Y.; Tong, X.; Yang, N. Strain Engineering in Electrocatalysts: Fundamentals, Progress, and Perspectives. *Adv. Energy Mater.* **2022**, *12* (5), 2102261. DOI: 10.1002/aenm.202102261.
- (118) Datye, I. M.; Daus, A.; Grady, R. W.; Brenner, K.; Vaziri, S.; Pop, E. Strain-Enhanced Mobility of Monolayer MoS₂. *Nano Lett.* **2022**, *22* (20), 8052–8059. DOI: 10.1021/acs.nanolett.2c01707. Published Online: May. 10, 2022.
- (119) Xia, Z.; Guo, S. Strain engineering of metal-based nanomaterials for energy electrocatalysis. *Chem. Soc. Rev.* **2019**, *48* (12), 3265–3278. DOI: 10.1039/c8cs00846a.
- (120) Li, M.; Zhao, Z.; Xia, Z.; Luo, M.; Zhang, Q.; Qin, Y.; Tao, L.; Yin, K.; Chao, Y.; Gu, L.; Yang, W.; Yu, Y.; Lu, G.; Guo, S. Exclusive Strain Effect Boosts Overall Water Splitting in PdCu/Ir Core/Shell Nanocrystals. *Angew. Chem. Int. Ed. Engl.* **2021**, *60* (15), 8243–8250. DOI: 10.1002/anie.202016199. Published Online: Mar. 3, 2021.
- (121) Zhang, X.; Lu, G. Computational Design of Core/Shell Nanoparticles for Oxygen Reduction Reactions. *J. Phys. Chem. Lett.* **2014**, *5* (2), 292–297. DOI: 10.1021/jz4024699. Published Online: Dec. 30, 2013.
- (122) Xiang, J.; Li, P.; Chong, H.; Feng, L.; Fu, F.; Wang, Z.; Zhang, S.; Zhu, M. Bimetallic Pd-Ni core-shell nanoparticles as effective catalysts for the Suzuki reaction. *Nano Res.* **2014**, *7* (9), 1337–1343. DOI: 10.1007/s12274-014-0498-8.
- (123) Xie, M.; Lyu, Z.; Chen, R.; Shen, M.; Cao, Z.; Xia, Y. Pt-Co@Pt Octahedral Nanocrystals: Enhancing Their Activity and Durability toward Oxygen Reduction with an Intermetallic Core and an Ultrathin Shell. *J. Am. Chem. Soc.* **2021**, *143* (22), 8509–8518. DOI: 10.1021/jacs.1c04160. Published Online: May. 27, 2021.
- (124) Liu, G.; Zhou, W.; Ji, Y.; Chen, B.; Fu, G.; Yun, Q.; Chen, S.; Lin, Y.; Yin, P.-F.; Cui, X.; Liu, J.; Meng, F.; Zhang, Q.; Song, L.; Gu, L.; Zhang, H. Hydrogen-Intercalation-Induced Lattice Expansion of Pd@Pt Core-Shell Nanoparticles for Highly Efficient Electrocatalytic Alcohol Oxidation. *J. Am. Chem. Soc.* **2021**, *143* (29), 11262–11270. DOI: 10.1021/jacs.1c05856. Published Online: Jul. 19, 2021.
- (125) He, T.; Wang, W.; Shi, F.; Yang, X.; Li, X.; Wu, J.; Yin, Y.; Jin, M. Mastering the surface strain of platinum catalysts for efficient electrocatalysis. *Nature* **2021**, *598* (7879), 76–81. DOI: 10.1038/s41586-021-03870-z. Published Online: Oct. 6, 2021.
- (126) Yan, K.; Maark, T. A.; Khorshidi, A.; Sethuraman, V. A.; Peterson, A. A.; Guduru, P. R. The Influence of Elastic Strain on Catalytic Activity in the Hydrogen Evolution Reaction. *Angew. Chem. Int. Ed. Engl.* **2016**, *55* (21), 6175–6181. DOI: 10.1002/anie.201508613.
- (127) Deng, Q.; Smetanin, M.; Weissmüller, J. Mechanical modulation of reaction rates in electrocatalysis. *J. Catal.* **2014**, *309*, 351–361. DOI: 10.1016/j.jcat.2013.10.008.
- (128) Lee, S.-J.; Pyun, S.-I.; Lee, S.-K.; Kang, S.-J. L. Fundamentals of Rotating Disc and Ring-Disc Electrode Techniques and their Applications to Study of the Oxygen Reduction Mechanism at Pt/C Electrode for Fuel Cells. *Isr. J. Chem.* **2008**, *48* (3-4), 215–228. DOI: 10.1560/IJC.48.3-4.215.
- (129) Stein, H. S.; Gregoire, J. M. Progress and prospects for accelerating materials science with automated and autonomous workflows. *Chem. Sci.* **2019**, *10* (42), 9640–9649. DOI: 10.1039/C9SC03766G. Published Online: Sep. 20, 2019.
- (130) Jenewein, K. J.; Akkoc, G. D.; Kormányos, A.; Cherevko, S. Automated high-throughput activity and stability screening of electrocatalysts. *Chem Catal.* **2022**, *2* (10), 2778–2794. DOI: 10.1016/j.checat.2022.09.019.

- (131) Jenewein, K. J.; Thienhaus, S.; Kormányos, A.; Ludwig, A.; Cherevko, S. High-throughput exploration of activity and stability for identifying photoelectrochemical water splitting materials. *Chem. Sci.* **2022**. DOI: 10.1039/D2SC05115J.
- (132) Elgrishi, N.; Rountree, K. J.; McCarthy, B. D.; Rountree, E. S.; Eisenhart, T. T.; Dempsey, J. L. A Practical Beginner's Guide to Cyclic Voltammetry. *J. Chem. Educ.* **2018**, *95* (2), 197–206. DOI: 10.1021/acs.jchemed.7b00361.
- (133) Bard, A. J.; Faulkner, L. R. *Electrochemical methods: Fundamentals and applications / Allen J. Bard, Larry R. Faulkner*, 2nd ed.; John Wiley, 2000.
- (134) Meunier, V.; Huang, J.; Feng, G.; Qiao, R.; Sumpter, B., Eds. *Volume 11: New Developments in Simulation Methods and Software for Engineering Applications; Safety Engineering, Risk Analysis and Reliability Methods; Transportation Systems*; ASMEDC, 2010.
- (135) Wang, H.; Pilon, L. Physical interpretation of cyclic voltammetry for measuring electric double layer capacitances. *Electrochim. Acta* **2012**, *64*, 130–139. DOI: 10.1016/j.electacta.2011.12.118.
- (136) Meunier, V.; Huang, J.; Feng, G.; Qiao, R.; Sumpter, B. G. Modern Theories of Carbon-Based Electrochemical Capacitors: A Short Review. In *Volume 11: New Developments in Simulation Methods and Software for Engineering Applications; Safety Engineering, Risk Analysis and Reliability Methods; Transportation Systems*; Meunier, V., Huang, J., Feng, G., Qiao, R., Sumpter, B., Eds.; ASMEDC, 2010; pp 21–30. DOI: 10.1115/IMECE2010-41003.
- (137) Sliozberg, K.; Schäfer, D.; Erichsen, T.; Meyer, R.; Khare, C.; Ludwig, A.; Schuhmann, W. High-throughput screening of thin-film semiconductor material libraries I: system development and case study for Ti-W-O. *ChemSusChem* **2015**, *8* (7), 1270–1278. DOI: 10.1002/cssc.201402917. Published Online: Feb. 27, 2015.
- (138) Schäfer, D.; Mardare, C.; Savan, A.; Sanchez, M. D.; Mei, B.; Xia, W.; Muhler, M.; Ludwig, A.; Schuhmann, W. High-throughput characterization of Pt supported on thin film oxide material libraries applied in the oxygen reduction reaction. *Anal. Chem.* **2011**, *83* (6), 1916–1923. DOI: 10.1021/ac102303u. Published Online: Feb. 17, 2011.
- (139) Grote, J.-P.; Zeradjanin, A. R.; Cherevko, S.; Savan, A.; Breitbach, B.; Ludwig, A.; Mayrhofer, K. J. Screening of material libraries for electrochemical CO₂ reduction catalysts – Improving selectivity of Cu by mixing with Co. *J. Catal.* **2016**, *343*, 248–256. DOI: 10.1016/j.jcat.2016.02.026.
- (140) Grote, J.-P.; Zeradjanin, A. R.; Cherevko, S.; Mayrhofer, K. J. J. Coupling of a scanning flow cell with online electrochemical mass spectrometry for screening of reaction selectivity. *Rev. Sci. Instrum.* **2014**, *85* (10), 104101. DOI: 10.1063/1.4896755.
- (141) Jenewein, K.; Kormanyos, A.; Knöppel, J.; Mayrhofer, K. J. J.; Cherevko, S. Accessing in Situ Photocorrosion Under Realistic Light Conditions. *Meet. Abstr.* **2022**, *MA2022-01* (45), 1886. DOI: 10.1149/MA2022-01451886mtgabs.
- (142) Liu, X.; Shen, Y.; Yang, R.; Zou, S.; Ji, X.; Shi, L.; Zhang, Y.; Liu, D.; Xiao, L.; Zheng, X.; Li, S.; Fan, J.; Stucky, G. D. Inkjet printing assisted synthesis of multicomponent mesoporous metal oxides for ultrafast catalyst exploration. *Nano Lett.* **2012**, *12* (11), 5733–5739. DOI: 10.1021/nl302992q. Published Online: Oct. 18, 2012.
- (143) Jaramillo, T. F.; Baeck, S.-H.; Kleiman-Shwarsstein, A.; Choi, K.-S.; Stucky, G. D.; McFarland, E. W. Automated electrochemical synthesis and photoelectrochemical characterization of Zn_{1-x}Co_xO thin films for solar hydrogen production. *J. Comb. Chem.* **2005**, *7* (2), 264–271. DOI: 10.1021/cc049864x.
- (144) Gerken, J. B.; Shaner, S. E.; Massé, R. C.; Porubsky, N. J.; Stahl, S. S. A survey of diverse earth abundant oxygen evolution electrocatalysts showing enhanced activity from Ni–Fe oxides containing a third metal. *Energy Environ. Sci.* **2014**, *7* (7), 2376–2382. DOI: 10.1039/C4EE00436A.
- (145) Gregoire, J. M.; Xiang, C.; Liu, X.; Marcin, M.; Jin, J. Scanning droplet cell for high throughput electrochemical and photoelectrochemical measurements. *Rev. Sci. Instrum.* **2013**, *84* (2), 24102. DOI: 10.1063/1.4790419.

- (146) Meyer, R.; Sliozberg, K.; Khare, C.; Schuhmann, W.; Ludwig, A. High-throughput screening of thin-film semiconductor material libraries II: characterization of Fe-W-O libraries. *ChemSusChem* **2015**, *8* (7), 1279–1285. DOI: 10.1002/cssc.201402918. Published Online: Feb. 27, 2015.
- (147) Klemm, S. O.; Topalov, A. A.; Laska, C. A.; Mayrhofer, K. J. Coupling of a high throughput microelectrochemical cell with online multielemental trace analysis by ICP-MS. *Electrochem. commun.* **2011**, *13* (12), 1533–1535. DOI: 10.1016/j.elecom.2011.10.017.
- (148) Löffler, T.; Wilde, P.; Öhl, D.; Chen, Y.-T.; Tschulik, K.; Schuhmann, W. Evaluation of the intrinsic catalytic activity of nanoparticles without prior knowledge of the mass loading. *Faraday Discuss.* **2018**, *210* (0), 317–332. DOI: 10.1039/C8FD00029H.
- (149) Tu, H.-C.; Wang, W.-L.; Wan, C.-C.; Wang, Y.-Y. Novel method for the synthesis of hydrophobic Pt-Ru nanoparticles and its application to preparing a Nafion-free anode for the direct methanol fuel cell. *J. Phys. Chem. B* **2006**, *110* (32), 15988–15993. DOI: 10.1021/jp061638I.
- (150) Wahab, O. J.; Kang, M.; Unwin, P. R. Scanning electrochemical cell microscopy: A natural technique for single entity electrochemistry. *Current Opinion in Electrochemistry* **2020**, *22*, 120–128. DOI: 10.1016/j.coelec.2020.04.018.
- (151) Wang, Y.; Skaanvik, S. A.; Xiong, X.; Wang, S.; Dong, M. Scanning probe microscopy for electrocatalysis. *Matter* **2021**, *4* (11), 3483–3514. DOI: 10.1016/j.matt.2021.09.024.
- (152) Xu, X.; Valavanis, D.; Ciocci, P.; Confederat, S.; Marcuccio, F.; Lemineur, J.-F.; Actis, P.; Kanoufi, F.; Unwin, P. *The new era of high throughput nanoelectrochemistry*, 2022. DOI: 10.26434/chemrxiv-2022-qn6dq-v2.
- (153) Ebejer, N.; Schnippering, M.; Colburn, A. W.; Edwards, M. A.; Unwin, P. R. Localized high resolution electrochemistry and multifunctional imaging: scanning electrochemical cell microscopy. *Anal. Chem.* **2010**, *82* (22), 9141–9145. DOI: 10.1021/ac102191u. Published Online: Oct. 15, 2010.
- (154) Bentley, C. L.; Edmondson, J.; Meloni, G. N.; Perry, D.; Shkirskiy, V.; Unwin, P. R. Nanoscale Electrochemical Mapping. *Anal. Chem.* **2019**, *91* (1), 84–108. DOI: 10.1021/acs.analchem.8b05235. Published Online: Dec. 13, 2018.
- (155) Bentley, C. L. Scanning electrochemical cell microscopy for the study of (nano)particle electrochemistry: From the sub-particle to ensemble level. *Electrochemical Science Adv* **2022**, *2* (3). DOI: 10.1002/elsa.202100081.
- (156) Bentley, C. L.; Kang, M.; Unwin, P. R. Scanning electrochemical cell microscopy: New perspectives on electrode processes in action. *Current Opinion in Electrochemistry* **2017**, *6* (1), 23–30. DOI: 10.1016/j.coelec.2017.06.011.
- (157) Ebejer, N.; Güell, A. G.; Lai, S. C. S.; McKelvey, K.; Snowden, M. E.; Unwin, P. R. Scanning electrochemical cell microscopy: a versatile technique for nanoscale electrochemistry and functional imaging. *Annual review of analytical chemistry (Palo Alto, Calif.)* **2013**, *6*, 329–351. DOI: 10.1146/annurev-anchem-062012-092650. Published Online: Apr. 1, 2013.
- (158) Tarnev, T. Scanning electrochemical cell microscopy as a tool for the evaluation of electrocatalytic activity at the nanoscale, Ruhr-Universität Bochum, 2022.
- (159) Tarnev, T.; Cychy, S.; Andronescu, C.; Muhler, M.; Schuhmann, W.; Chen, Y.-T. Eine universelle, auf Nanokapillaren basierende Methode zur Katalysatorimmobilisierung für die Flüssigzell-Transmissionselektronenmikroskopie. *Angew. Chem.* **2020**, *132* (14), 5634–5638. DOI: 10.1002/ange.201916419.
- (160) Bentley, C. L.; Andronescu, C.; Smialkowski, M.; Kang, M.; Tarnev, T.; Marler, B.; Unwin, P. R.; Apfel, U.-P.; Schuhmann, W. Local Surface Structure and Composition Control the Hydrogen Evolution Reaction on Iron Nickel Sulfides. *Angew. Chem. Int. Ed. Engl.* **2018**, *57* (15), 4093–4097. DOI: 10.1002/anie.201712679. Published Online: Mar. 9, 2018.

- (161) Zhang, G.; Güell, A. G.; Kirkman, P. M.; Lazenby, R. A.; Miller, T. S.; Unwin, P. R. Versatile Polymer-Free Graphene Transfer Method and Applications. *ACS Appl. Mater. Interfaces* **2016**, *8* (12), 8008–8016. DOI: 10.1021/acsami.6b00681. Published Online: Mar. 18, 2016.
- (162) Snowden, M. E.; Güell, A. G.; Lai, S. C. S.; McKelvey, K.; Ebejer, N.; O'Connell, M. A.; Colburn, A. W.; Unwin, P. R. Scanning electrochemical cell microscopy: theory and experiment for quantitative high resolution spatially-resolved voltammetry and simultaneous ion-conductance measurements. *Anal. Chem.* **2012**, *84* (5), 2483–2491. DOI: 10.1021/ac203195h. Published Online: Feb. 17, 2012.
- (163) Bentley, C. L.; Gaudin, L. F.; Kang, M. Direct electrochemical identification of rare microscopic catalytic active sites. *Chem. Commun. (Camb)* **2023**, *59* (16), 2287–2290. DOI: 10.1039/d2cc06316f. Published Online: Feb. 21, 2023.
- (164) Shkirskiy, V.; Yule, L. C.; Daviddi, E.; Bentley, C. L.; Aarons, J.; West, G.; Unwin, P. R. Nanoscale Scanning Electrochemical Cell Microscopy and Correlative Surface Structural Analysis to Map Anodic and Cathodic Reactions on Polycrystalline Zn in Acid Media. *J. Electrochem. Soc.* **2020**, *167* (4), 41507. DOI: 10.1149/1945-7111/ab739d.
- (165) Yule, L. C.; Daviddi, E.; West, G.; Bentley, C. L.; Unwin, P. R. Surface microstructural controls on electrochemical hydrogen absorption at polycrystalline palladium. *J. Electroanal. Chem.* **2020**, *872*, 114047. DOI: 10.1016/j.jelechem.2020.114047.
- (166) Wang, Y.; Li, M.; Ren, H. Voltammetric Mapping of Hydrogen Evolution Reaction on Pt Locally via Scanning Electrochemical Cell Microscopy. *ACS Meas. Au* **2022**. DOI: 10.1021/acsmesuresciau.2c00012.
- (167) Chen, C.-H.; Meadows, K. E.; Cuharuc, A.; Lai, S. C. S.; Unwin, P. R. High resolution mapping of oxygen reduction reaction kinetics at polycrystalline platinum electrodes. *Phys. Chem. Chem. Phys.* **2014**, *16* (34), 18545–18552. DOI: 10.1039/c4cp01511h.
- (168) Tetteh, E. B.; Banko, L.; Krysiak, O. A.; Löffler, T.; Xiao, B.; Varhade, S.; Schumacher, S.; Savan, A.; Andronesco, C.; Ludwig, A.; Schuhmann, W. Zooming-in – Visualization of active site heterogeneity in high entropy alloy electrocatalysts using scanning electrochemical cell microscopy. *Electrochem. Sci. Adv.* **2021**, *2*, e2100105. DOI: 10.1002/elsa.202100105.
- (169) Daviddi, E.; Chen, Z.; Beam Massani, B.; Lee, J.; Bentley, C. L.; Unwin, P. R.; Ratcliff, E. L. Nanoscale Visualization and Multiscale Electrochemical Analysis of Conductive Polymer Electrodes. *ACS nano* **2019**, *13* (11), 13271–13284. DOI: 10.1021/acsnano.9b06302. Published Online: Nov. 7, 2019.
- (170) Bentley, C. L.; Agoston, R.; Tao, B.; Walker, M.; Xu, X.; O'Mullane, A. P.; Unwin, P. R. Correlating the Local Electrocatalytic Activity of Amorphous Molybdenum Sulfide Thin Films with Microscopic Composition, Structure, and Porosity. *ACS Appl. Mater. Interfaces* **2020**, *12* (39), 44307–44316. DOI: 10.1021/acsami.0c11759. Published Online: Sep. 15, 2020.
- (171) Martín-Yerga, D.; Milan, D. C.; Xu, X.; Fernández-Vidal, J.; Whalley, L.; Cowan, A. J.; Hardwick, L. J.; Unwin, P. R. Dynamics of Solid-Electrolyte Interphase Formation on Silicon Electrodes Revealed by Combinatorial Electrochemical Screening. *Angew. Chem. Int. Ed. Engl.* **2022**, *61* (34), e202207184. DOI: 10.1002/anie.202207184. Published Online: Jul. 13, 2022.
- (172) Mariano, R. G.; Kang, M.; Wahab, O. J.; McPherson, I. J.; Rabinowitz, J. A.; Unwin, P. R.; Kanan, M. W. Microstructural origin of locally enhanced CO₂ electroreduction activity on gold. *Nat. Mater.* **2021**, *20* (7), 1000–1006. DOI: 10.1038/s41563-021-00958-9. Published Online: Mar. 18, 2021.
- (173) Tarnev, T.; Aiyappa, H. B.; Botz, A.; Erichsen, T.; Ernst, A.; Andronesco, C.; Schuhmann, W. Scanning Electrochemical Cell Microscopy Investigation of Single ZIF-Derived Nanocomposite Particles as Electrocatalysts for Oxygen Evolution in Alkaline Media. *Angew. Chem. Int. Ed. Engl.* **2019**, *58* (40), 14265–14269. DOI: 10.1002/anie.201908021. Published Online: Aug. 21, 2019.
- (174) Quast, T.; Varhade, S.; Saddeler, S.; Chen, Y.-T.; Andronesco, C.; Schulz, S.; Schuhmann, W. Single Particle Nanoelectrochemistry Reveals the Catalytic Oxygen Evolution Reaction Activity of Co₃O₄

Nanocubes. *Angew. Chem. Int. Ed. Engl.* **2021**, *60* (43), 23444–23450. DOI: 10.1002/anie.202109201. Published Online: Sep. 23, 2021.

(175) Daviddi, E.; Gonos, K. L.; Colburn, A. W.; Bentley, C. L.; Unwin, P. R. Scanning Electrochemical Cell Microscopy (SECCM) Chronopotentiometry: Development and Applications in Electroanalysis and Electrocatalysis. *Anal. Chem.* **2019**, *91* (14), 9229–9237. DOI: 10.1021/acs.analchem.9b02091. Published Online: Jun. 28, 2019.

(176) Liu, D.-Q.; Tao, B.; Ruan, H.-C.; Bentley, C. L.; Unwin, P. R. Metal support effects in electrocatalysis at hexagonal boron nitride. *Chem. Commun. (Camb.)* **2019**, *55* (5), 628–631. DOI: 10.1039/c8cc08517j.

(177) Tetteh, E. B.; Löffler, T.; Tarnev, T.; Quast, T.; Wilde, P.; Aiyappa, H. B.; Schumacher, S.; Andronesco, C.; Tilley, R. D.; Chen, X.; Schuhmann, W. Calibrating SECCM measurements by means of a nanoelectrode ruler. The intrinsic oxygen reduction activity of PtNi catalyst nanoparticles. *Nano Res.* **2021**. DOI: 10.1007/s12274-021-3702-7.

(178) Ustarroz, J.; Ornelas, I. M.; Zhang, G.; Perry, D.; Kang, M.; Bentley, C. L.; Walker, M.; Unwin, P. R. Mobility and Poisoning of Mass-Selected Platinum Nanoclusters during the Oxygen Reduction Reaction. *ACS Catal.* **2018**, *8* (8), 6775–6790. DOI: 10.1021/acscatal.8b00553.

(179) Byers, J. C.; Güell, A. G.; Unwin, P. R. Nanoscale electrocatalysis: visualizing oxygen reduction at pristine, kinked, and oxidized sites on individual carbon nanotubes. *J. Am. Chem. Soc.* **2014**, *136* (32), 11252–11255. DOI: 10.1021/ja505708y. Published Online: Aug. 4, 2014.

(180) Mefford, J. T.; Akbashev, A. R.; Kang, M.; Bentley, C. L.; Gent, W. E.; Deng, H. D.; Alsem, D. H.; Yu, Y.-S.; Salmon, N. J.; Shapiro, D. A.; Unwin, P. R.; Chueh, W. C. Correlative operando microscopy of oxygen evolution electrocatalysts. *Nature* **2021**, *593* (7857), 67–73. DOI: 10.1038/s41586-021-03454-x. Published Online: May. 5, 2021.

(181) Mariano, R. G.; McKelvey, K.; White, H. S.; Kanan, M. W. Selective increase in CO₂ electroreduction activity at grain-boundary surface terminations. *Science* **2017**, *358* (6367), 1187–1192. DOI: 10.1126/science.aao3691.

(182) Kim, Y.-R.; Lai, S. C. S.; McKelvey, K.; Zhang, G.; Perry, D.; Miller, T. S.; Unwin, P. R. Nucleation and Aggregative Growth of Palladium Nanoparticles on Carbon Electrodes: Experiment and Kinetic Model. *J. Phys. Chem. C* **2015**, *119* (30), 17389–17397. DOI: 10.1021/acs.jpcc.5b03513.

(183) Lai, S. C. S.; Lazenby, R. A.; Kirkman, P. M.; Unwin, P. R. Nucleation, aggregative growth and detachment of metal nanoparticles during electrodeposition at electrode surfaces. *Chem. Sci.* **2015**, *6* (2), 1126–1138. DOI: 10.1039/c4sc02792b. Published Online: Nov. 7, 2014.

(184) Daviddi, E.; Shkirskiy, V.; Kirkman, P. M.; Robin, M. P.; Bentley, C. L.; Unwin, P. R. Nanoscale electrochemistry in a copper/aqueous/oil three-phase system: surface structure-activity-corrosion potential relationships. *Chem. Sci.* **2020**, *12* (8), 3055–3069. DOI: 10.1039/D0SC06516A. Published Online: Dec. 22, 2020.

(185) Tao, B.; Yule, L. C.; Daviddi, E.; Bentley, C. L.; Unwin, P. R. Correlative Electrochemical Microscopy of Li-Ion (De)intercalation at a Series of Individual LiMn₂O₄ Particles. *Angew. Chem. Int. Ed. Engl.* **2019**, *58* (14), 4606–4611. DOI: 10.1002/anie.201814505. Published Online: Feb. 21, 2019.

(186) Tao, B.; McPherson, I. J.; Daviddi, E.; Bentley, C. L.; Unwin, P. R. Multiscale Electrochemistry of Lithium Manganese Oxide (LiMn₂O₄): From Single Particles to Ensembles and Degrees of Electrolyte Wetting. *ACS Sustain. Chem. Eng.* **2023**, *11* (4), 1459–1471. DOI: 10.1021/acssuschemeng.2c06075. Published Online: Jan. 13, 2023.

(187) Inomata, H.; Takahashi, Y.; Takamatsu, D.; Kumatani, A.; Ida, H.; Shiku, H.; Matsue, T. Visualization of inhomogeneous current distribution on ZrO₂-coated LiCoO₂ thin-film electrodes using scanning electrochemical cell microscopy. *Chem. Commun. (Camb.)* **2019**, *55* (4), 545–548. DOI: 10.1039/c8cc08916g.

- (188) Barton, Z. J.; Rodríguez-López, J. Emerging scanning probe approaches to the measurement of ionic reactivity at energy storage materials. *Analytical and bioanalytical chemistry* **2016**, *408* (11), 2707–2715. DOI: 10.1007/s00216-016-9373-7. Published Online: Feb. 22, 2016.
- (189) Miller, T. S.; Sansuk, S.; E, S. P.; Lai, S. C.; Macpherson, J. V.; Unwin, P. R. Pt nanoparticle modified single walled carbon nanotube network electrodes for electrocatalysis: Control of the specific surface area over three orders of magnitude. *Catalysis Today* **2015**, *244*, 136–145. DOI: 10.1016/j.cattod.2014.06.022.
- (190) E, S. P.; Liu, D.; Lazenby, R. A.; Sloan, J.; Vidotti, M.; Unwin, P. R.; Macpherson, J. V. Electrodeposition of Nickel Hydroxide Nanoparticles on Carbon Nanotube Electrodes: Correlation of Particle Crystallography with Electrocatalytic Properties. *J. Phys. Chem. C* **2016**, *120* (29), 16059–16068. DOI: 10.1021/acs.jpcc.5b12741.
- (191) Takahashi, Y.; Kumatani, A.; MUNAKATA, H.; Inomata, H.; Ito, K.; Ino, K.; Shiku, H.; Unwin, P. R.; Korchev, Y. E.; KANAMURA, K.; Matsue, T. Nanoscale visualization of redox activity at lithium-ion battery cathodes. *Nat. Commun.* **2014**, *5*, 5450. DOI: 10.1038/ncomms6450. Published Online: Nov. 17, 2014.
- (192) Takahashi, Y.; Yamashita, T.; Takamatsu, D.; Kumatani, A.; Fukuma, T. Nanoscale kinetic imaging of lithium ion secondary battery materials using scanning electrochemical cell microscopy. *Chem. Commun. (Camb)* **2020**, *56* (65), 9324–9327. DOI: 10.1039/d0cc02865g. Published Online: Jul. 16, 2020.
- (193) Bentley, C. L.; Kang, M.; Unwin, P. R. Nanoscale Structure Dynamics within Electrocatalytic Materials. *J. Am. Chem. Soc.* **2017**, *139* (46), 16813–16821. DOI: 10.1021/jacs.7b09355. Published Online: Nov. 8, 2017.
- (194) Bentley, C. L.; Unwin, P. R. Nanoscale electrochemical movies and synchronous topographical mapping of electrocatalytic materials. *Faraday Discuss.* **2018**, *210* (0), 365–379. DOI: 10.1039/c8fd00028j.
- (195) Güell, A. G.; Cuharuc, A. S.; Kim, Y.-R.; Zhang, G.; Tan, S.; Ebejer, N.; Unwin, P. R. Redox-dependent spatially resolved electrochemistry at graphene and graphite step edges. *ACS nano* **2015**, *9* (4), 3558–3571. DOI: 10.1021/acsnano.5b00550. Published Online: Mar. 18, 2015.
- (196) Kumatani, A.; Miura, C.; Kuramochi, H.; Ohto, T.; Wakisaka, M.; Nagata, Y.; Ida, H.; Takahashi, Y.; Hu, K.; Jeong, S.; Fujita, J.-I.; Matsue, T.; Ito, Y. Chemical Dopants on Edge of Holey Graphene Accelerate Electrochemical Hydrogen Evolution Reaction. *Advanced science (Weinheim, Baden-Wurtemberg, Germany)* **2019**, *6* (10), 1900119. DOI: 10.1002/advs.201900119. Published Online: Apr. 1, 2019.
- (197) Hill, J. W.; Hill, C. M. Directly Mapping Photoelectrochemical Behavior within Individual Transition Metal Dichalcogenide Nanosheets. *Nano Lett.* **2019**, *19* (8), 5710–5716. DOI: 10.1021/acs.nanolett.9b02336. Published Online: Jul. 12, 2019.
- (198) Krysiak, O. A.; Schumacher, S.; Savan, A.; Schuhmann, W.; Ludwig, A.; Andronescu, C. Searching novel complex solid solution electrocatalysts in unconventional element combinations. *Nano Res.* **2021**. DOI: 10.1007/s12274-021-3637-z.
- (199) Batchelor, T. A.; Pedersen, J. K.; Winther, S. H.; Castelli, I. E.; Jacobsen, K. W.; Rossmeisl, J. High-Entropy Alloys as a Discovery Platform for Electrocatalysis. *Joule* **2019**, *3* (3), 834–845. DOI: 10.1016/j.joule.2018.12.015.
- (200) Löffler, T.; Savan, A.; Meyer, H.; Meischein, M.; Strotkötter, V.; Ludwig, A.; Schuhmann, W. Design of Complex Solid-Solution Electrocatalysts by Correlating Configuration, Adsorption Energy Distribution Patterns, and Activity Curves. *Angew. Chem. Int. Ed. Engl.* **2020**, *59* (14), 5844–5850. DOI: 10.1002/anie.201914666. Published Online: Feb. 11, 2020.
- (201) Sarkar, S.; Peter, S. C. An overview on Pd-based electrocatalysts for the hydrogen evolution reaction. *Inorg. Chem. Front.* **2018**, *5* (9), 2060–2080. DOI: 10.1039/C8QI00042E.

- (202) Schumacher, S.; Baha, S.; Savan, A.; Andronescu, C.; Ludwig, A. High-throughput discovery of hydrogen evolution electrocatalysts in the complex solid solution system Co–Cr–Fe–Mo–Ni. *J. Mater. Chem. A* **2022**. DOI: 10.1039/D2TA01652D.
- (203) Shang, X.-L.; Wang, Z.-J.; Wu, Q.-F.; Wang, J.-C.; Li, J.-J.; Yu, J.-K. Effect of Mo Addition on Corrosion Behavior of High-Entropy Alloys CoCrFeNiMox in Aqueous Environments. *Acta Metall. Sin. (Engl. Lett.)* **2019**, *32* (1), 41–51. DOI: 10.1007/s40195-018-0812-7.
- (204) McKay, F.; Fang, Y.; Kizilkaya, O.; Singh, P.; Johnson, D. D.; Roy, A.; Young, D. P.; Sprunger, P. T.; Flake, J. C.; Shelton, W. A.; Xu, Y. CoCrFeNi High-Entropy Alloy as an Enhanced Hydrogen Evolution Catalyst in an Acidic Solution. *J. Phys. Chem. C* **2021**, *125* (31), 17008–17018. DOI: 10.1021/acs.jpcc.1c03646. Published Online: Aug. 3, 2021.
- (205) Chung, D. Y.; Park, S.; Lopes, P. P.; Stamenkovic, V. R.; Sung, Y.-E.; Markovic, N. M.; Strmcnik, D. Electrokinetic Analysis of Poorly Conductive Electrocatalytic Materials. *ACS Catal.* **2020**, *10* (9), 4990–4996. DOI: 10.1021/acscatal.0c00960.
- (206) Motchenbacher, C. D.; Connelly, J. A.; Motchenbacher, C. D. L. e. d. *Low-noise electronic system design*; J. Wiley & Sons, 1993.
- (207) Regtien, P. P. Uncertainty Aspects. In *Sensors for Mechatronics*; Elsevier, 2012; pp 35–56. DOI: 10.1016/B978-0-12-391497-2.00003-0.
- (208) *ELC-03XS from NPI*. https://www.npielectronic.com/wp-content/uploads/2018/08/ELC-03XS_manual.pdf.
- (209) *FEMTO DLPCA-200*. <https://www.google.com/url?sa=t&rct=j&q=&esrc=s&source=web&cd=&ved=2ahUKEwiJh4KqzZ2AAxWTRvEDHfloAQQQFnoECBYQAQ&url=https%3A%2F%2Fwww.femto.de%2Fimages%2Fpdf-dokumente%2Fde-dlpca-200.pdf&usg=AOvVaw2eYRjxI3Di8zCZLQU6rVGy&opi=89978449>.
- (210) Schumacher, S.; Madauß, L.; Liebsch, Y.; Tetteh, E. B.; Varhade, S.; Schuhmann, W.; Schleberger, M.; Andronescu, C. Revealing the heterogeneity of large-area MoS₂ layers in the electrocatalytic hydrogen evolution reaction. *ChemElectroChem* **2022**. DOI: 10.1002/celec.202200586.
- (211) Madauß, L.; Zegkinoglou, I.; Vázquez Muiños, H.; Choi, Y.-W.; Kunze, S.; Zhao, M.-Q.; Naylor, C. H.; Ernst, P.; Pollmann, E.; Ochedowski, O.; Lebius, H.; Benyagoub, A.; Ban-d'Etat, B.; Johnson, A. T. C.; Djurabekova, F.; Roldan Cuenya, B.; Schleberger, M. Highly active single-layer MoS₂ catalysts synthesized by swift heavy ion irradiation. *Nanoscale* **2018**, *10* (48), 22908–22916. DOI: 10.1039/c8nr04696d.
- (212) Brunet Cabré, M.; Paiva, A. E.; Velický, M.; Colavita, P. E.; McKelvey, K. Electrochemical kinetics as a function of transition metal dichalcogenide thickness. *Electrochim. Acta* **2021**, *393*, 139027. DOI: 10.1016/j.electacta.2021.139027.
- (213) Lai, Y. W.; Hamann, S.; Ehmann, M.; Ludwig, A. High-throughput characterization of stresses in thin film materials libraries using Si cantilever array wafers and digital holographic microscopy. *Rev. Sci. Instrum.* **2011**, *82* (6), 63903. DOI: 10.1063/1.3600594.
- (214) Burger, S. *High Cycle Fatigue of Al and Cu Thin Films by a Novel High-Throughput Method*; KIT Scientific Publishing, 2013.
- (215) Grochla, D.; Banko, L.; Pfetzling-Micklich, J.; Behm, H.; Dahlmann, R.; Ludwig, A. Si micro-cantilever sensor chips for space-resolved stress measurements in physical and plasma-enhanced chemical vapour deposition. *Sensors and Actuators A: Physical* **2018**, *270*, 271–277. DOI: 10.1016/j.sna.2017.12.050.
- (216) Grochla, D.; Siegel, A.; Hamann, S.; Buenconsejo, P. J. S.; Kieschnick, M.; Brunken, H.; König, D.; Ludwig, A. Time- and space-resolved high-throughput characterization of stresses during sputtering and thermal processing of Al–Cr–N thin films. *J. Phys. D: Appl. Phys.* **2013**, *46* (8), 84011. DOI: 10.1088/0022-3727/46/8/084011.
- (217) *P-611.3 NanoCube® XYZ-Nanopositionierer:Spezifikationen*.

- (218) Benn, E. E.; Gaskey, B.; Erlebacher, J. D. Suppression of Hydrogen Evolution by Oxygen Reduction in Nanoporous Electrocatalysts. *J. Am. Chem. Soc.* **2017**, *139* (10), 3663–3668. DOI: 10.1021/jacs.6b10855. Published Online: Feb. 3, 2017.
- (219) Bentley, C. L.; Perry, D.; Unwin, P. R. Stability and Placement of Ag/AgCl Quasi-Reference Counter Electrodes in Confined Electrochemical Cells. *Anal. Chem.* **2018**, *90* (12), 7700–7707. DOI: 10.1021/acs.analchem.8b01588. Published Online: Jun. 8, 2018.
- (220) Pletcher, D.; Sotiropoulos, S. Hydrogen adsorption–desorption and oxide formation–reduction on polycrystalline platinum in unbuffered aqueous solutions. *J. Chem. Soc., Faraday Trans.* **1994**, *90* (24), 3663–3668. DOI: 10.1039/FT9949003663.
- (221) Zhan, D.; Velmurugan, J.; Mirkin, M. V. Adsorption/desorption of hydrogen on Pt nanoelectrodes: evidence of surface diffusion and spillover. *J. Am. Chem. Soc.* **2009**, *131* (41), 14756–14760. DOI: 10.1021/ja902876v.
- (222) Conway, B. E.; Angerstein-Kozłowska, H.; Sharp, W. B. A.; Criddle, E. E. Ultrapurification of water for electrochemical and surface chemical work by catalytic pyrodistillation. *Anal. Chem.* **1973**, *45* (8), 1331–1336. DOI: 10.1021/ac60330a025.
- (223) Igor A. Pasti, Nemanja M. Gavrilov, Slavko V. Mentus. Potentiodynamic Investigation of Oxygen Reduction Reaction on Polycrystalline Platinum Surface in Acidic Solutions: the Effect of the Polarization Rate on the Kinetic Parameters. *Int. J. Electrochem. Sci.* **2012**, *7*, 11076–11090.
- (224) Kaspar, F.; Crameri, F. Coloring Chemistry-How Mindful Color Choices Improve Chemical Communication. *Angew. Chem. Int. Ed. Engl.* **2022**, *61* (16), e202114910. DOI: 10.1002/anie.202114910. Published Online: Mar. 3, 2022.
- (225) Crameri, F.; Shephard, G. E.; Heron, P. J. The misuse of colour in science communication. *Nat. Commun.* **2020**, *11* (1), 5444. DOI: 10.1038/s41467-020-19160-7. Published Online: Oct. 28, 2020.
- (226) Burger, S.; Eberl, C.; Siegel, A.; Ludwig, A.; Kraft, O. A novel high-throughput fatigue testing method for metallic thin films. *Science and technology of advanced materials* **2011**, *12* (5), 54202. DOI: 10.1088/1468-6996/12/5/054202.
- (227) Dieckhöfer, S.; Öhl, D.; Junqueira, J. R. C.; Quast, T.; Turek, T.; Schuhmann, W. Probing the Local Reaction Environment During High Turnover Carbon Dioxide Reduction with Ag-Based Gas Diffusion Electrodes. *Chemistry (Weinheim an der Bergstrasse, Germany)* **2021**, *27* (19), 5906–5912. DOI: 10.1002/chem.202100387. Published Online: Mar. 3, 2021.